UNIVERSITY COLLEGE LONDON

DEPARTMENT OF PHYSICS

AND ASTRONOMY

Quantum Behaviour of Hydrogen and Muonium in Solid-State and Biological Systems

Andrew Kerridge

Thesis submitted for the Degree of Doctor of Philosophy

September 2003

Supervisors: Prof. A. M. Stoneham

Dr. A. H. Harker

ProQuest LLC
789 East Eisenhower Parkway
P.O. Box 1346
Ann Arbor, MI 48106-1346

Abstract

For hydrogen-like nuclei (HLN) such as the proton or muon, the quantum zero point energy cannot be ignored. The main objectives of this thesis were to identify practical ways to model this quantatively, and hence i) to gain an understanding of interactions between the HLN and its environment, and ii) to use this understanding to evaluate the wavefunction of such a nucleus within an electronic structure calculation.

Several features of the HLN-electron interactions were studied analytically by assuming their interaction to be harmonic in nature. It was shown that the accurate modelling of the HLN-electron correlation was extremely important in the evaluation of the HLN wavefunction.

A parametrised correlation model (PCM) was developed, and was shown to accurately reproduce the effective potential energy surface experienced by the HLN when HLN-electron correlation was included.The required parameters showed a simple HLN mass dependence.

The PCM was used to study DNA base molecule adducts formed by addition of a single HLN. The relative stability of these adducts was shown to be dependent on the mass of the HLN, and the inclusion of HLN-electron correlation was shown to lead to a stabilisation of the C-X bonds relative to the N-X and O-X bonds.

The PCM was used to study the interaction of H and Mu with the diamond dopants sulphur and phosphorus. The PCM correctly predicted differences between the HLN wavefunctions in crystalline and molecular environments. The HLN-electron correlation energy was shown to be large enough to cause the phosphorus-muonium defect complex formation energy to become positive.

HLN-impurity-vacancy complexes in diamond were studied using the PCM, and it was found that the lowest energy state was obtained by the HLN saturating a carbon dangling bond, irrespective of the impurity species. It was concluded that the HLN would be effectively localised at a single site.

Contents

List of Figures

List of Tables

Acknowledgements

I would like to thank my supervisors, Professor A. M. Stoneham and Dr. A. H. Harker, for their help and guidance during the course of this work, and also for their critical reading of this thesis.

I am also grateful to my industrial supervisor, Professor S. F. J. Cox, for his help regarding the experimental aspects of muon science, and his patience in explaining these concepts. I would also like to thank the Rutherford Appleton Laboratories for their financial assistance given in support of this work.

I thank Peter Sushko for his help with the computational aspects of this work, and particularly for sharing his expertise in Gaussian 98.

Finally, I would like to thank my parents, other family, and friends for their support and interest in this work.

Chapter 1

Introduction

1.1 The Muon: Production and Properties

The muon, μ^+, has for decades been used in the study of both crystalline solids and organic radicals. It is typically generated via the decay of the pion, π^+, through the parity-violating weak interaction

$$\pi^+ \rightarrow \mu^+ + \nu_\mu, \tag{1.1}$$

where ν_μ is the muon neutrino. Theoretical studies conducted during the 1950's [77] showed that conservation of both linear and angular momentum dictated that the spin of a muon generated via this decay would be polarised antiparallel to its linear momentum, and it was this property which allowed pioneers in the field of μSR (muon spin rotation, relaxation, and resonance) to use the muon as a probe of the local magnetic structure of materials [44, 46]. By firing high energy protons into (typically) carbon or beryllium targets, large numbers of pions can be created, and hence a beam of muons with up to 100% spin polarisation can be generated. This alone, however, is not enough to make the muon a useful probe. Fortunately, it is also radioactive, with a lifetime $\tau_\mu \simeq 2.2\,\mu$s, decaying via the process

$$\mu^+ \longrightarrow e^+ + \nu_e + \overline{\nu}_\mu. \tag{1.2}$$

where ν_e is the electron neutrino, and $\overline{\nu}_\mu$ the muon antineutrino. The decay positrons of Equation 1.2 are emitted preferentially in the direction of the instantaneous spin polarisation of the muon at the time of its decay. It is the detection of these decay positrons which forms the basis of the μSR technique, which will be discussed in more detail later in this chapter.

As a charged particle, the muon will trap electron density (at least in semiconductors and insulators), and so it is more realistic to consider the muon and its trapped electron density as a light ($M_p/M_\mu \simeq 9$) pseudoisotope of hydrogen. The extremely large mass ratio between the muon and the proton presents a unique tool with which to study isotope dependent properties.

Following standard nomenclature, the diamagnetic state (μ^+) will be referred to as Mu^+, whilst the paramagnetic state (μ^+e^-) will be referred to as Mu^0. It should also be noted that another diamagnetic state of muonium can exist, $Mu^- = [\mu^+e^-e^-]$, although experimentally the two are extremely hard to distinguish. For example, in Silicon, where the host nuclei have no nuclear moment, differentiating between Mu^+ and Mu^- is virtually impossible, although for other semiconductors, in particular the 'III-V' compounds such as GaAs, where nuclear quadrupoles are present, the avoided level crossing resonance technique has been applied in order to identify both the Mu^- [19] and Mu^+ centres [25].

1.2 Experimental techniques

The experimental techniques of nuclear magnetic resonance (NMR), electron spin resonance (ESR), and μSR spectroscopies are closely related. For systems within which the muon forms a diamagnetic state, NMR is the most appropriate analogue, with the interaction of the muon spin with the local magnetic field being the measured quantity, whereas when the muon forms a paramagnetic

state, comparisons with ESR are more appropriate, since in this case it is the interaction between the muon and electron spins which is of primary interest.

1.2.1 NMR Spectroscopy

NMR spectroscopy is based upon the principle that the spins of nuclei can be aligned with an external static magnetic field, and then reversed through the application of an alternating field. Although the technique applies to other nuclei, we will consider here only the proton. The energy of a proton with spin projection m_I in a magnetic field of magnitude B is given by

$$E_{m_I} = -g_N \mu_N m_I B, \tag{1.3}$$

where g_N is the proton g-factor, μ_N is the nuclear magneton, and m_I assumes the value of $\pm\frac{1}{2}$. The resonance condition for the transition of a proton from its lower to higher spin state is then given by

$$h\nu = g_N \mu_N B. \tag{1.4}$$

Experimental results are obtained by either varying the magnetic field over a small range and monitoring the absorption of radiation of frequency ν, or by keeping the magnetic field fixed, and monitoring the absorption of radiation over a range of frequencies. In what follows, when we refer to an NMR or ESR spectrum, this is to be interpreted as a plot as a function of B.

In practice, the local magnetic field experienced by the proton differs from the external field due to interactions with the electron density, and so information regarding the electronic structure of a system can be obtained via interpretation of NMR spectra. There is further information contained in a typical NMR spectrum, however, which cannot be identified with electron-proton interactions. This is the *fine structure* of the spectrum, and is due to spin-spin interactions

between the protons in a given system. This component of the spectrum can be used to infer details of the nuclear structure of the system.

1.2.2 ESR Spectroscopy

The energy of an electron in an applied field of magnitude B can be defined in an analogous way to that of a proton. The energy of the electron is given by

$$E_{m_S} = g_e \mu_B B m_S, \tag{1.5}$$

where in this case μ_B is the Bohr magneton, and so the resonance condition is given by

$$h\nu = g_e \mu_B B. \tag{1.6}$$

It should be noted that since the Bohr magneton is approximately 2000 times larger than the nuclear magneton, so the resonance frequency for a given applied field is higher by the same ratio, and so applied fields are typically much smaller in ESR spectroscopy than in its NMR counterpart for the same resonant frequency.

ESR spectroscopy is applied to systems containing unpaired electrons, since the spin transitions associated with the resonance frequency ν are forbidden by the Pauli exclusion principle for closed shell systems. Typical resonance frequencies are in the microwave region, and ESR spectra are obtained by monitoring the absorption of this microwave radiation as the applied magnetic field, B, is varied. Experimentally it is observed that different systems come into resonance at different frequencies, and this is again due to the local magnetic field experienced by the unpaired electron differing from the externally applied field, interpretable through an understanding of the electronic structure of the system. Further structure is observed in the ESR spectra, the *hyperfine structure* asso-

ciated with spin-spin interactions between the unpaired electron and the nuclei in the system. Again only the proton will be considered here. Typically, half of the protons in a given system will have the z-component of their spin given by $m_I = \frac{1}{2}$, and half by $m_I = -\frac{1}{2}$. This leads to an alteration of the electron energy, which can now be defined as

$$H = g_e \mu_B B m_S + h A_0 m_S m_I \tag{1.7}$$

Since m_S can take the values $\pm\frac{1}{2}$,so there will be splitting of the electron energy. This implies that half of the system will resonate when the applied field satisfies

$$\begin{aligned} B &= \frac{h\nu}{g_e \mu_B} \pm \frac{h A_0}{2 g_e \mu_B} \\ &= \frac{h\nu}{g_e \mu_B} \pm \frac{A}{2} \end{aligned} \tag{1.8}$$

and so the ESR spectrum shows two lines separated by a magnetic field of magnitude A. Again more than one hyperfine splitting can be observed in a spectrum if inequivalent protons are present in a system, since the local electronic structure can vary. The ESR spectrum can therefore be used to understand the electronic structure of a given system, in particular allowing a coarse mapping of the molecular orbital occupied by the unpaired electron.

1.2.3 μSR Spectroscopy

As previously stated, μSR stands for muon spin rotation, relaxation, and resonance. These refer to the various experimental techniques which can be used to detect features of the muon decay, and thereby infer information about a system of interest. Reviews of these techniques can be found, for example [119].

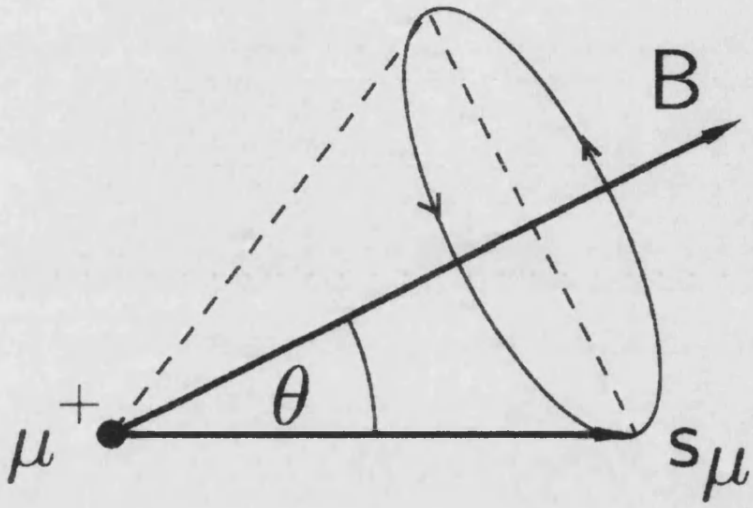

Figure 1.1: Precession of muon spin s_μ about a magnetic field **B**

Tranverse field Muon Spin Rotation (TF-μSR)

In TF-μSR, a magnetic field is applied *perpendicular* to the initial spin polarisation of the muon beam, causing the muon spin to precess about this field with a frequency, ω_μ, proportional to the magnitude of the local field **B** it experiences. This frequency is known as the Larmor frequency (see Figure 1.1), given by

$$\omega_\mu = \gamma_\mu \mathbf{B}, \tag{1.9}$$

where $\gamma_\mu = g_\mu e/2m_\mu$. Typical TF-$\mu$SR spectra are shown in Figure 1.2. These are in fact the Fourier transforms of the measured spectra, and reveal the precession frequencies of the muons implanted in the sample. Hyperfine coupling constants can be obtained directly from these spectra.

Longitudinal field Muon Spin Relaxation (LF-μSR)

In LF-μSR, a magnetic field is applied *parallel* to the initial spin polarisation of the muon beam. In this case, the time-evolution of the muon spin polarisation

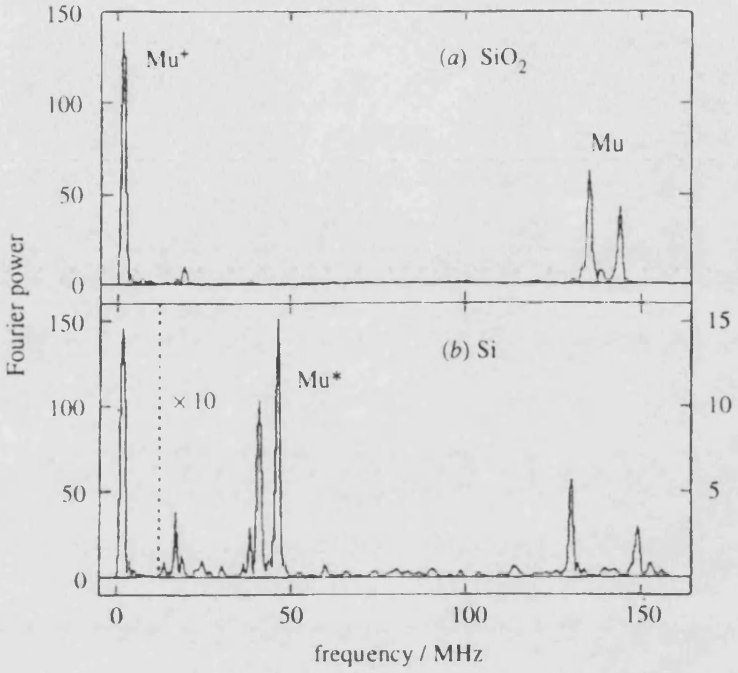

Figure 1.2: Fourier transform of transverse field μSR spectra of SiO_2 and Si (reproduced from [13])

along its original direction is monitored. As the applied field is increased, so the polarisation of the incident beam can be recaptured, giving information about the hyperfine structure of the system. Muon spin relaxation measurements can also be performed in the absence of an applied field, and this is known as Zero Field Muon Spin Relaxation (ZF-μSR). ZF-μSR is a very sensitive technique which allows the detection of weak internal magnetic fields in a system. ZF-μSR has the advantage over other magnetic resonance techniques in that no external field is required, and so can be considered as a technique unique to μSR. Figures 1.3 and 1.4 show simulated and experimentally obtained LF-μSR spectra.

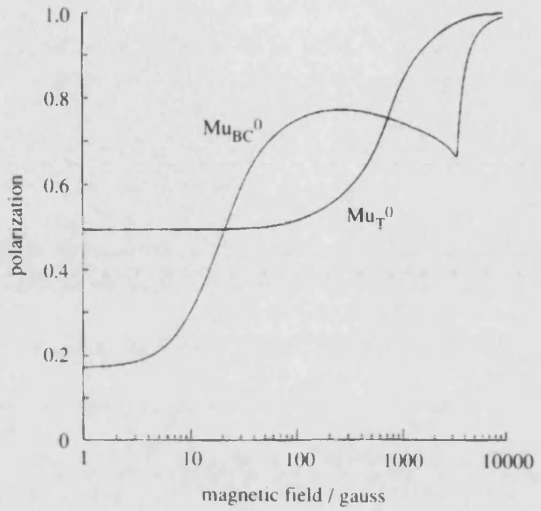

Figure 1.3: Simulated longitudinal field μSR spectra for normal (Mu_T) and anomalous (Mu_{BC}) muonium in silicon (reproduced from [27]).

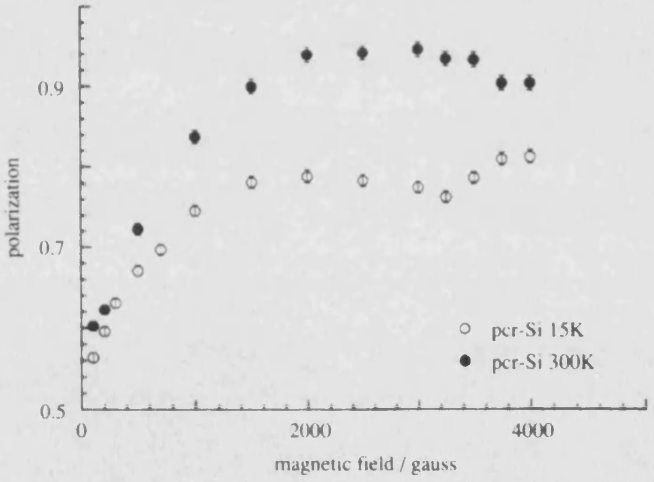

Figure 1.4: Experimental longitudinal field μSR spectra for normal and anomalous muonium in polycrystalline silicon (reproduced from [27]). At $T = 15$K, the reduction in repolarization at $B \sim 3400$G predicted in Figure 1.3 can be clearly seen. Note that Figure 1.3 is plotted on logarithmic scale, whilst Figure 1.4 is plotted on a linear scale.

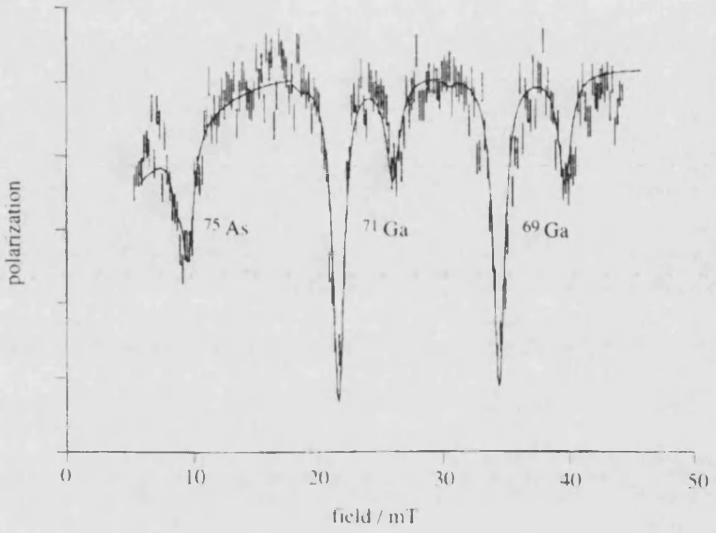

Figure 1.5: Avoided level crossing μSR spectrum of muonium in heavily doped n-type GaAs, characterising the quadrupole interactions of Ga and As nuclei neighbouring the muon (reproduced from [20]).

Avoided Level Crossing Resonance (ALC-μSR)

Muon spin resonance techniques bear more in common with traditional magnetic resonance techniques such as ESR and NMR. A magnetic field is applied parallel to the initial muon spin polarisation, and a radio-frequency field as applied to perturb the muon spin. In ALC-μSR, this RF-field is tuned so that the muon Zeeman splitting is in resonance with the combined Zeeman and quadrupolar splitting of a neighbouring spins system. At resonance, the energy of the combined spin system is unchanged by a spin 'flip-flop' between the muon and a neighbouring spin, and the muon spin polarisation is reduced via this mechanism. Figure 1.5 shows an example of an ALC-μSR spectrum.

General Points

When there is significant electron spin density in the vicinity of the muon, information about the local environment is obtained principally through the isotropic hyperfine interaction

$$A = -\frac{2}{3}\mu_0 g_e \gamma_e \gamma_\mu \left|\varphi_e(0)\right|^2 \mathbf{S}_\mu.\mathbf{S}_e. \tag{1.10}$$

The magnitude of this interaction can be seen to be proportional to the electron spin density at the muon, and so is often referred to as the contact interaction. The vacuum-state value for this interaction is $A_0 = 4.46\,\mathrm{GHz}$.

The measured quantity in any μSR experiment is the distribution of the emitted decay positrons, which is used to infer information about the local magnetic environment. The muon decay is a three body process (see Equation 1.2), and so the energies of the decay positrons may vary. The angular distribution can be modelled as a function of angle and positron energy,

$$P(E,\theta) = 1 + a(E)\cos(\theta), \tag{1.11}$$

where $a(E)$ is the asymmetry parameter, and is a measure of the degree to which the linear momentum of the decay positron is correlated to the instantaneous spin polarisation of the muon at the time of its decay. Figure 1.6 shows $P(E,\theta)$ for the most energetic decay positrons, for which $a(E) = 1$. The energy averaged angular distribution function, for which $a(E) = \frac{1}{3}$, shows a much less pronounced angular dependence. This asymmetry in the energy of the decay positrons is essential to the understanding of μSR spectra. Further information on experimental techniques can be found in [24, 112].

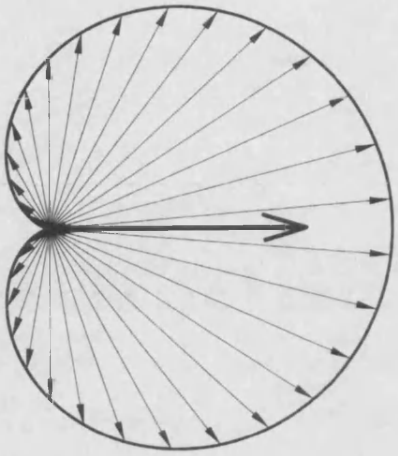

Figure 1.6: $P(E,\theta)$ for the highest energy energy decay positrons, for which $a(E)$=1

1.3 Previous Work

Although the theoretical frameworks for the self-consistent evaluation of electronic structure were developed much earlier, the very weak computing power available before the 1970's meant that these techniques could only be applied to very simple systems, and often with extreme approximations, although these methods could often be trusted for qualitatively accurate results. It was from the 1970's onwards that significant computational power became more widely available, and this marked a rapid increase in the amount of research into this area. This section gives an overview of the theoretical work which has been carried out into the behaviour of muonium and hydrogen (in addition to heavier isotopes) in molecular and solid state systems, for which the specific theoretical techniques mentioned are considered in detail in Section 2.1. It is not intended to be an exhaustive review, but gives an account of previously completed work with direct or indirect relevance to this thesis. Since much of the work carried

out experimentally (particularly in μSR) has been on open-shell systems, so this has dictated that much of the theroretical work has been carried out on such systems. Many different theoretical techniques and approximations are used, and the more common ones are discussed in detail in Chapter 2. For further details, see [137] and references therein. The level of approximation used can significantly affect the quality of the results obtained, and the reader should bear this in mind when comparing results discussed here.

1.3.1 Hydrogen and Muonium in Molecular Systems

Saebø, Radom, and Schaefer [116] have performed unrestricted Hartree-Fock (UHF) calculations of the two radicals of formaldehyde, the methoxy and hydroxymethyl radicals, and found the latter to be more stable by 0.217 eV, in agreement with experiment. More recently, Valladares *et al.* have studied the behaviour of implanted muons in organic radicals using a semi-empirical, Hartree-Fock based method known as intermediate neglect of differential overlap (INDO), and observed that in each of the four cases studied , 3-quinolyl nitronyl nitroxide (3-QNNN), para-pyridyl nitronyl nitroxide (p-PYNN), phenyl nitronyl nitroxide (PNN), and para-nitrophenyl nitronyl nitroxide (p-NPNN), the most stable binding site for the muon was a carbon atom joining two N-O groups. The stability of these sites varied between $\sim 0.3 - 1.3$ eV. Jeong *et al.* [69] have performed UHF calculations on muonated radicals of p-NPNN, and assign the experimentally observed μSR signals to the nitrogen and oxygen binding sites of the pair of NO groups. The same authors [68] have performed UHF calculations on muonated radicals of *p*-Cl-Ph-CH=N-TEMPO (an abbreviation of 4-(*p*-chlorobenzylideneamino)-2,2,6,6-tetramethylpiperidin-1-yloxyl). From the theoretical hyperfine coupling constants obtained in these calculations, they con-

clude that the most likely binding sites for the muon are the chlorine and oxygen sites. Brier *et al.* [11] have performed UHF calculations on the bi-Ph-CH=N-TEMPO (*p*-biphenylmethyleneamino-2,2,6,6-tetramethylpiperidin-1-yloxyl) and 4-Pyr-CH=N-TEMPO (4-pyridylmethyleneamino-2,2,6,6-tetramethylpiperidin-1-yloxyl) radicals along with their muonated analogues. They predict that the lowest energy site for hydrogen in the former is the azomethine nitrogen site, whilst the lowest energy site in the latter is the pyridyl nitrogen site. Muonium was found to bond most strongly to oxygen in both systems.

Claxton *et al.* [21] have studied the residual isotope effect (see Section 5.2), which characterises the difference in the hyperfine coupling constants for the muon and proton due to their vibrational motion in a given system. In particular, they studied the hydroxyl and ethyl radicals using a UHF method, and predict an effect of 24% in the former, and 16% in the latter system. Buttar and Webster [15] have performed UHF calculations on isotopomers of the ethyl radical. They predict a residual isotope effect of 15%, and an increase in bond length of C-Mu over C-H of 2.9%. Webster [135] has used a UHF method to consider the vibrational effects of isotopomers of the formyl radical, and calculates a residual isotope effect of 18%, and the same increase in bond length as for the formyl radical of 2.9%. Yu *et al.* [138] have varied the C-H bond length in the cyclohexadienyl radical and its muonated analogue so that theoretically calculated hyperfine coupling constants calculated using INDO agreed with experiment, and found a bond length increase of 4.3% allowed this. Roduner and Reid [111] have studied the same systems using a diatomic Morse potential to predict a bond length increase of 4.9%. Subsequent INDO calculation gave a residual isotope effect of 30.0%. Valladares *et al.* [128] have compared classical and quantum motion of a hydrogen-like nucleus (HLN) in the same systems,

using a discretized imaginary-time path-integral approach to describe the quantum motion of the HLN. Using the electronic structure obtained from INDO calculations, they predict a residual isotope effect of 49.2%, and an increase in bond-length of 3.5%. Using the electronic structure obtained from complete neglect of differential overlap (CNDO) calculations they predict a residual isotope effect of 48.8% and a bond length increase of 3.3%. The experimental value of the residual isotope effect quoted here is 20.6%.

Percival *et al.* [98] have performed both restricted Hartree Fock (RHF) and density functional theory (DFT) calculations, with the latter incorporating the B3LYP exchange-correlation functional, to study the free radical formed by addition of H and Mu to pyrene. Experimental results from the same paper suggest that of the potential radicals which can be formed by addition to pyrene, two are formed readily, whilst a third is formed with in low abundance. Assuming a residual isotope effect of 20%, hyperfine constants were calculated and used to identify the 3 radicals observed experimentally, with accuracies $> 97\%$. Macrae [82] has calculated hyperfine coupling constants and measured relative stabilities of the radicals formed by addition to the molecule TTF at both the UHF and ROHF (Restricted open Hartree-Fock) level. In TTF, the adduct formed by addition to the central carbon atom was found to be the most stable, although only by ~ 0.16 eV, and this stability was observed to be very sensitive to the molecular geometry. A low hyperfine coupling constant observed experimentally was tentatively assigned to this radical. Calculations were also attempted on radicals formed by addition to TCNQ, but little was able to be deduced due to the extreme sensitivity of this system to the basis set and model chemistry used. Macrae and Carmichael [83] have performed DFT calculations using the B3LYP model chemistry to compare and contrast adducts formed by addition

to C=O and C=S bonds in small molecular radicals. They found that although ketone and thioketone H (or Mu) adducts display similar hyperfine structure, in thioamides the interactions are fundamentally different. Oganesyan *et al.* [95] have performed DFT calculations, using the local density approximation (LDA) to evaluate the electron exchange-correlation energy, to study the adducts that can be formed by addition to the four DNA base molecules. Hyperfine coupling constants were calculated for all possible adducts, and good agreement was achieved between these calculations and the small amount of experimental data on these systems. It is also claimed that the theoretically calculated coupling constants are in good agreement with experimental data obtained by the same group, however these results have yet to be published. Cammarere *et al.* [16] have performed UHF calculations on the heme group of cytochrome c in order to identify binding sites for μ^+. They find that the most stable sites for μ^+ are at the nitrogen and carbon of the pyrrole rings, with the former being more stable by 1.87 eV. They conclude that the theoretically calculated Knight shifts[1] should be experimentally observable.

Percival and Wlodek [97] have performed modified neglect of differential overlap (MNDO) on radicals formed by muonium addition to buckminsterfullerene, and conclude that the two experimentally observed μSR precession signals can be attributed to Mu@C_{60}, a free atom state inside the fullerene, and exo-C_{60}Mu, a radical formed by addition on the outside of the molecule, with the latter being the more stable. This conclusion is supported by Estreicher *et al.* [38] who have performed DFT calculations on the same systems. Claxton and Cox [22] have performed both UHF and ROHF calculations on these systems, as well as smaller

[1]The Knight shift is a measure of the change in muon (or proton) resonant frequencies due to interaction with a local magtnetic field. It is usually associated with the NMR spectra of metallic compounds.

clusters of a similar structure. They conclude that exo-C_{60}Mu saturates a C=C bond, and that the distortion of the structure is very localised, and note that the chemical nature of the radical bears many similarities to the ethyl radical. Boxwell *et al.* [9] have performed restricted open shell Hartree-Fock (ROHF) calculations on the C_{60}H and its muonated isotopomer, and predict a residual isotope effect of 6.6%, compared to the experimental value of 9.0%. Donzelli *et al.* [32] argue that UHF calculations show that an *endohedral* adduct (i.e. an adduct in which the muon is bonded to the inside of the fullerene cage) can form, with a hyperfine coupling constant in good agreement with experiment. The energy of this adduct was found to be within 0.1 eV of the energy of Mu@C_{60}, but zero-point effects of the muon were not considered. Subsequent calculations by the same authors [33] confirm the exohedral adduct to be the lowest energy structure by 3.8 eV, and predict a residual isotope effect of 8.0%.

The results discussed in this section show the diverse range of Mu and H containing systems to which theoretical modelling has been applied, and highlights the fact that the quantum nature of the particle under consideration can result in significant deviations from classical theory. This suggests that the incorporation of quantum effects into a theoretical model would provide useful insights into the validity of assuming muonium to be a light analogue of hydrogen.

1.3.2 Hydrogen and Muonium in Diamond and Silicon

Diamond

Goss [51] has recently published a review of the current position regarding the simulation of hydrogen-related defects in diamond, and a summary of calculations on isolated hydrogen and muonium in diamond can be seen in Table 1.1.

Sahoo *et al.* [118] have performed UHF calculations on muonium in small

diamond clusters, and conclude from total energy calculations that 'normal' muonium (i.e. the defect responsible for the isotropic hyperfine interaction observed in μSR spectra of diamond crystals) is localised at the tetrahedral (T), rather than the hexagonal (H), interstitial site. The zero-point energy of the muon is calculated to be 0.48 eV, with the barrier between adjacent T-centres being 0.83 eV, and so the authors conclude that tunnelling events would be very rare. The vibrationally averaged hyperfine coupling constant was calculated to be within 10% of the experimentally accepted value at T, although, as was pointed out by Estreicher *et al.* [35], these results are cluster-size dependent. Mainwood and Stoneham [81] have performed CNDO calculations on hydrogen and muonium in larger diamond clusters. They infer that in both neutral and positively charged systems, the HLN traps electron density, although there may be an energy cost in the formation of this neutral state in the positively charged system. They find a local maximum at the T site, and a minimum at the H site. The zero point energy of a proton at the H-centre is calculated to be 0.17 eV, a value too high for hydrogen to be trapped at this site, since a saddle point lies just 0.125 eV above this minimum. They postulate that deuterium may have one localised level at the H-centre. Estreicher *et al.* [35] have used UHF and partial retention of diatomic differential overlap (PRDDO) methods to study surface effects in diamond clusters of varying sizes. They find that if the C-H bond length for the hydrogen used to terminate the cluster varies between 1.09 Å (the separation that gives the equilibrium geometry), and 1.545 Å (the physical C-C bond length in diamond), then the relative stability of the T-centre with respect to the H-centre falls from 2.1 eV to 0.9 eV. They also report a (rather large) value of 1.17 eV for the zero-point energy of the muon at the T-centre. They conclude surface effects are relatively small if the C-H bond length is set to 1.09

Author	Method	Particle	Site	Barrier (eV)	ZPE (eV)	Stability (eV)
[118]	UHF	μ^+	T*	0.83 (T)	0.48	N/R
[81]	CNDO	p	H*	N/R	0.17	0.125 (SP)
[35]	PRDDO	μ^+	T*	N/R	1.17	0.9 (H)
[36]	PRDDO	classical	BC	2.4 (T)	N/R	2.7 (T)
				2.1 (H)		
[114]	TBMD	classical	ET	N/R	N/R	1.4 (BC)
						1.9 (T)

Table 1.1: Summary of previous calculations on isolated H and Mu in diamond. N/R means that the property was not reported by the authors. An asterisk indicates that the authors did not consider the bond-centred geometry. In columns four and six, T = tetrahedral site, H = hexagonal site, SP = saddle point, BC = bond centre, and ET = Equilateral Triangle site.

Å. The same authors [36] have also studied the relative stability of the T and H-centres with respect to the electronic basis set. In all cases the T-centre was found to be the more stable, and so all energies quoted here are those of the H-centre relative to the T-centre. Using a STO-3G basis set, the stability was calculated to be 2.22 eV, a 3-21G set gave a stability of 1.65 eV, a 4-31G set gave a stability of 1.48 eV, a 3-21G* set gave a stability of 1.35 eV, and a 4-31G* set gave a stability of 1.25 eV. They also find that it *costs* 7.8 eV to implant a muon at the T-centre, and report that full relaxation of the nearest and next-nearest neighbours of the muon results in a lowering of the barrier between T-centres of 0.17 eV, but has little effect on the vibrational wavefunction of the muon. They are unable to reproduce the experimentally observed hyperfine coupling constant for normal muonium.

Estle *et al.* [34] have performed PRDDO calculations on diamond clusters in order to investigate the location of 'anomalous' muonium (i.e. the defect centre which gives rise to the anisotropic hyperfine coupling, with low contact

interaction, and [111] symmetry). They agreed with the proposal by Cox and Symons [23] that the location for anomalous muonium (Mu*) is at the bond centre (BC) location, with an associated large lattice deformation. They report a minimum in the total energy for a muon at the bond centre when the nearest neighbour carbons are relaxed to give a C-C bond length 42% larger than the standard bond length of 1.545 Å. This minimum is 2.7 eV lower than for the muon at the T-centre, and is some 16.6 eV lower than the BC configuration with no lattice distortion. A barrier of 2.4 eV (2.1 eV) is calculated between the BC and T (H) centre. Calculated hyperfine couplings were approximately four times too large. Saada, Adler, and Kalish [114] have performed tight binding molecular dynamics (TBMD) simulations on hydrogen in diamond and predict the BC site to be lower in energy than the T-centre by 0.5 eV, with an increase of the nearest neighbor C-C bond length of 52% but also report a new, lower energy site with six-fold symmetry about the C-C bond, which they term the ET site. Hydrogen at this site causes the C-C bond to dilate by 43%, and is found to be 1.4 eV lower than the BC site, and a simulated annealing procedure ensures that (at this level of theory at least) this site is a *global* minimum of the total energy. The stability of this structure has since been shown by Kanai *et al.* [72] and Goss *et al.* [50] to be an artifact of the method.

Mehandru *et al.* [85] have used the semi-empirical atom-superposition and electron-delocalisation molecular orbital (ASED-MO) technique to study the hydrogen-vacancy complex in diamond. They predict a binding energy of 5.3 eV for hydrogen saturating one of the dangling bonds due to the vacancy, but did not include relaxation around the vacancy. Breuer and Briddon [12] have performed DFT-LDA calculations on the boron-hydrogen (BH) complex in diamond. They find a minimum energy site along the [001] direction, with the BC

site 0.7 eV higher. Mehandru and Anderson [86] have performed (ASED-MO) calculations on the nitrogen-hydrogen (NH) complex, and find the BC-site to be the most stable, with a binding energy of 1.49 eV.

Nishimatsu *et al.* [93] have performed DFT calculations using LDA to approximate the exchange-correlation energy in order to study hydrogen as a lone defect and as part of the sulphur-hydrogen (SH) and phosphorus-hydrogen (PH) complexes in diamond. They find the BC site to be the most stable, with the T site 0.95 eV higher in energy, the antibonding (AB) site 0.99 eV higher, and the H site 1.52 eV higher. For both of the complexes, the most stable site for hydrogen was found to be the AB site around the substitutional impurity. In the PH complex, the hydrogen passivates the donor level, while for the SH complex, the presence of hydrogen results in a shallower singly occupied donor level, as opposed to a deeper double donor level in its absence. They predict a stretch mode (assuming the heavier particle to be fixed) with vibrational frequency $\nu = 2668$ cm^{-1} for the PH complex, and $\nu = 2787$ cm^{-1} for the SH complex.

Silicon

For recent reviews of hydrogen and other point defects in Silicon see Estreicher [39, 40]. A summary of results obtained for isolated hydrogen and muonium in silicon can be seen in Table 1.2.

Mainwood and Stoneham [81] have performed CNDO calculations on silicon clusters, and find the T-centre to be the most stable site, but with the H-centre only 0.052 eV higher in the absence of lattice relaxation, but an outward relaxation of the six nearest neighbours of only 1% results in the centres becoming essentially degenerate. They conclude that no localised neutral state of hydrogen in silicon exists. Estreicher [37] has performed PRDDO and UHF calculations

on hydrogen in silicon clusters, and finds the BC site to be the most stable, when a relaxation of the two nearest neighbours of 34% is included. This site is found to be ~0.9 eV lower than the T site when using basis sets which result in a minimum at this site. The energy of the H site is found to be 0.59 eV above the T site, and the barrier is expected to be low enough for rapid diffusion of hydrogen between T and H to occur, in agreement with Mainwood and Stoneham [81] who did not consider the BC site. Chang and Chadi [18] have performed DFT-LDA calculations on silicon supercells with various hydrogen defects. They find that hydrogen is only most stable at the BC site when a negatively charged Si-H-Si complex is formed, with the T-centre being the most stable for the neutral state, with a predicted binding energy of 1.1 eV. Herring *et al.* [62] have performed DFT-LDA calculations on silicon supercells in order to study the importance of charge states in hydrogen incorporation. They find that, assuming the Fermi level to be at the bottom of the conduction band, H^0 is most stable at the BC site, as is H^+. H^- is most stable at the T-centre. They find no metastable state for H^0, and so conclude that the transition $H^- \rightarrow H^0$ at some non-equilibrium geometry results in a rapid change of site from T to BC, and that there is a 'negative-U' positioning of the donor and acceptor levels. Here U can be defined as

$$U = E_{BC}^{0/+} - E_{T/BC}^{-/0},$$

and can be more clearly interpreted in relation to Figure 1.7. As can be seen, U measures the difference in ionisation energy between the negatively charged and neutral states, and that between the neutral and positively charged states.

Boucher and DeLeo [8] have performed TBMD calculations on hydrogen in silicon supercells. Using parameters derived from the silane environment, they find the T-centre to be most stable, but on adjustment of these parameters find

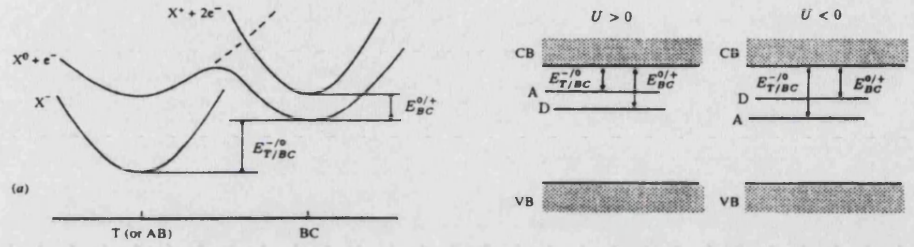

(a) (b)

Figure 1.7: The relative energies and geometries for hydrogen/muonium charge states leading to positive or negative values of U.

a global minimum at the BC site, with a Si-H-Si distance of 3.06 Å, a dilation of 30.2%, with an adiabatic barrier between neighbouring BC sites of 0.23 eV, although they note that the adiabatic picture is not expected to be valid. They also note that the amplitude of the Si-Si stretch mode is not large enough for the BC to become energetically stable, and so postulate an anti-bonding 'precursor' site for H which stretches the associated Si-Si bond, allowing the BC energy minimum to manifest itself.

Tuttle and Van de Walle [126] have performed DFT-LDA calculations in order to study the behaviour the Si-H bond in the vicinity of large vacancies. A system was created to ensure only one Si dangling bond was available. It was found that hydrogen fully passivated this dangling bond, and that the energy of this configuration is 2.6 eV higher than the BC configuration of an otherwise perfect crystal. Assuming the Si to be fixed, the Si-H stretch mode was found to have a vibrational frequency of 1970 cm^{-1}, consistent with that found at the Si surface [73]. The antibonding site is also found to be a local minimum, 1.2 eV higher in energy than the bonding site, and with a stretch mode frequency

Author	Method	Stable Site	Barrier (eV)	ZPE (eV)	Stability (eV)
[81]	CNDO	T*	N/R	N/R	<0.052
[34]	PRDDO	BC	N/R	N/R	0.9 (T)
[18]	LDA	BC (H^-)	N/R	N/R	N/R
		T (H^0)	N/R	N/R	N/R
[60]	LDA	BC (H^0, H^+)	N/R	N/R	N/R
		T (H^-)	N/R	N/R	N/R
[8]	TBMD	BC	0.23 (BC)	N/R	N/R
[107]	PIMC	BC (c)	N/R	N/R	1.22
		T (q)	N/R	0.11 (μ^+)	N/R
[66]	PIMC	T	N/R	0.11 (μ^+)	N/R
[104]	GGA	T	N/R	0.28 (μ^+)	N?R

Table 1.2: Summary of previous calculations on isolated H and Mu in silicon. N/R means that the property was not reported by the authors. An asterisk indicates that the authors did not consider the bond-centred geometry. In column three, c = classical particle, q = quantum particle. In columns three and six, T = tetrahedral site and BC = bond centre.

of 1790 cm^{-1}. The BC site for the Si-Si bond involving the unsaturated silicon is found to be 1.75 eV higher than the bonding site. The barriers to transverse motion appear to be so low as to be unable to localise H at this site.

In a previously cited paper [18], Chang and Chadi find a BC site to be most stable for the BH complex in silicon, with a binding energy of 2.5 eV. They find the AB site of a nearest neighbour Si to be the most stable configuration for the PH complex, in agreement with Johnson *et al.* [70], and predict a binding energy of 2.0 eV. Korpás *et al.* [75] have used the PRDDO method to investigate hydrogen complexes in silicon. They found that both B and P act as strong traps for one interstitial hydrogen, the resulting complexes are likely to be traps for additional hydrogens, and this does not result in the formation of H_2. Luchsinger *et al.* [80] have performed DFT-LDA calculation in order to

study the vibrational modes of hydrogen in the PH complex in silicon. The equilibrium geometry was found to be at the AB site of the Si in a Si-P bond. Assuming that the adiabatic potential energy surface can be decoupled into a bond-axial mode, and a high symmetry transverse mode, vibrational frequencies of 1631 cm^{-1} for the stretch mode and 843 cm^{-1} for the transverse mode are found. If coupling of these vibrational modes is included, a slight lowering of these frequencies is found. Hoffmann *et al.* [63] have performed DFT-LDA in order to study carbon-hydrogen (CH) complex in silicon clusters. They find that the minimum energy of this complex is obtained when the interstitial hydrogen is located at the bond centre between a silicon and substitutional carbon. This configuration is stable by ~0.2 eV when compared to other possible complex configurations, with this stability being reduced to 0.1 eV when zero-point effects are taken into account. Xu [136] has performed tight-binding calculations of various phosphorus-hydrogen complexes in silicon supercells. He finds that none of the complexes studied introduce states into the band gap, and that the role of hydrogen in each of the systems is to passivate the band gap states introduced by the Si dangling bonds. The phosphorus has the effect of lowering the energies of the dangling bonds, and thus of the corresponding defect states.

Ramíres and Herrero [107] have performed Feynman path-integral Monte Carlo (PIMC) calculations on hydrogen and muonium in silicon in order to study the quantum mechanical differences between the two, based on a potential energy surface (PES) calculated by Van de Walle *et al.* [127]. For a point impurity (i.e. a classical proton or muon), they find the BC site to be most stable by 1.22 eV, a stretch mode frequency for this configuration of 2230 cm^{-1}, and a dilation of the nearest neighbour Si-Si bond of 0.3 Å, in general agreement with other work. They find that once the finite mass of the defect is included, two

distinct spatial locations of the muon are present in the temperature range of 50-100 K, as opposed to a single location for the proton and deuteron. The muon in these locations exhibits the properties associated with Mu and Mu*. Mu* is found to be of higher energy than Mu over this range of temperatures, and is not found at temperatures >100 K, in disagreement with experiment. The zero point energies for d, p, and μ^+ at the BC site are found to be 0.100, 0.142, and 0.440 eV respectively. The zero point energy (ZPE) of μ^+ in Mu is found to be 0.11 eV. They conclude that Mu is a highly delocalised state in silicon. Ienaga and Tsuneyuki [66] have performed PIMC calculations on silicon supercells containing a quantum-mechanically described impurity, again using the PES of [127]. They assume a double Born-Oppenheimer approximation, decoupling the electronic motion from that of the impurity and the host lattice, and decoupling the motion of the impurity from that of the lattice. They find two minima in the total energy for an impurity of muon mass, one corresponding to a muon at the T-centre (ZPE = 0.11 eV), and the other corresponding to a muon at the BC site (ZPE = 0.47 eV). However, and again in disagreement with experiment, they predict Mu to be stable at T, rather than BC, and do not consider temperature dependent effects. They find a ZPE of 0.14 eV for the proton at the BC centre, the only energy minimum present when considering an impurity of proton mass. Miyake *et al.* [88] have performed first-principles path-integral molecular dynamics (FP-PIMD) calculations in order to study the quantum distributions of the muon and proton in silicon at 200 K. The interatomic potentials used here are based on DFT calculations using the generalised gradient approximation (GGA) to approximate the electronic exchange-correlation energy. They find that the muon localises in a single cage at the T-centre, and ascribe this localisation to the formation of a small polaron state. The proton (and also a

point impurity) is found to be distributed between two Si atoms in the [001] direction from their common nearest neighbour, the 'C-centre'. They conclude that when quantum effects are taken into account, the lower ZPE of the muon at the T-centre compared to elsewhere is enough to counteract the fact that the T-centre is a local maximum of the PES. Porter *et al.* [104] have performed DFT-LDA and DFT-GGA calculations on silicon supercells in order to study the differences in the quantum distributions of the muon and proton. They apply a double BO approximation in order to decouple electronic, impurity, and lattice degrees of freedom. They find that zero-point effects play only a very small role in lattice relaxation, even at the BC site, accounting for just 0.01 Å of the total relaxation. They find the ZPE of the muon at the BC site to be 0.63 eV, and the corresponding ZPE of the proton to be 0.20 eV. At the T-centre, the muon ZPE was found to be 0.28 eV, and that of the proton to be 0.09 eV. They predict that at the BC site, both the muon and proton could have excited states, but at the T-centre, only the proton has a low enough ZPE to allow an excited state. They again conclude that, when quantum effects are included, the T-centre becomes the more stable site for both the muon and proton.

Herrero [60] has performed PIMC simulations in order to study the thermally assisted tunnelling of hydrogen in silicon. He finds that at temperatures above 40 K, the proton is localised at the C-centre. Below this temperature, a probability density displaying two well-defined maxima appears, with these maxima tending towards the BC site as $T \rightarrow 0$. The probability distribution for the deuteron remains localised at C, even at low temperatures. The Arrhenius plot associated with the proton diffusion shows a distinct change in gradient at temperature of $\sim$80 K, this being the transition temperature calculated here between semi-classical motion over an effective barrier and quantum tunnelling through the

barrier. Noya, Herrero, and Ramírez [94] have performed PIMC calculations in order to study the thermally assisted tunneling of the BH complex in silicon. At a temperature of 100 K, both the hydrogen and boron remain localised, the hydrogen at the C site. At 30 K however, a double maximum is observed in both the hydrogen and boron probability distributions, indicating that the entire complex, rather than just the hydrogen, is tunnelling. The corresponding Arrhenius plot reveals a change in gradient at ~60 K. No deviation is found for the BD complex.

As in the previous section, the results discussed here show that quantitatively different behaviour is predicted in some systems when muonium is compared hydrogen. Here the lighter mass, and hence greater vibrational energy of the muon can be sufficient to cause classically calculated globl energy minima to become higher in energy than surrounding local minima. Again a model which includes this vibrational motion in a self-consistent manner would be a useful tool with which to study such systems.

1.4 Aims of This Thesis

Although many authors have studied the proton and muon in solid state and molecular systems, the vast majority have ignored the quantum effects present due to the their finite mass. Those studies which include these quantum effects require computationally intensive calculations to be performed, restricting the systems that can be studied in both number and size. The aim of this thesis is to investigate the interactions of the hydrogen-like nucleus (HLN) with the electronic and nuclear components of various systems, and to identify the relevant features of these interactions in order to accurately evaluate the HLN wavefunction within the self-consistent field method. This method of evaluation

would greatly reduce the computational effort required to study the effects of including the quantum nature of the HLN on the properties of a given system. Furthermore, this thesis is concerned with the invetsigating the validity of the assumption that muonium can be treated as as a light analogue of hydrogen.

Chapter 2

Theoretical Techniques

Whilst experiment is very useful for understanding the properties of systems of interest, theoretical modelling can be used in a different role. The role of theorist is to identify the important features of a given problem, to build a suitable model incorporating these features, and to use this model to either verify experimental results, or predict new phenomena. For the purposes of this thesis, we require a quantum mechanical description of the hydrogen-like nucleus. Before specifying how this is done, it is worth reviewing the methods available for obtaining a quantum-mechanical description of the electronic structure of the system in terms of its nuclear and electronic degrees of freedom.

2.1 Methods of Electronic Structure Calculation

The ultimate goal of an electronic structure calculation is to solve the many body Schrödinger equation for a system of n interacting particles. In practice however, approximations need to be made in order to attempt this, and typically the variational method is employed. This method allows an approximate solution to the Schrödinger equation to be obtained by minimising the energy of a model system through the optimisation of a set of variational parameters.

In obtaining the minimum electronic energy of a system of interest, there are two main approaches that can be employed; those that attempt to minimise the energy in terms of a wavefunction, $\Psi(\mathbf{r},\mathbf{R})$, and those attempting the same task in terms of a functional of the particle density, $\rho(\mathbf{r},\mathbf{R})$. These two general methods will be examined in more detail in Sections 2.1.1 and 2.1.2, but first it is worth considering two popular approximations employed in order to make the solution to this general problem more tractable. We shall examine these approximations from the perspective of a wavefunction-based approach, although they apply equally to the density functional method.

The Born-Oppenheimer Approximation

$\Psi(\mathbf{r},\mathbf{R})$ can, in principle, be obtained exactly via solution of the Schrödinger equation,

$$\widehat{H}\Psi(\mathbf{r},\mathbf{R}) = E\Psi(\mathbf{r},\mathbf{R}), \tag{2.1}$$

where $\widehat{H}$ is the Hamiltonian operator of the system, and E is the energy of the system. However, Equation 2.1 quickly becomes intractable for all but highly specific Hamiltonians, such as that describing the coupled harmonic oscillators, for which the exact n-body wavefunction can be obtained. To allow highly accurate approximations to $\Psi(\mathbf{r},\mathbf{R})$ to be made using numerical methods, Born and Oppenheimer proposed [7] that a decoupling of the electronic and nuclear degrees of freedom,

$$\Psi(\mathbf{r},\mathbf{R}) = \Phi(\mathbf{R})\psi(\mathbf{r};\mathbf{R}), \tag{2.2}$$

would allow for a solution of the Schrödinger equation which would be functionally dependent on the electronic coordinates of the system, but only parametrically dependent on the nuclear coordinates, a greatly simplified problem. The justification of this approximation lies in the large ratio of the masses of the

nucleons and electrons. This ratio is typically $\sim 10^4$, meaning that the kinetic energy of an electron would be some 100 times greater than that of a typical nucleon, and so, assuming that the electronic system adapts to the new nuclear configuration rapidly, the nuclear motion is effectively frozen during the time period required for this adaptation to take place. The Born-Oppenheimer approximation is actually more severe than this, assuming the nucleons to be of infinite mass (and therefore with no kinetic energy), but has been shown to be highly valid for large nucleon to electron mass ratios. It should be noted that this approximation is not a requirement for the solution of the Schrödinger equation, and indeed methods which do not make this approximation exist, for example the path integral Monte-Carlo method [48].

The Linear Combination of Atomic Orbitals Method

A further simplification is the linear combination of atomic orbitals (LCAO) method. This method assumes that a given electronic wavefunction can be described by a linear combination of basis functions $\{\phi_\mu\}$,

$$\varphi_i(\mathbf{r}_e) = \sum_{i=1}^{n} c_{i\mu}\phi_\mu(\mathbf{r}_e), \tag{2.3}$$

where the $\{\phi_\mu\}$ need not be orthogonal. This approximation allows a set of variational parameters (the $c_{i\mu}$'s) to be defined. The energy of a given system can then be minimised via variation of these parameters. This approximation is conducive to numerical energy minimisation, as it allows the problem to be recast as a matrix mechanics problem, for which many computational techniques have been developed.

2.1.1 Hartree-Fock Theory

Assuming that the Born-Oppenheimer approximation has been made, the problem remains of solving the electronic Schrödinger equation for a given nuclear configuration. The exact solution to this Schrödinger equation is a many body wavefunction, although in general the equation is intractable. An approximate solution can be constructed, however, if it is assumed that an n-electron wavefunction can be well approximated by the product of n 1-electron wavefunctions, i.e.

$$\psi(\mathbf{r}_1, \mathbf{r}_2, ..., \mathbf{r}_n) = \varphi_1(\mathbf{r}_1)\varphi_2(\mathbf{r}_2)...\varphi_n(\mathbf{r}_n). \tag{2.4}$$

This is the Hartree approximation [58]. This approximation alone however, does not ensure that the constructed wavefunction obeys the same quantum mechanical principles as the true n-body wavefunction. The simplest method for constructing a wavefunction which obeys the antisymmetry principle employs what are known as Slater determinants [121]. For a $2n$ electron system, the many-electron wavefunction can be approximated as

$$\psi(\mathbf{r}_1, \mathbf{r}_2, ..., \mathbf{r}_n) = N_\psi \begin{vmatrix} \varphi_1(\mathbf{r}_1)\alpha(1) & \varphi_1(\mathbf{r}_1)\beta(1) & ... & \varphi_n(\mathbf{r}_1)\beta(1) \\ \varphi_1(\mathbf{r}_2)\alpha(2) & \varphi_1(\mathbf{r}_2)\beta(2) & ... & ... \\ ... & ... & ... & ... \\ \varphi_1(\mathbf{r}_{2n})\alpha(2n) & ... & ... & \varphi_n(\mathbf{r}_{2n})\beta(2n) \end{vmatrix} \tag{2.5}$$

where N_ψ is a normalisation factor, and the product $\varphi_n(\mathbf{r}_m)\sigma(m)$ is a spin-orbital, allowing for the distribution of $2n$ electrons across n spatial orbitals (although it should be noted that an even number of electrons is *not* a requirement of this approach). The properties of the determinant of a matrix ensure that the sign of the wavefunction changes under exchange of any two rows, and that the determinant of the matrix, and hence the wavefunction, is zero if any two rows

are identical, as required.

Hartree-Fock theory is an *ab-initio*[1] theory which uses the variational method to minimise the electronic energy of a system described by a single Slater determinant. It first makes the LCAO approximation, with the set of variational coefficients associated with an molecular orbital φ_i described by the set of parameters $\{c_{i\mu}\}$. The set of orbitals $\{\varphi_\mu\}$ define the basis functions of the system. The system of interest is subjected to the constraint

$$\sum_{\mu\nu} c^*_{i\mu} c_{j\nu} S_{\mu\nu} = \delta_{ij}, \tag{2.6}$$

where $S_{\mu\nu} = \langle \phi_\mu | \phi_\nu \rangle$ is an overlap matrix element, and δ_{ij} is the Kronecker delta function. This constraint ensures that the calculated eigenfunctions of the system are orthonormal. The electronic energy expectation can now be evaluated [103], and written in terms of atomic orbitals as

$$\varepsilon = \sum_{\mu\nu} P_{\mu\nu} H_{\mu\nu} + \frac{1}{2} \sum_{\mu\nu\lambda\eta} \left(P_{\mu\nu} P_{\lambda\sigma} - P^\alpha_{\mu\lambda} P^\alpha_{\nu\sigma} - P^\beta_{\mu\lambda} P^\beta_{\nu\sigma} \right) (\mu\nu|\lambda\eta), \tag{2.7}$$

where

$$(\mu\nu|\lambda\eta) = \int\int \phi^*_\mu(\mathbf{r}_1) \phi_\nu(\mathbf{r}_1) \left|\mathbf{r}_1 - \mathbf{r}_2\right|^{-1} \phi^*_\lambda(\mathbf{r}_2) \phi_\eta(\mathbf{r}_2) d^3\mathbf{r}_1 d^3\mathbf{r}_2, \tag{2.8}$$

and $P_{\mu\nu}$, $P^\sigma_{\mu\nu}$ are density matrix and spin density matrix elements respectively, formed from the variational coefficients as

$$P^\sigma_{\mu\nu} = \sum_i^{occ} c^\sigma_{i\mu} c^\sigma_{i\nu} \tag{2.9}$$

and

$$P_{\mu\nu} = P^\alpha_{\mu\nu} + P^\beta_{\mu\nu}. \tag{2.10}$$

[1]The term *ab-initio* is generally used to describe a method which relies on nothing other than the positions and charges of the atomic species, along with the fundamental physical constants, in order to evaluate the ground state electronic structure. It should be noted, however, that density functional theory is also often considered to be an *ab-initio* theory, even though the exchange-correlation energy is evaluated using a parametrised formula.

Determinants which allow a system to be described in this way are known as unrestricted single determinants, and allow separate molecular orbitals to be defined for α-spin and β-spin electrons. This gives rise to the unrestricted Hartree-Fock method, UHF.

The variational method is employed here to minimise the electronic energy through variation of the $c^{\sigma}_{i\mu}$, subject to the constraint of Equation 2.6. This treatment leads to the coupled equations [103]

$$\sum_{\mu} \left(F^{\alpha}_{\mu\nu} - \varepsilon^{\alpha}_{i} S_{\mu\nu}\right) c^{\alpha}_{i\mu} = 0 \tag{2.11a}$$

$$\sum_{\mu} \left(F^{\beta}_{\mu\nu} - \varepsilon^{\beta}_{i} S_{\mu\nu}\right) c^{\beta}_{i\mu} = 0 \tag{2.11b}$$

where $\mathbf{F}^{\sigma}$ is the Fock Hamiltonian matrix for σ-spin electrons, with elements given by

$$F^{\sigma}_{\mu\nu} = H_{\mu\nu} + \sum_{\lambda\eta} \left[P_{\lambda\eta} \left(\mu\nu \mid \lambda\eta\right) - P^{\sigma}_{\lambda\eta} \left(\mu\eta \mid \lambda\nu\right)\right]. \tag{2.12}$$

Here, $H_{\mu\nu}$ are the one-electron core Hamiltonian matrix elements, which can be written in atomic units (where $e = m_e = \hbar = 4\pi\varepsilon_0 = 1$) as

$$H_{\mu\nu} = \left\langle \phi_{\mu}(\mathbf{r}_e) \left| \frac{-\nabla^2}{2} \right| \phi_{\nu}(\mathbf{r}_e) \right\rangle - \sum_{i}^{ions} Q_i \left(\mu \left| |\mathbf{r}_i - \mathbf{r}_e|^{-1} \right| \nu\right) \tag{2.13}$$

where

$$\left(\mu \left| |\mathbf{r}_i - \mathbf{r}_e|^{-1} \right| \nu\right) = \int \phi_{\mu}(\mathbf{r}_e) \left| |\mathbf{r}_i - \mathbf{r}_e|^{-1} \right| \phi_{\nu}(\mathbf{r}_e) d^3\mathbf{r}_e. \tag{2.14}$$

The second term on the RHS of Equation 2.12 measures the Coulomb interaction between the charge distributions $\phi^*_{\nu}\phi_{\mu}$ and $\phi^*_{\lambda}\phi_{\eta}$, whereas the final term defines the exchange interaction, measuring the possible lowering of energy due to the exchange of electrons of identical spins, a purely quantum mechanical effect. Although Hartree-Fock theory treats electron exchange fully, it is mean-field theory, i.e. each of the electrons experiences only the average potential field due

to the other electrons in the system. It ignores the instantaneous electrostatic interactions between electrons, more commonly known as electron correlation. This will be considered further in the following section.

Equation 2.11a can be written in matrix form as

$$\mathbf{F}^{\alpha} \cdot \mathbf{c}^{\alpha} = \boldsymbol{\varepsilon}^{\alpha} \cdot \mathbf{S} \cdot \mathbf{c}^{\alpha}, \tag{2.15}$$

and similarly for Equation 2.11b. These equations are known as the Roothaan equations [55, 113]. These equations collectively form a generalised eigenvalue problem, the solution of which would give as eigenvectors the molecular orbitals of the system, and as eigenvalues the energies of these orbitals. Unfortunately, the solution of Equation 2.15 requires full knowledge of the $c_{i\mu}^{\sigma}$, which in general is unavailable, and so the self-consistent field (SCF) approach is employed. In the SCF approach, an initial density matrix is constructed, often using a very simple semi-empirical method such as extended Hückel theory [65]. This density matrix is used to form an initial Fock matrix, and the energy of the system is calculated. The resulting LCAO coefficients are then used to form a new density matrix, and the process is repeated until the energy of the system converges to within a given tolerance.

Electron Correlation and Perturbation Theory

Hartree-Fock theory, being a mean-field theory, only partially accounts for the electron correlation energy, in that there is an effective repulsion due to the exchange interaction. This leads to electrons of the same spin being found further apart than electrons of differing spin, and this in turn leads to the Hartree-Fock energy being lower than the Hartree energy, which does not contain an exchange term. However, the total electron correlation gives a greater contribution than

the exchange contribution alone[2], and so perturbational methods have been developed to account for this. Möller-Plessett (MP) perturbation theory [89] can be applied to obtain an approximation to this correlation energy. As with perturbation methods in general, different orders of MP perturbation theory can be applied. Therefore an nth order perturbation treatment is referred to as MPn, and higher orders correspond (in principle) to higher accuracy. Perturbation theory, however, rapidly becomes more computationally expensive than HF theory itself. For a system containing N basis functions, HF calculations scale as N^4, MP2 as N^5, and MP4 as N^7. For this reason, it is uncommon to find perturbational treatments higher than MP2 theory being applied to any but very small systems. In MP2, the perturbation to the energy is given by

$$\Delta E_2 = -\sum_{i,j}^{occ.}\sum_{a,b}^{virt.} \frac{((ai|bj) - (aj|bi))^2}{\varepsilon_a + \varepsilon_b - \varepsilon_i - \varepsilon_j}, \tag{2.16}$$

where i, j, a, and b correspond to occupied and virtual orbitals in the *molecular* basis, ε_n is the one-electron eigenvalue corresponding to the nth orbital, and $(ai|bj)$ is a two-electron integral in the molecular basis. MP2 can often account for up to 80% of the total correlation energy.

2.1.2 Density Functional Theory

It can be shown that any physically observable quantity can be calculated (in principle) if the wavefunction of a system can be evaluated exactly. However, the n-body wavefunction is in general a very complicated mathematical object, a function of $3n$ position space variables and n spin variables, whereas most

[2]The correlation energy can be broken down into two terms; 'dynamic' and 'static' correlation. Of interest when studying the interactions between a hydrogen-like nucleus and an electronic system will be the former, which accounts for the fact that charged particles experience a stronger interaction than that given by a mean field approximation as their trajectories take them into close proximity with each other.

operators corresponding to experimental observables are dependent on only one or two particles, or up to 6 position space and 2 spin variables. This implies that much of the information contained in the n-body wavefunction is extraneous. The ground-state electron density can be described in terms of the ground-state wavefunction,

$$\rho(\mathbf{r}) = \sum_{i=1}^{n} \iint \cdots \int \psi^*(\mathbf{r}_1, \mathbf{r}_2, ..., \mathbf{r}_n)\delta(\mathbf{r}_i - \mathbf{r})\psi(\mathbf{r}_1, \mathbf{r}_2, ..., \mathbf{r}_n)d\mathbf{r}_1 d\mathbf{r}_2 \cdots d\mathbf{r}_n, \quad (2.17)$$

and it has been shown [64] that full knowledge of this ground-state density is sufficient to calculate any ground-state observable. Furthermore, a variational principle can be defined in terms of the density

$$E_e[\rho(\mathbf{r})] \geq E_e[\rho_0(\mathbf{r})], \quad (2.18)$$

allowing similar minimisation techniques to those of Hartree-Fock theory to be applied. Density functional theory (DFT) [64, 74] defines a method for calculating this ground state density directly, and (in principle at least) implicitly includes the correlation energy neglected in Hartree-Fock based methods by means of an exchange-correlation functional. To understand how this is achieved it is first worth noting that a single Slater determinant of the form of Equation 2.5 can be looked upon as the exact wavefunction of a system of n $non-interacting$ electrons. For this system, a Hamiltonian can be written as

$$\widehat{H}_{NI} = -\frac{1}{2}\sum_{i=1}^{n} \nabla_i^2 + \sum_{i=1}^{n} V_E(\mathbf{r}_i), \quad (2.19)$$

where V_E is an effective potential in which the electrons move. The kinetic energy of a system described by this Hamiltonian can be evaluated exactly, and a set of eigenfunctions, φ_{NI}^i, can be obtained. These φ_{NI}^i are known as the Kohn-Sham (KS) orbitals.

This non-interacting system is connected to the real one of physical interest by choosing the external potential such that the non-interacting ground-state electron density $\rho_{NI}(\mathbf{r})$ of the system exactly equals that of the real system, i.e.

$$\rho_{NI}(\mathbf{r}) = \sum_{i=1}^{n} \left|\varphi_{NI}^{i}\right|^2 = \rho_0(\mathbf{r}). \tag{2.20}$$

Now, the kinetic energy of the real system cannot be evaluated exactly, since it will be dependent on exchange-correlation effects, and so will be included in the exchange-correlation functional. The total electronic energy of the real system, in the absence of nuclei, can be written

$$E_e[\rho(\mathbf{r})] = T_{NI}[\rho(\mathbf{r})] + J[\rho(\mathbf{r})] + E_{XC}[\rho(\mathbf{r})], \tag{2.21}$$

where $T_{NI}[\rho(\mathbf{r})]$ is the kinetic energy term in the Hamiltonian of Equation 2.19, and $J[\rho(\mathbf{r})]$ measures the potential energy of the electron density,

$$J[\rho(\mathbf{r})] = \frac{1}{2}\iint \frac{\rho(\mathbf{r}_1)\rho(\mathbf{r}_2)}{|\mathbf{r}_1 - \mathbf{r}_2|} d\mathbf{r}_1 d\mathbf{r}_2. \tag{2.22}$$

The exchange-correlation functional $E_{XC}[\rho(\mathbf{r})]$ can then be defined as

$$\begin{aligned} E_{XC}[\rho(\mathbf{r})] &= (T[\rho(\mathbf{r})] - T_{NI}[\rho(\mathbf{r})]) + (E_e[\rho(\mathbf{r})] - J[\rho(\mathbf{r})]) \\ &= T_R[\rho(\mathbf{r})] + E_{NC}[\rho(\mathbf{r})], \end{aligned} \tag{2.23}$$

where $T_R[\rho(\mathbf{r})]$ is the residual part of the true kinetic energy not included in $T_{NI}[\rho(\mathbf{r})]$, and $E_{NC}[\rho(\mathbf{r})]$ is a measure of the non-classical contribution to the potential energy of the system.

$T_{NI}[\rho(\mathbf{r})]$ does not have a simple form in terms of the density $\rho(\mathbf{r})$ since it is defined through the Hamiltonian of Equation 2.19 as

$$T_{NI}[\rho(\mathbf{r})] = -\frac{1}{2}\sum_{i=1}^{n} \left\langle \varphi_{KS}^{i} \left| \nabla^2 \right| \varphi_{KS}^{i} \right\rangle, \tag{2.24}$$

however, the total energy of the real, interacting system (excluding $E_{XC}[\rho(\mathbf{r})]$) can also be written in similar terms, with $E_{Ne}[\rho(\mathbf{r})]$ measuring the potential energy between the electron density and the nuclei in the system;

$$\begin{aligned} E[\rho(\mathbf{r})] &= T_S[\rho(\mathbf{r})] + J[\rho(\mathbf{r})] + E_{Ne}[\rho(\mathbf{r})] + E_{XC}[\rho(\mathbf{r})] \\ &= T_S[\rho(\mathbf{r})] + \frac{1}{2}\iint \frac{\rho(\mathbf{r}_1)\rho(\mathbf{r}_2)}{|\mathbf{r}_1 - \mathbf{r}_2|} d\mathbf{r}_1 d\mathbf{r}_2 + \int V_{Ne}\rho(\mathbf{r}) d\mathbf{r} + E_{XC}[\rho(\mathbf{r})] \\ &= -\frac{1}{2}\sum_{i=1}^{n} \left\langle \varphi_{KS}^i \left| \nabla^2 \right| \varphi_{KS}^i \right\rangle \\ &\quad + \frac{1}{2}\sum_{i,j=1}^{n} \iint \left|\varphi_{KS}^i(\mathbf{r}_1)\right|^2 \frac{1}{\mathbf{r}_{12}} \left|\varphi_{KS}^j(\mathbf{r}_2)\right|^2 d\mathbf{r}_1 d\mathbf{r}_2 \\ &\quad - \sum_{A=1}^{m}\sum_{i=1}^{n} \int \frac{Z_A}{\mathbf{r}_{1A}} \left|\varphi_{KS}^i(\mathbf{r}_1)\right|^2 d\mathbf{r}_1 + E_{XC}[\rho(\mathbf{r})]. \end{aligned} \tag{2.25}$$

The condition which must be fulfilled by the KS orbitals under the constraint $\langle \varphi_{KS}^i | \varphi_{KS}^j \rangle = \delta_{ij}$ can be obtained variationally [96], giving

$$\left(-\frac{1}{2}\nabla^2 + \int \frac{\rho(\mathbf{r}_2)}{\mathbf{r}_{12}} d\mathbf{r}_2 - \sum_{A=1}^{m} \frac{Z_A}{\mathbf{r}_{1A}} + V_{XC}(\mathbf{r}_1) \right) \varphi_{KS}^i(\mathbf{r}_1) = \varepsilon_i \varphi_{KS}^i(\mathbf{r}_1), \tag{2.26}$$

and so the effective potential V_E of Equation 2.19 can be defined as

$$V_E(\mathbf{r}_1) = \int \frac{\rho(\mathbf{r}_2)}{\mathbf{r}_{12}} d\mathbf{r}_2 - \sum_{A=1}^{m} \frac{Z_A}{\mathbf{r}_{1A}} + V_{XC}(\mathbf{r}_1). \tag{2.27}$$

Since we have no knowledge of the form of the exchange-correlation energy E_{XC}, we also have no knowledge of the corresponding potential. Therefore, this potential is simply defined as

$$V_{XC} = \frac{\delta E_{XC}}{\delta \rho}. \tag{2.28}$$

In practice, DFT requires assumptions to be made regarding the particle density in order to approximate this exchange-correlation contribution. The most simple (yet highly successful) approximation is the local density approximation (LDA), or for open-shell systems, the local spin density approximation (LSD). In this

approximation the exchange-correlation functional is assumed to be of the form

$$E_{XC}^{LSD}[\rho_\alpha(\mathbf{r}), \rho_\beta(\mathbf{r})] = \int \rho(\mathbf{r}) \varepsilon_{XC}(\rho_\alpha(\mathbf{r}), \rho_\beta(\mathbf{r})) d\mathbf{r}, \tag{2.29}$$

where $\varepsilon_{XC}(\rho_\alpha(\mathbf{r}), \rho_\beta(\mathbf{r}))$ is the exchange correlation energy per particle of an homogeneous electron gas. $\rho(\mathbf{r})$ weights this energy by the probability that an electron is actually at the point $\mathbf{r}$. Highly accurate Monte-Carlo calculations [17] have been performed in order to ascertain ε_{XC} for various electron densities, and sophisticated interpolation methods have been employed [132, 100] to give approximate analytical expressions for $\varepsilon_{XC}(\rho(\mathbf{r}))$.

Although LSD has proved successful in the determination of equilibrium geometries, harmonic vibrational frequencies, and charge moments, it has well-known deficiencies in the prediction of atomization energies (leading to over-estimation of binding energies) and excitation energies. Attempts to improve on LSD have involved application of the generalised gradient approximation (GGA), which considers not only the contribution to E_{XC} due to the electron density at a given point in space, but also the deviations from this contribution due to the fact that this density is not constant throughout space. The GGA exchange-correlation functional can be written in a rather general way as

$$E_{XC}^{GGA}[\rho_\alpha(\mathbf{r}), \rho_\beta(\mathbf{r})] = \int f\left(\rho_\alpha(\mathbf{r}), \rho_\beta(\mathbf{r}), \nabla\rho_\alpha(\mathbf{r}), \nabla\rho_\beta(\mathbf{r})\right) d\mathbf{r}. \tag{2.30}$$

In practice, E_{XC}^{GGA} is divided into exchange and correlation components, with the correlation term often containing empirical parameters obtained from reference systems. Typically, GGA exchange-correlation functionals use Becke's exchange functional [6], and combine it with the correlation functionals of Perdew [99] or Lee, Yang, and Parr [78].

2.1.3 Approximate SCF methods

Both Hartree-Fock and density functional theory require $\mathcal{O}[N^4]$ two electron integrals (where N is the number of basis functions) to be evaluated per self-consistency cycle, making calculations on large systems very computationally expensive. Because of this, approximate methods have been devised to reduce the computational cost of such calculations. In general, these approaches have been developed as approximations to the Hartree-Fock method, since DFT methods have only become popular with the advent of larger computational power. The earliest approximate SCF-based method was devised by Pople, Santry, and Segal [101], and is known as the complete neglect of differential overlap method, or CNDO. In this semi-empirical method, the overlap matrix of Equation 2.15 is replaced by the identity matrix, reducing the generalised eigenvalue problem to a standard one. Furthermore, two electron integrals are set to zero except in the case where the probability distribution for a given electron can be described in terms of a single basis function. These non-zero integrals are then parametrised to be only dependent on the species of the host nuclei. Off-diagonal core Hamiltonian matrix elements are made proportional to the overlap matrix. These approximations greatly reduce the computational cost of performing SCF calculations, and have been widely used in the decades since their introduction. It should be noted that although CNDO was originally derived from the Roothaan equations, Lindholm and Lundqvist [79] have shown that it can also be derived from the Kohn-Sham equations.

Improvements on CNDO include intermediate neglect of differential overlap (INDO) [102], and neglect of diatomic differential overlap (NNDO) [14], which are both based on similar approximations to CNDO, but retain more of the two-

electron contribution to the Hamiltonian. Another popular approximation is known as the partial retention of differential diatomic overlap, or PRDDO [53], which, although parametrised, is *not* semi-empirical. It is given special mention here as it has been shown to consistently and accurately reproduce energies, wavefunctions, and geometries obtained from minimal basis set HF calculations [53, 54, 84].

These methods, though highly successful, are now becoming less often used. In contrast, more sophisticated methods are being increasingly employed as the necessary computational resources become available.

2.1.4 Other Methods

The Hartree-Fock approximation assumes that the many-body wavefunction can be described by a single Slater determinant of the form of Equation 2.5, but, as discussed previously, this method ignores the effects of electron correlation. A method of including these effects is configuration interaction (CI), which describes the exact many-body wavefunction in terms of a linear combination of Slater determinants, i.e.

$$\psi = \sum_{I=0}^{N_{CI}} C_I \psi_I. \tag{2.31}$$

Here, ψ_0 is the Slater determinant obtained by populating the N lowest energy solution to the Roothaan equations, and all other ψ_n are formed by exciting electrons from these lowest energy states into higher energy, virtual states. In the case $C_0 = 1$ and $C_n = 0$, $n > 0$, we retrieve the Hartree-Fock approximation.

The variational method can be applied [122] and yields the eigenvalue problem

$$\mathbf{H} \cdot \mathbf{C} = \lambda \cdot \mathbf{O} \cdot \mathbf{C}, \tag{2.32}$$

where

$$H_{KJ} = \left\langle \psi_K \left| \widehat{H} \right| \psi_J \right\rangle \tag{2.33a}$$

$$O_{KJ} = \langle \psi_K | \psi_J \rangle \tag{2.33b}$$

$$\lambda = \frac{\left\langle \psi \left| \widehat{H} \right| \psi \right\rangle}{\langle \psi | \psi \rangle}. \tag{2.33c}$$

It should be noted that the solution to Equation 2.32 can be obtained directly (rather than using an iterative approach as in HF theory), since all the matrix elements can be obtained from the solution to the Roothaan equations. In practice, however, the CI method is computational expensive, and so often only singly and doubly excited determinants are used, although other excitations can be included if the physics of the problem clearly neccesitates it.

Path integral Monte-Carlo (PIMC) methods are based on the Feynman path-integral interpretation of quantum mechanics [42]. It can be shown [42] that the partition function required for the evaluation of the expectation value of an observable of a single quantum particle at a finite temperature is formally equivalent to a *classical* partition function of a cyclic chain of P classical particles coupled harmonically, in the limit $P \rightarrow \infty$. This fact allows classical simulation methods, and in particular Monte-Carlo methods, to be applied to finite temperature quantum mechanical problems. In practice, P is typically ≤ 32, and so the partition function obtained is an approximation to the true partition function. However, the PIMC method is in principle capable of an exact solution (including correlation) to the Schrödinger equation at finite temperatures. This method has still not been widely adopted, partly due to the fact that immense computational power is required for PIMC calculations. Miyake *et al.* [88] report calculation times of $0.5-2$ CPU months using the 128 CPU Hitachi SR2201 supercomputer for PIMC calculations on 16 atom silicon supercells containing

one hydrogen or muonium impurity, and with $P \leq 32$.

2.2 Evaluation of the Hydrogen–like Nuclear Wavefunction

For the calculations presented in this thesis, the hydrogen-like nuleus (HLN) is modelled as a heavy, positively charged electron, with the basis set of the system being extended to accommodate this new *distinguishable* particle. The basis set associated with the HLN is defined to be orthogonal to the electron basis set (i.e. the overlap between electron and HLN basis functions is *defined* to be zero). This ensures that the Hamiltonian matrix for the many-body system containing an HLN adopts a block diagonal form. The basis set chosen for the HLN was a local basis, composed of Gaussian functions, and the reasons for this are three-fold. Firstly, the HLN is expected to be highly localised, and so a plane wave basis set would have to be large to reflect this. Secondly, the efficient and (in principle) exact evaluation of the two particle, four-centre integrals required in a full *ab-initio* calculation using a local basis is only possible if the basis set is composed of Gaussians. Thirdly, the potential energy surfaces on which the HLN moves will be expected to be at least approximately harmonic in nature, and so the Gaussian, which is the general form of the solution to the harmonic oscillator Schrödinger equation, is a natural choice.

Since the HLN is a distinguishable particle, there can be no exchange interaction with the electronic components of the system. There can, however, be electron-HLN correlation effects that will be ignored in the Hartree-Fock approximation. These effects will be considered in detail in Chapter 4, but the general

form for the Hamiltonian matrix elements will be given by

$$H_{\lambda\sigma}^{HLN} = \left\langle \phi_\lambda \left| \frac{-\nabla^2}{2m_{HLN}} \right| \phi_\sigma \right\rangle + \sum_i^{ions} Q_i \left(\lambda \left| |\mathbf{r}_i - \mathbf{r}_e|^{-1} \right| \sigma \right) - \sum_{\gamma,\nu}^{elec} P_{\gamma\nu}^{e^-} (\lambda\sigma|\gamma\nu) + V_X \tag{2.34}$$

where γ and ν cycle through the electron basis functions, $P_{\gamma\nu}^{e^-}$ is the associated electron density matrix element, and V_X represents the contribution to the matrix element from electron-HLN correlation.

2.3 Evaluation of Molecular Integrals in a Gaussian Basis

Although well-established commercial programs which implement the methods described in Section 2.1 already exist, the quantum mechanical modelling of the hydrogen-like nucleus in this thesis required additional code to be written and incorporated into these programs. Although in principle existing code from these programs could be used for the evaluation of the required molecular integrals, it was decided that in an attempt to maintain a well-defined separation between a given commercial program and the additional code developed for the requirements of this thesis, new code would be written for the evaluation of the integrals. In this manner, it was hoped that the code could be relatively easily transferred between programs.

Detailed accounts of the methods required for the evaluation of the molecular integrals are few and far between, although they do exist [26]. It will therefore be a useful reference to outline the methods used here. In addition, some of the problems that can occur in the implementation of these methods will be considered, since it would appear that these are not mentioned in the literature.

2.3.1 Preliminaries

There are some basic mathematical concepts and techniques which prove useful in the evaluation of molecular integrals. These are the Gamma function, the Gaussian product theorem, and the Laplace transform.

The Gamma Function

The Gamma function is a generalisation of the factorial function, and is defined as

$$\Gamma(n) = \int_0^\infty u^{n-1} e^{-u} du \tag{2.35}$$

and has the following properties

$$\Gamma(1) = 1 \tag{2.36a}$$

$$\Gamma\left(\frac{1}{2}\right) = \sqrt{\pi} \tag{2.36b}$$

$$\Gamma(n+1) = n\Gamma(n). \tag{2.36c}$$

It will be shown that the Gamma function can be used for the evaluation of both the overlap and kinetic energy integrals, in addition to being of use in the following section.

The Laplace Transform

The Coulomb integrals, by definition, contain terms of the form $|\mathbf{r} - \mathbf{r}_p|^{-1}$, and these terms can be recast, via application of the Laplace transform, into a form which allows the integrals to be evaluated using quadrature methods. The Laplace transform is defined by

$$\mathcal{L}(t) = \int_0^\infty g(\rho) \exp[-t\rho] d\rho. \tag{2.37}$$

Setting $t = |\mathbf{r} - \mathbf{r}_p|^2$ and $g(\rho) = \rho^{-\frac{1}{2}}$ gives

$$\mathcal{L}\left(|\mathbf{r} - \mathbf{r}_p|^2\right) = \int_0^\infty \rho^{-\frac{1}{2}} \exp\left[-|\mathbf{r} - \mathbf{r}_p|^2 \rho\right] d\rho. \tag{2.38}$$

Making the substitution $u = |\mathbf{r} - \mathbf{r}_p|^2 \rho$ allows the integral to be written in the form of a Gamma function;

$$\begin{aligned} \mathcal{L}\left(|\mathbf{r} - \mathbf{r}_p|^2\right) &= |\mathbf{r} - \mathbf{r}_p|^{-1} \int_0^\infty u^{-\frac{1}{2}} \exp\left[-u\right] du \\ &= |\mathbf{r} - \mathbf{r}_p|^{-1} \Gamma\left(\frac{1}{2}\right) \\ &= \sqrt{\pi}\, |\mathbf{r} - \mathbf{r}_p|^{-1}, \end{aligned} \tag{2.39}$$

and so finally

$$|\mathbf{r} - \mathbf{r}_p|^{-1} = \frac{1}{\sqrt{\pi}} \int_0^\infty \rho^{-\frac{1}{2}} \exp\left[-|\mathbf{r} - \mathbf{r}_p|^2 \rho\right] d\rho. \tag{2.40}$$

The Gaussian Product Theorem

The Gaussian product theorem states that the product of two (or more) Gaussians is itself a Gaussian. This can be verified by considering

$$\exp\left[-\alpha(\mathbf{r} - \mathbf{r}_A)^2\right] \times \exp\left[-\beta(\mathbf{r} - \mathbf{r}_B)^2\right] = K \exp\left[-\gamma(\mathbf{r} - \mathbf{r}_P)^2\right] \tag{2.41}$$

where

$$\begin{aligned} \gamma &= \alpha + \beta \\ K &= \exp\left[-\frac{\alpha\beta}{\gamma}(\mathbf{r}_A - \mathbf{r}_B)^2\right] \\ \mathbf{r}_P^2 &= \left(\frac{\alpha\mathbf{r}_A - \beta\mathbf{r}_B}{\gamma}\right)^2. \end{aligned}$$

This result can be generalised to treat Gaussians more familiar to electronic structure calculations, of the form

$$G_A(\mathbf{r}) = N_A(x - x_A)^{l_A}(y - y_A)^{m_A}(z - z_A)^{n_A} \exp\left[-\alpha(\mathbf{r} - \mathbf{r}_A)^2\right]. \tag{2.42}$$

Boys [10] has shown that the $\{l_A,\ m_A,\ n_A\}$ of Equation 2.42 are closely related to the angular momentum quantum numbers. Now,

$$\begin{aligned}(x-x_A)^{l_A} &= ((x-x_P)+(x_P-x_A))^{l_A} \\ &= \sum_{i_A=0}^{l_A}\binom{l_A}{i_A}(x_P-x_A)^{l_A-i_A}(x-x_P)^{i_A} \end{aligned} \tag{2.43}$$

where x_P is arbitrary, and $\binom{l_A}{i_A}$ is a binomial coefficient. This can be extended to give

$$\begin{aligned}(x-x_A)^{l_A}(x-x_B)^{l_B} &= \sum_{i_A=0}^{l_A}\binom{l_A}{i_A}(x_P-x_A)^{l_A-i_A} \\ &\quad\times\sum_{i_B=0}^{l_B}\binom{l_B}{i_B}(x_P-x_B)^{l_B-i_B}(x-x_P)^{i_A+i_B} \\ &= \sum_{i_A=0}^{l_A}\sum_{i_B=0}^{l_B}\binom{l_A}{i_A}\binom{l_B}{i_B}(x_P-x_A)^{l_A-i_A}(x_P-x_B)^{l_B-i_B} \\ &\quad\times\sum_{k_x=0}^{l_A+l_B}(x-x_P)^{k_x} \\ &= \sum_{k_x=0}^{l_A+l_B} f_{k_x}(l_A,l_B,x_A,x_B)(x-x_P)^{k_x} \end{aligned} \tag{2.44}$$

where

$$f_{k_x}(l_A,l_B,x_A,x_B)=\sum_{i_A=0}^{l_A}\sum_{i_B=0}^{l_B}\binom{l_A}{i_A}\binom{l_B}{i_B}(x_P-x_A)^{l_A-i_A}(x_P-x_B)^{l_B-i_B}. \tag{2.45}$$

for the remainder of this section, $f_{k_x}(l_A,l_B,x_A,x_B)$ will be reduced to f_{k_x} for brevity. Using the procedure defined above for the y and z components of Equation 2.41 yields

$$\begin{aligned}G_A(\mathbf{r})G_B(\mathbf{r}) &= KN_AN_B\sum_{k_x=0}^{l_A+l_B} f_{k_x}(x-x_P)^{k_x}\sum_{k_y=0}^{m_A+m_B} f_{k_y}(y-y_P)^{k_y} \\ &\quad\times\sum_{k_z=0}^{n_A+n_B} f_{k_z}(z-z_P)^{k_z}\exp\left[-\gamma(\mathbf{r}-\mathbf{r}_P)^2\right] \end{aligned} \tag{2.46}$$

and the Gaussian product theorem takes on its most general form.

2.3.2 Rys Quadrature

Rys quadrature is a numerical method for evaluating integrals of the form

$$I = \int_0^1 t^{2m} \exp\left[-Xt^2\right] dt. \tag{2.47}$$

It will be shown in sections 2.3.5 and 2.3.6 that both the potential energy and Coulomb integrals can be reduced to this form, and so successful evaluation of Equation 2.47 will be sufficient for the evaluation of all necessary molecular integrals.

Rys quadrature, like any quadrature method, uses a set of polynomials orthogonal with respect to a certain weight function and over a certain range of integration. For the case of the Rys polynomials, $R_n(X,t)$, the weight function is

$$W(X,t) = \exp\left[-Xt^2\right], \tag{2.48}$$

and the range of integration is $0 < t < 1$. Any set of polynomials, orthogonal with respect to the weight function $W(x)$ over the interval $a < x < b$, have the following property [28];

$$\int_a^b p_\lambda(x)\, W(x)\, dx = \sum_{j=1}^{n} w_j f(x_j) + \epsilon, \tag{2.49}$$

where $p_\lambda(x)$ is a polynomial of order λ in x, and ϵ is a measure of the error in the numerical procedure $\epsilon = 0$ if $n > \lambda/2$, and so the evaluation of a given integral can be exact using this method. x_j is the jth abscissa of the nth order polynomial, and ω_j is an associated weight. For the 'classical' orthogonal polynomials, such as the Legendre, Hermite, or Chebychev polynomials, there are well known analytical expressions for obtaining these weights and abscissas (see, for example, Section 4.5 of [105]), but no such analytical method is known for the

Rys polynomials. Before this point is addressed, however, the construction of the Rys polynomials themselves will be considered. This is most easily achieved by constructing the set of polynomials $J_n(X,t)$, orthogonal with respect to the same weight function as the $R_n(X,t)$, but over the interval $-1 < t < 1$. The $J_n(X,t)$ are related to the $R_n(X,t)$ via

$$R_n(X,t) = \sqrt{2}J_{2n}(X,t), \tag{2.50}$$

and so it can be seen that the $R_n(X,t)$ are the set of even Rys polynomials, and can be thought of as functions of t^2.

Any set of monic orthogonal polynomials satisfy a three-term recurrence relationship [125], and this relationship will be easier to apply using the $J_n(X,t)$. The recurrence relationship is

$$J_{n+1}(X,t) = (t-\alpha_n)J_n(X,t) - \beta_n J_{n-1}(X,t), \tag{2.51}$$

where

$$\alpha_n = \frac{\int tJ_n^2(X,t)W(x,t)dt}{\int J_n^2(X,t)W(x,t)dt} \tag{2.52a}$$

$$\beta_n = \frac{\int J_n^2(X,t)W(x,t)dt}{\int J_{n-1}^2(X,t)W(x,t)dt}, \tag{2.52b}$$

with initial values $\beta_0 = \int W(X,t)dt$, $J_0 = 1$, and $J_{-1} = 0$. The recursion coefficients were calculated following the recommendation of Sagar and Smith [117]. This involves application of Fejér quadrature [47], for which the analytical form of the abscissas, x_j^N, and weights, s_j^N, are given by

$$x_j^N = \cos\left(\frac{(2j-1)\pi}{2N}\right) \tag{2.53a}$$

$$s_j^N = \frac{2}{N}\left(1 - 2\sum_{m=1}^{N/2}\frac{\cos(m(2j-1)\pi/N)}{4m^2-1}\right). \tag{2.53b}$$

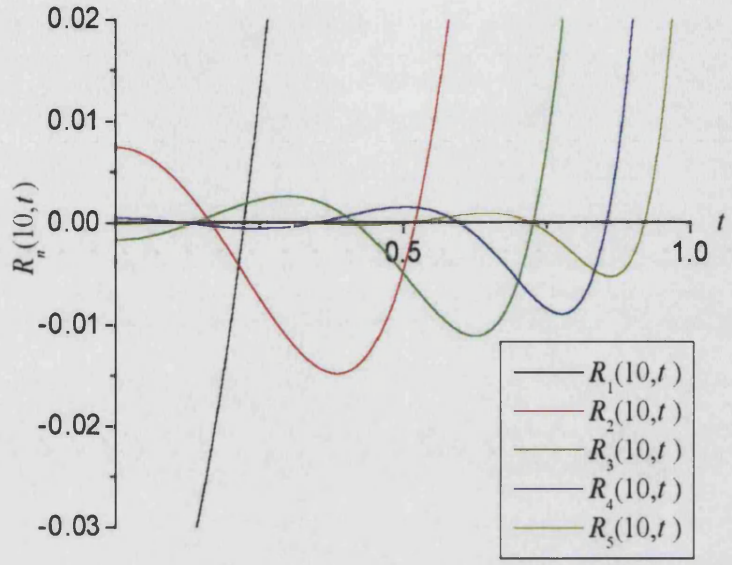

Figure 2.1: Rys polynomials $R_n(10,t)$, $n = 1, 2, 3, 4, 5$

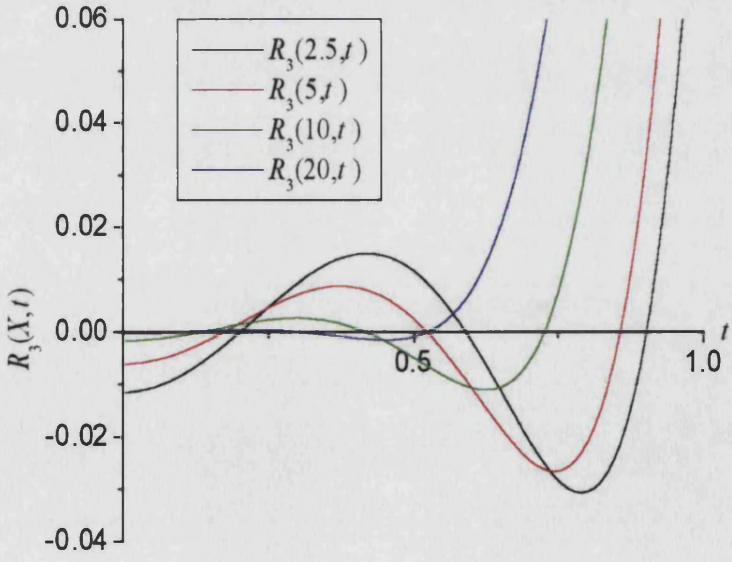

Figure 2.2: Rys polynomials $R_3(X,t)$, $X = 2.5, 5, 10, 20$

Equations 2.53a and 2.53b, along with Equation 2.49 can then be used to numerically evaluate α_n and β_n, with N being increased until convergence is achieved. The $J_n(X,t)$, and hence the $R_n(X,t)$, can then be calculated using Equation 2.51, and the Rys abscissas and weights can be evaluated using standard techniques [105]. Figures 2.1 and 2.2 show the dependence of the Rys polynomials on n and X.

2.3.3 The Overlap Integrals

The overlap integrals take the form

$$\begin{aligned} S_{AB} &= \int_{-\infty}^{\infty} G_A(\mathbf{r}) G_B(\mathbf{r}) d\mathbf{r} \\ &= \langle G_A | G_B \rangle , \end{aligned} \tag{2.54}$$

where $G_N(x)$ take the form of Equation 2.42. Applying the Gaussian product theorem of section 2.3.1 yields

$$S_{AB} = K N_A N_B U_x U_y U_z \tag{2.55}$$

where

$$U_q = \int_{-\infty}^{\infty} \sum_{k_q=0}^{(l_A^q + l_B^q)} f_{2k_q}(q - q_p)^{2k_q} \exp\left[-\gamma(q - q_p)^2\right] dq. \tag{2.56}$$

Here, terms for which k_q is odd have been dropped since these terms correspond to odd functions, and so their contribution over the range of integration will be zero. Now, making use of the standard integral

$$\begin{aligned} I &= \int_{-\infty}^{\infty} q^n \exp\left[-\alpha q^2\right] dq \\ &= \left(\frac{\pi}{\alpha}\right)^{1/2} \frac{(n-1)!!}{(2\alpha)^{n/2}} \end{aligned} \tag{2.57}$$

gives

$$U_q = \left(\frac{\pi}{\gamma}\right)^{1/2} \sum_{k_q=0}^{(l_A^q+l_B^q)} \frac{f_{2k_q}(2k_q-1)!!}{(2\gamma)^{k_q}}, \tag{2.58}$$

and so S_{AB} can be evaluated. A similar procedure can be applied to obtain the normalisation constants, giving

$$\frac{1}{N_A^2} = \left(\frac{\pi}{2\alpha}\right)^{3/2} \frac{(2l_A^x-1)!!(2l_A^y-1)!!(2l_A^z-1)!!}{(4\alpha)^{l_A^x+l_A^y+l_A^z}}. \tag{2.59}$$

2.3.4 The Kinetic Energy Integrals

The kinetic energy integrals are defined as

$$\begin{aligned} T_{AB} &= -\left\langle G_A(\mathbf{r}) \left| \frac{\nabla^2}{2} \right| G_B(\mathbf{r}) \right\rangle \\ &= \frac{1}{2} \langle \nabla G_A(\mathbf{r}) | \nabla G_B(\mathbf{r}) \rangle . \end{aligned} \tag{2.60}$$

Noting that the kinetic energy operator is spatially separable, i.e.

$$T_{AB} = T_{AB}^x + T_{AB}^y + T_{AB}^z, \tag{2.61}$$

where

$$T_{AB}^x = \frac{1}{2} \left\langle \frac{\partial}{\partial x} G_A(\mathbf{r}) \middle| \frac{\partial}{\partial x} G_B(\mathbf{r}) \right\rangle, \tag{2.62}$$

and similarly for T_{AB}^y and T_{AB}^z. Simplifying the notation to

$$G_A(\mathbf{r}) = |l_A^x, l_A^y, l_A^z\rangle \tag{2.63}$$

gives

$$\frac{\partial}{\partial x} G_A(\mathbf{r}) = l_A^x \, |l_A^x - 1, l_A^y, l_A^z\rangle - 2\alpha \, |l_A^x + 1, l_A^y, l_A^z\rangle , \tag{2.64}$$

and so

$$\begin{aligned} T_{AB}^x &= l_A^x l_B^x \langle l_A^x - 1, l_A^y, l_A^z | l_B^x - 1, l_B^y, l_B^z \rangle + 4\alpha\beta \langle l_A^x + 1, l_A^y, l_A^z | l_B^x + 1, l_B^y, l_B^z \rangle \\ &\quad -2\alpha l_B^x \langle l_A^x + 1, l_A^y, l_A^z | l_B^x - 1, l_B^y, l_B^z \rangle \\ &\quad -2\beta l_A^x \langle l_A^x - 1, l_A^y, l_A^z | l_B^x + 1, l_B^y, l_B^z \rangle . \end{aligned} \tag{2.65}$$

Similar results can be obtained for T_{AB}^{y} and T_{AB}^{z}, and so Equation 2.60 can be evaluated.

2.3.5 The Potential Energy Integrals

In atomic units, the potential energy integrals have the form

$$V_C = \left\langle G_A(\mathbf{r}) \left| |\mathbf{r} - \mathbf{r}_C|^{-1} \right| G_B(\mathbf{r}) \right\rangle, \tag{2.66}$$

and measure the potential energy between a point charge at $\mathbf{r}_C$ and the charge density defined by $G_A(\mathbf{r})G_B(\mathbf{r})$. Using the Laplace transform, and twice applying the Gaussian product theorem, allows the integral to be written as

$$V_C = \frac{KN_AN_B}{\sqrt{\pi}} \int_0^\infty \Lambda(\rho)\rho^{-1/2} J_x J_y J_z d\rho, \tag{2.67}$$

where

$$\begin{aligned} J_x &= \sum_{k_x=0}^{\left(l_A^x+l_B^x\right)/2} f_{2k_x} \int_{-\infty}^{\infty} (x - x_Q)^{2k_x} \exp\left[-\theta (x - x_Q)^2\right] dx \\ &= \left(\frac{\pi}{\theta}\right)^{1/2} \sum_{k_x=0}^{\left(l_A^x+l_B^x\right)/2} \frac{f_{2k_x}(2k_x - 1)!!}{(2\theta)^{k_x}} \end{aligned}$$

$$\begin{aligned} \Lambda(\rho) &= \exp\left[-\frac{\gamma\rho}{\theta}(\mathbf{r}_P - \mathbf{r}_C)^2\right] \\ \gamma &= \alpha + \beta \\ \theta &= \gamma + \rho \\ x_Q &= \frac{\alpha x_A + \beta x_B + \rho x_C}{\theta} \\ \mathbf{r}_P &= \frac{\alpha \mathbf{r}_A + \beta \mathbf{r}_B}{\gamma}, \end{aligned}$$

and J_y, J_z, y_Q, z_Q are defined similarly. Making the substitution $t^2 = \rho/(\rho + \gamma)$, and noting that $\theta = \gamma/(1 - t^2)$, gives

$$J_x = \left(\frac{\pi(1 - t^2)}{\gamma}\right)^{1/2} \sum_{k_x=0}^{\left(l_A^x+l_B^x\right)/2} \left(\frac{1 - t^2}{2\gamma}\right)^{k_x} f_{2k_x}(2k_x - 1)!! \tag{2.68}$$

and

$$V_C = \frac{2KN_AN_B}{\gamma\sqrt{\pi}} \int_0^1 \left(\frac{\gamma}{1-t^2}\right) \Lambda(t) J_x J_y J_z dt. \tag{2.69}$$

Letting $I_x = (\gamma/(1-t^2))^{1/2} J_x$ gives

$$V_C = \frac{2\pi KN_AN_B}{\gamma} \int_0^1 \Lambda(t) I_x I_y I_z dt. \tag{2.70}$$

Now, I_x is a polynomial of order $l_A^x + l_B^x$ in t, and similarly for I_y and I_z, therefore $I_x I_y I_z$ is a polynomial $P_\lambda(t)$ of order λ in t, where

$$\lambda = l_A^x + l_B^x + l_A^y + l_B^y + l_A^z + l_B^z, \tag{2.71}$$

and so

$$V_C = \frac{2\pi KN_AN_B}{\gamma} \int_0^1 P_\lambda(t) \exp\left[-Xt^2\right] dt, \tag{2.72}$$

where $X = \gamma\left(\mathbf{r}_P - \mathbf{r}_C\right)^2$. Equation 2.72 is of the form to which Rys quadrature can be directly applied, allowing V_C to be evaluated exactly.

2.3.6 The Coulomb Integrals

In atomic units, the Coulomb integrals are of the form

$$\begin{aligned} I_C &= \int_{-\infty}^{\infty}\int_{-\infty}^{\infty} G_A(\mathbf{r}_1) G_B(\mathbf{r}_1) \left|\mathbf{r}_1 - \mathbf{r}_2\right|^{-1} G_C(\mathbf{r}_2) G_D(\mathbf{r}_2) d\mathbf{r}_1 d\mathbf{r}_2 \\ &= (AB|CD), \end{aligned} \tag{2.73}$$

and measure the average potential energy between two charge densities described by the coordinates $\mathbf{r}_1$ and $\mathbf{r}_2$ respectively. Applying the Laplace transform, and the Gaussian product theorem to G_AG_B and G_CG_D gives

$$I_C = \frac{K_{AB}K_{CD}N_AN_BN_CN_D}{\sqrt{\pi}} \int_0^\infty \rho^{-1/2} U_x U_y U_z d\rho, \tag{2.74}$$

where

$$U_x = \int_{-\infty}^{\infty}\int_{-\infty}^{\infty} (x_1 - x_A)^{l_A^x} (x_1 - x_B)^{l_B^x} (x_2 - x_C)^{l_C^x} (x_2 - x_D)^{l_D^x} \exp\left[-\rho(x_1 - x_2)^2 - \varepsilon_1 (x_1 - x_P)^2 - \varepsilon_2 (x_2 - x_Q)^2\right] d\mathbf{r}_1 d\mathbf{r}_2$$

$$\begin{aligned} \varepsilon_1 &= \alpha + \beta \\ \varepsilon_2 &= \gamma + \delta \\ x_P &= \frac{\alpha x_A + \beta x_B}{\varepsilon_1} \\ x_Q &= \frac{\gamma x_C + \delta x_D}{\varepsilon_2}. \end{aligned}$$

Applying the Gaussian product theorem twice more gives

$$I_C = \frac{KN}{\sqrt{\pi}} \int_0^{\infty} \rho^{-1/2} \exp\left[-\frac{\theta\rho\,(\mathbf{r}_P - \mathbf{r}_Q)^2}{\theta + \rho}\right] J_x J_y J_z d\rho, \tag{2.75}$$

where $\theta = \varepsilon_1\varepsilon_2/(\varepsilon_1 + \varepsilon_2)$, and $KN = K_{AB}K_{CD}N_AN_BN_CN_D$. Making the transformation $t^2 = \rho/(\theta + \rho)$, J_x can be evaluated as

$$\begin{aligned} J_x = &\left(\frac{\pi^2}{\eta_1\eta_2}\right)^{1/2} \sum_{k_{x_2}=0}^{(l_C^x + l_D^x)/2} \frac{(2k_{x_2} - 1)!!}{(2\eta_2)^{k_{x_2}}} \sum_{i_C=0}^{l_C} \sum_{i_D=0}^{l_D} \binom{l_C}{i_C} \binom{l_D}{i_D} \\ &\times \sum_{k_{x_1}=0}^{(L - i_C - i_D)/2} \frac{f_{2k_{x_1}} (2k_{x_1} - 1)!!}{(2\eta_1)^{k_{x_1}}} \left(\frac{\rho}{\eta_2}\right)^{l_C + l_D - i_C - i_D} \end{aligned} \tag{2.76}$$

where

$$\begin{aligned} f_{k_{x_1}} = &\sum_{i_A=0}^{l_A} \sum_{i_B=0}^{l_B} \sum_{j_C=0}^{l_C - i_C} \sum_{j_D=0}^{l_D - i_D} \binom{l_A}{i_A} \binom{l_B}{i_B} \binom{l_C - i_C}{j_C} \binom{l_D - i_D}{j_D} (\overline{x}_1 - x_A)^{l_A - i_A} \\ &\times (\overline{x}_1 - x_B)^{l_B - i_B} (\overline{x}_1 - \chi_1)^{l_C - i_C - j_C} (\overline{x}_1 - \chi_2)^{l_D - i_D - j_D} \end{aligned} \tag{2.77}$$

$$
\begin{aligned}
k_{x_1} &= i_A + i_B + j_C + j_D \\
L &= l_A + l_B + l_C + l_D \\
\eta_1 &= \varepsilon_1 + \frac{\rho\varepsilon_2}{\rho + \varepsilon_2} \\
\eta_2 &= \rho + \varepsilon_2 \\
\overline{x}_1 &= \frac{(\gamma x_C + \delta x_D + \varepsilon_2 x_P)\, t^2}{\varepsilon_1 + \varepsilon_2} + x_P \\
\chi_1 &= \frac{\delta(x_C - x_D)(1 - t^2)}{\theta t^2} + x_C \\
\chi_2 &= \frac{\gamma(x_D - x_C)(1 - t^2)}{\theta t^2} + x_D.
\end{aligned}
$$

Letting $I_x = \sqrt{\eta_1\eta_2}J_x$, and similarly for J_y and J_z gives

$$
I_C = \frac{2KN}{(\varepsilon_1\varepsilon_2)^{3/2}} \left(\frac{\theta}{\pi}\right)^{1/2} \int_0^1 I_x I_y I_z \exp\left[-Xt^2\right] dt, \tag{2.78}
$$

where $X = \theta\left(\mathbf{r}_P - \mathbf{r}_Q\right)^2$, and, with $I_x I_y I_z$ being an even polynomial in t, Rys quadrature can be directly applied.

Computational Considerations

Although the formulae given in Sections 2.3.3 - 2.3.6 are sufficient to evaluate all molecular integrals needed in a self-consistent field calculation, there are some computational factors which should be considered. In particular, for relatively small basis sets, such as the 6-31G set used throughout this thesis, angular momenta numbers are never larger than $l_n = 1$, and so the computationally costly multiple summations required for the evaluation of the 1-dimensional integrals I_n can be reduced dramatically, and in some cases removed altogether. In addition, symmetries in the basis function can be exploited to rapidly identify non-contributing integrals. Finally the limiting behaviour of terms of the form $m = (x_P - x_A)^{l_A - i_A}$, which arise during application of the Gaussian product theorem, should be considered. For $x_A = x_B$, it can be readily seen that

$x_P - x_A = 0$, and so, for $l_A - i_A = 0$, indeterminate values of m are encountered. The limiting behaviour is easily seen to be that, for $l_A - i_A = 0$, $m \rightarrow 1$ as $x_P - x_A \rightarrow 0$.

The numerical accuracy of the solutions to the molecular integrals presented in Sections 2.3.3 - 2.3.6 were verified using Mathematica, and found to be accurate to $\sim$ 12 decimal places.

2.4 Herring's Formula in Three Dimensions

Herring's formula was originally derived [61] for the purpose of obtaining a zeroth order approximation to the singlet-triplet splitting in the H_2 molecule. The same approach can be used to obtain an estimate of the tunnel-splitting energy in a symmetric double potential well. This energy is a measure of the splitting between the lowest energy states in the presence of a finite barrier between the two wells, and can be related to the probability of a tunnelling event occurring [87]. The original derivation of Herring's formula only considers a one-dimensional potential, but this thesis requires a three-dimensional version of the formula. This formula can then be used to estimate the tunnel-splitting energy of a hydrogen-like nucleus in the presence of more than one identical potential energy minima. The following two sections show the derivation these forms of Herring's formula for the first time.

2.4.1 The Double Potential Well

The derivation presented here follows that of Landau and Lifshitz [76], but extends the approach to encompass three dimensions. Consider the two functions

$$\varphi_S = \frac{1}{\sqrt{2}} \left[\varphi_L(x,y,z) + \varphi_R(x,y,z) \right] \tag{2.79a}$$

$$\varphi_A = \frac{1}{\sqrt{2}} \left[\varphi_L(x,y,z) - \varphi_R(x,y,z) \right], \tag{2.79b}$$

where there is a plane of symmetry between φ_L and φ_R. These functions represent the zeroth order approximation to ground and first excited states of the symmetric double potential well, and it is assumed that the product $\varphi_L \varphi_R$ is vanishingly small everywhere. Under this approximation, two Schrödinger equations can be defined. In atomic units, these are

$$\nabla^2 \varphi_R(x,y,z) + 2m(E_R - U)\varphi_R = 0 \tag{2.80a}$$

$$\nabla^2 \varphi_S(x,y,z) + 2m(E_S - U)\varphi_S = 0, \tag{2.80b}$$

where m is the mass of the tunnelling particle, U represents the double potential well, E_R gives the energy of the particle when confined to one well, and E_S gives the energy of the symmetric ground state described by Equation 2.79a. Multiplying Equation 2.80a by φ_S, Equation 2.80b by φ_R, and rearranging yields

$$\varphi_S \nabla^2 \varphi_R - \varphi_R \nabla^2 \varphi_S = -2m(E_R - E_S)\varphi_R \varphi_S. \tag{2.81}$$

With no loss of generality, the system can be rotated so that the plane of symmetry between φ_L and φ_R is the $y-z$ plane, and the plane intersects the x-axis at $x = 0$. In this case we have the relationship

$$\varphi_R(x,y,z) = \varphi_L(-x,y,z). \tag{2.82}$$

Equation 2.81 is valid over all space, and so there is freedom in the range of integration used to evaluate $E_R - E_S$. Choosing the ranges $0 \leq x \leq \infty$, $-\infty \leq y \leq \infty$, $-\infty \leq z \leq \infty$ gives

$$\begin{aligned} &\int_{-\infty}^{\infty}\int_{-\infty}^{\infty}\int_{0}^{\infty} \left(\varphi_S \nabla^2 \varphi_R - \varphi_R \nabla^2 \varphi_S \right) dx\, dy\, dz \\ &= -2m(E_R - E_S) \int_{-\infty}^{\infty}\int_{-\infty}^{\infty}\int_{0}^{\infty} \varphi_R \varphi_S \, dx\, dy\, dz. \end{aligned} \tag{2.83}$$

Now, since $\varphi_L\varphi_R$ is vanishingly small everywhere,

$$\begin{aligned}\varphi_R\varphi_S &= \frac{1}{\sqrt{2}}\varphi_R(\varphi_L+\varphi_R)\\ &\simeq \frac{1}{\sqrt{2}}\varphi_R^2 \end{aligned} \tag{2.84}$$

and so the right hand side of Equation 2.83 can be evaluated as

$$\begin{aligned}2m(E_R-E_S)\int_{-\infty}^{\infty}\int_{-\infty}^{\infty}\int_{0}^{\infty}\varphi_R\varphi_S\,dx\,dy\,dz &\simeq \sqrt{2}m(E_R-E_S)\int_{-\infty}^{\infty}\int_{-\infty}^{\infty}\int_{0}^{\infty}\varphi_R^2\,dx\,dy\,dz\\ &= \sqrt{2}m(E_R-E_S).\end{aligned} \tag{2.85}$$

The left hand side of Equation 2.83 can be rewritten

$$\begin{aligned}&\int_{-\infty}^{\infty}\int_{-\infty}^{\infty}\int_{0}^{\infty}\left(\varphi_S\nabla^2\varphi_R-\varphi_R\nabla^2\varphi_S\right)\,dx\,dy\,dz\\ =\;&\int_{-\infty}^{\infty}\int_{-\infty}^{\infty}\int_{0}^{\infty}\left(\frac{\partial^2\varphi_R}{\partial x^2}\varphi_S-\varphi_R\frac{\partial^2\varphi_S}{\partial x^2}\right)+\left(\frac{\partial^2\varphi_R}{\partial y^2}\varphi_S-\varphi_R\frac{\partial^2\varphi_S}{\partial y^2}\right)\\ &+\left(\frac{\partial^2\varphi_R}{\partial z^2}\varphi_S-\varphi_R\frac{\partial^2\varphi_S}{\partial z^2}\right)\,dx\,dy\,dz,\end{aligned} \tag{2.86}$$

and the first term on the right hand side of Equation 2.86 can be evaluated by considering the one dimensional integral

$$\begin{aligned}\int_0^{\infty}\left(\frac{\partial^2\varphi_R}{\partial x^2}\varphi_S-\varphi_R\frac{\partial^2\varphi_S}{\partial x^2}\right)dx &= \left[\frac{\partial\varphi_R}{\partial x}\varphi_S-\varphi_R\frac{\partial\varphi_S}{\partial x}\right]_{x=0}^{x=\infty}\\ &\quad-\int_0^{\infty}\frac{\partial\varphi_R}{\partial x}\frac{\partial\varphi_S}{\partial x}-\frac{\partial\varphi_S}{\partial x}\frac{\partial\varphi_R}{\partial x}\,dx\\ &= -\left[\frac{\partial\varphi_R}{\partial x}\varphi_S-\varphi_R\frac{\partial\varphi_S}{\partial x}\right]_{x=0}.\end{aligned} \tag{2.87}$$

Since φ_S is a symmetric function with respect to x,

$$\left[\frac{\partial\varphi_S}{\partial x}\right]_{x=0}=0 \tag{2.88}$$

and

$$\begin{aligned}\varphi_S|_{x=0} &= \frac{1}{\sqrt{2}}\left(\varphi_L|_{x=0} + \varphi_R|_{x=0}\right) \\ &= \sqrt{2}\varphi_R|_{x=0}. \end{aligned} \tag{2.89}$$

This gives

$$\begin{aligned}&\int_{-\infty}^{\infty}\int_{-\infty}^{\infty}\int_{0}^{\infty}\left(\frac{\partial^2\varphi_R}{\partial x^2}\varphi_S - \varphi_R\frac{\partial^2\varphi_S}{\partial x^2}\right)dx\,dy\,dz \\ = \; &-\sqrt{2}\int_{-\infty}^{\infty}\int_{-\infty}^{\infty}\varphi_R(0,y,z)\frac{\partial\varphi_R(0,y,z)}{\partial x}\,dy\,dz, \end{aligned} \tag{2.90}$$

where the notation is obvious. The second and third terms can be evaluated in a similar manner;

$$\begin{aligned}&\int_{-\infty}^{\infty}\int_{-\infty}^{\infty}\int_{0}^{\infty}\left(\frac{\partial^2\varphi_R}{\partial y^2}\varphi_S - \varphi_R\frac{\partial^2\varphi_S}{\partial y^2}\right)dx\,dy\,dz \\ = \; &\int_{-\infty}^{\infty}\int_{0}^{\infty}\left(\left[\frac{\partial\varphi_R}{\partial y}\varphi_S - \varphi_R\frac{\partial\varphi_S}{\partial y}\right]_{y=-\infty}^{y=\infty} + \int_{0}^{\infty}\frac{\partial\varphi_R}{\partial y}\frac{\partial\varphi_S}{\partial y} - \frac{\partial\varphi_S}{\partial y}\frac{\partial\varphi_R}{\partial y}\,dy\right)dx\,dz \\ = \; &0, \end{aligned} \tag{2.91}$$

and so Equation 2.83 can be rewritten as

$$(E_R - E_S) = \frac{1}{m}\int_{-\infty}^{\infty}\int_{-\infty}^{\infty}\varphi_R(0,y,z)\frac{\partial\varphi_R(0,y,z)}{\partial x}\,dy\,dz. \tag{2.92}$$

A similar equation to Equation 2.80b can be defined for φ_A, yielding $(E_A - E_R) = -(E_S - E_R)$, and so the tunnel-splitting energy ΔE can be written as

$$\Delta E = E_A - E_S = \frac{2}{m}\int_{-\infty}^{\infty}\int_{-\infty}^{\infty}\varphi_R(0,y,z)\frac{\partial\varphi_R(0,y,z)}{\partial x}\,dy\,dz. \tag{2.93}$$

The time evolution of the wavefunction of a particle localised in one of the wells at $t = 0$, i.e.

$$\varphi(x,y,z,0) = \frac{1}{\sqrt{2}}\left[\varphi_S(x,y,z) + \varphi_A(x,y,z)\right] \tag{2.94}$$

can be written in atomic units as [87]

$$\varphi(x,y,z,t) = \exp\left[-\frac{i}{2}(E_S+E_A)t\right]\times \left(\frac{\varphi_S+\varphi_A}{\sqrt{2}}\cos\left(\frac{\Delta E}{2}t\right)+i\frac{\varphi_S-\varphi_A}{\sqrt{2}}\sin\left(\frac{\Delta E}{2}t\right)\right), \quad (2.95)$$

and so it can be clearly seen that after a period given by

$$\tau = 2\pi/\Delta E \quad (2.96)$$

the particle has tunnelled from the original well into the other, and back again. A tunnelling frequency can therefore be associated with the tunnel splitting energy.

2.4.2 The Triple Potential Well

A three-dimensional version of Herrings formula can also be derived for the case of a particle tunnelling between three identical potentials located on the vertices of a equilateral triangle. Again, the ground state and lowest energy excited states can be constructed as linear combinations of the localised functions corresponding to the solution of the single potential well Schrödinger equation. These states are

$$\varphi_S = \frac{1}{\sqrt{3}}\left[\varphi_a(x,y,z)+\varphi_b(x,y,z)+\varphi_c(x,y,z)\right] \quad (2.97a)$$

$$\varphi_{A1} = \frac{1}{\sqrt{2}}\left[\varphi_a(x,y,z)-\varphi_b(x,y,z)\right] \quad (2.97b)$$

$$\varphi_{A2} = \frac{1}{\sqrt{6}}\left[\varphi_a(x,y,z)+\varphi_b(x,y,z)-2\varphi_c(x,y,z)\right]. \quad (2.97c)$$

The derivation of the tunnel-splitting energy in this case will be made much easier by first considering the nature of the splitting about the ground state energy, E_0, of a particle localised in one of the wells. In the case of the double potential well, the nature of the splitting is easily seen to be symmetric about

E_0 since, from Equations ?? and ??, it can be seen that the expectation values of the Hamiltonian are given by

$$\begin{aligned} E_S &= \frac{1}{2}\left(\left\langle \varphi_L \middle| \widehat{H} \middle| \varphi_L \right\rangle + \left\langle \varphi_R \middle| \widehat{H} \middle| \varphi_R \right\rangle + 2\left\langle \varphi_L \middle| \widehat{H} \middle| \varphi_R \right\rangle\right) \\ &= E_0 + J \qquad (2.98a) \\ E_A &= \frac{1}{2}\left(\left\langle \varphi_L \middle| \widehat{H} \middle| \varphi_L \right\rangle + \left\langle \varphi_R \middle| \widehat{H} \middle| \varphi_R \right\rangle - 2\left\langle \varphi_L \middle| \widehat{H} \middle| \varphi_R \right\rangle\right) \\ &= E_0 - J, \qquad (2.98b) \end{aligned}$$

where $\left\langle \varphi_L \middle| \widehat{H} \middle| \varphi_L \right\rangle = \left\langle \varphi_R \middle| \widehat{H} \middle| \varphi_R \right\rangle = E_0$, and the tunnel-splitting energy, ΔE, is given by

$$\Delta E = 2J = 2\left\langle \varphi_L \middle| \widehat{H} \middle| \varphi_R \right\rangle. \qquad (2.99)$$

Applying the same procedure to the triple well, we obtain

$$\begin{aligned} E_S &= \frac{1}{3}\left(\left\langle \varphi_a \middle| \widehat{H} \middle| \varphi_a \right\rangle + \left\langle \varphi_b \middle| \widehat{H} \middle| \varphi_b \right\rangle + \left\langle \varphi_c \middle| \widehat{H} \middle| \varphi_c \right\rangle \right. \\ &\quad \left. +2\left\langle \varphi_a \middle| \widehat{H} \middle| \varphi_b \right\rangle + 2\left\langle \varphi_a \middle| \widehat{H} \middle| \varphi_c \right\rangle + 2\left\langle \varphi_b \middle| \widehat{H} \middle| \varphi_c \right\rangle\right) \\ &= E_0 + 2J \qquad (2.100a) \\ E_{A1} &= \frac{1}{2}\left(\left\langle \varphi_a \middle| \widehat{H} \middle| \varphi_a \right\rangle + \left\langle \varphi_b \middle| \widehat{H} \middle| \varphi_b \right\rangle - 2\left\langle \varphi_a \middle| \widehat{H} \middle| \varphi_b \right\rangle\right) \\ &= E_0 - J \qquad (2.100b) \\ E_{A2} &= \frac{1}{6}\left(\left\langle \varphi_a \middle| \widehat{H} \middle| \varphi_a \right\rangle + \left\langle \varphi_b \middle| \widehat{H} \middle| \varphi_b \right\rangle + 4\left\langle \varphi_c \middle| \widehat{H} \middle| \varphi_c \right\rangle \right. \\ &\quad \left. +2\left\langle \varphi_a \middle| \widehat{H} \middle| \varphi_b \right\rangle - 4\left\langle \varphi_a \middle| \widehat{H} \middle| \varphi_c \right\rangle - 2\left\langle \varphi_b \middle| \widehat{H} \middle| \varphi_c \right\rangle\right) \\ &= E_0 - J, \qquad (2.100c) \end{aligned}$$

and so it can be seen that in the case of the triple well, the tunnel splitting is not symmetric about the ground state, but consists of a ground state $2J$ below the single well ground-state, with a doubly degenerate 1st excited state of energy J above the ground state.

Equation 2.100b has the same form as Equation 2.98b, and so a pair of Schrödinger equations analogous to Equations 2.80a and 2.80b can be constructed for the triple well. The energy separation between E_0 and the excited states will be identical to that for the double well, since the potential U is eliminated in Equation 2.81. The energy difference between E_0 and the symmetric ground state is double the magnitude of this, and so the tunnel splitting energy can be written as

$$\Delta E = E_{A1} - E_S = E_{A2} - E_S = \frac{3}{m} \int_{-\infty}^{\infty} \int_{-\infty}^{\infty} \varphi_R(0,y,z) \frac{\partial \varphi_R(0,y,z)}{\partial x} \, dy \, dz. \quad (2.101)$$

Equation 2.101 shows an amplification of the tunnel-splitting energy, and hence the tunneling rate of a particle in a triple potential well compared to that in a double well. This amplification can be attributed to the fact that there are two distinct diffusion pathways in the triple well system, and so during the vibrational motion of a particle trapped in a single well, a higher proportion of tunnelling events can occur.

The time evolution of the three well system is not as a simple as that of the two well system. Here, a particle initially localised in any one given well will never localise completely in any other well. However, it is still correct to say that if a particle is localised in any given well at $t = 0$, then the particle will continue to localise in this well with the period given by Equation 2.96, and so a tunnelling frequency can still be associated with the tunnel-splitting energy.

As will be shown in Section 3.3, ΔE is a very good approximation to the exact tunnel-splitting energy for physically realistic φ_S and φ_R. Herring's formula is particularly useful in that it allows an evaluation of the tunnel splitting energy using only the symmetric ground state. Since the accurate evaluation of excited states is very difficult using self-consistent field techniques, Herring's formula

becomes very valuable here. Herring's formula is also useful in models where the electronic motion cannot be correlated to that of a tunnelling hydrogen-like nucleus, such as in the parametrised correlation model presented later in this thesis.

Chapter 3

Analytical Examples; The Harmonic Oscillator

The harmonic oscillator is a powerful analytical tool in quantum mechanics, with a Hamiltonian for which the Schrödinger equation has straightforward yet non-trivial solutions. Intractable problems, simplified and recast in a form to which these solutions can be applied, can be used to reveal general physical properties of systems of interest. For example, this approach has been used to better understand the errors introduced by the application of the Born-Oppenheimer and Hartree-Fock approximations [91, 92]. In this chapter, the harmonic oscillator will be used to illustrate physical phenomena relevant to this thesis. Firstly, it will be used to study the behaviour of the variational method when isotropic functions are used to model anisotropic functions. Secondly, the harmonic oscillator will be used to derive exact analytical expressions for the one tunnel-splitting energy, allowing a critical study of Herring's formula [61] to be made. Finally, and of most importance, the calculations of [92] will be extended to allow a detailed study of the behaviour of the electron-nuclear correlation energy as a function of nuclear mass, of great importance in the remainder of this thesis.

3.1 General Solution to the Harmonic Oscillator Schrödinger Equation

In three dimensions the harmonic oscillator Hamiltonian is defined (in atomic units) as

$$\widehat{H} = -\frac{\nabla^2}{2m} + \frac{1}{2}m(\omega_x^2 x^2 + \omega_y^2 y^2 + \omega_z^2 z^2). \tag{3.1}$$

This can separated into three one-dimensional Hamiltonians, corresponding to simple harmonic motion in that dimension. For each of these we have the Schrödinger equation

$$\left(-\frac{1}{2m}\frac{\partial^2}{\partial i^2} + \frac{1}{2}m(\omega_i^2 i^2)\right)\varphi_n(i) = E_{ni}\varphi_n(i), \tag{3.2}$$

and the solution to this equation gives an infinite set of eigenstates of equally spaced energies

$$\varphi_n(i) = N_n H_n(\sqrt{\alpha}i)\exp[-\alpha i^2], \qquad E_{ni} = \left(n + \frac{1}{2}\right)\omega_i \tag{3.3}$$

in atomic units, where $H_n(\sqrt{\alpha}i)$ is the Hermite polynomial of degree n. Of particular interest is the ground state harmonic oscillator wavefunction, a Gaussian function given by

$$\varphi_0(i) = \left(\frac{m\omega}{\pi}\right)^{\frac{1}{4}}\exp\left[-\frac{m\omega_i i^2}{2}\right], \qquad E_0 = \frac{\omega_i}{2}. \tag{3.4}$$

Gaussians are often used as the primitive basis functions in electronic structure calculations. These functions allows for the exact evaluation of four centre, two particle integrals, a necessary requirement in *ab initio* calculations.

3.2 The Variational Method

In this section, the quality of an isotropic two dimensional harmonic oscillator wavefunction (i.e. one for which $\omega_x = \omega_y$) as an approximation to an anisotropic

wavefunction (for which $\omega_x \neq \omega_y$), will be discussed. We take as our starting point Equations 3.2 and 3.4. Applying the variational method with a trial wavefunction $\varphi(x) = \exp[-\alpha x^2]$ would yield the exact ground state wavefunction, with $\alpha = m\omega/2$. Now consider the two dimensional harmonic oscillator, with the Hamiltonian

$$\widehat{H}_{2D} = -\frac{1}{2m}\left(\frac{\partial^2}{\partial x^2} + \frac{\partial^2}{\partial y^2}\right) + \frac{m}{2}\left(\omega_x^2 x^2 + \omega_y^2 y^2\right). \tag{3.5}$$

The ground state for this Hamiltonian is given by

$$\varphi_0(x,y) = \left(\frac{m}{\pi}\right)^{\frac{1}{2}} (\omega_x\omega_y)^{\frac{1}{4}} \exp\left[-\frac{m}{2}\left(\omega_x x^2 + \omega_y y^2\right)\right], \qquad E_0 = \frac{\omega_x + \omega_y}{2}, \tag{3.6}$$

allowing different degrees of localisation in the x and y directions. If an isotropic trial wavefunction

$$\varphi_t(x,y) = \left(\frac{m\omega}{\pi}\right)^{\frac{1}{2}} \exp\left[-\frac{m\omega}{2}\left(x^2 + y^2\right)\right] \tag{3.7}$$

is used, then the energy of this function $E_t \geq E_0$, is given by

$$E_t = \left\langle \varphi_t(x,y) \middle| \widehat{H} \middle| \varphi_t(x,y) \right\rangle. \tag{3.8}$$

Now, both the Hamiltonian and the trial wavefunction can be separated into their respective x and y components, and so

$$E_t = E_{tx} + E_{ty} = \left\langle \varphi_t(x) \middle| \widehat{H}_x \middle| \varphi_t(x) \right\rangle + \left\langle \varphi_t(y) \middle| \widehat{H}_y \middle| \varphi_t(y) \right\rangle. \tag{3.9}$$

These expectation values can also be separated into kinetic and potential energy terms, giving

$$T_{tx} = \frac{\omega}{4} \tag{3.10a}$$

$$T_{ty} = \frac{\omega}{4} \tag{3.10b}$$

$$V_{tx} = \frac{\omega_x^2}{4\omega} \tag{3.10c}$$

$$V_{ty} = \frac{\omega_y^2}{4\omega} \tag{3.10d}$$

giving

$$E_t = \frac{1}{4\omega}\left(2\omega^2 + \omega_x^2 + \omega_y^2\right), \tag{3.11}$$

and

$$E_t - E_0 = \frac{1}{4\omega}\left((\omega - \omega_x)^2 + (\omega - \omega_y)^2\right). \tag{3.12}$$

E_t is minimised by finding

$$\frac{dE_t}{d\omega} = 1 - \frac{1}{4\omega^2}\left(2\omega^2 + \omega_x^2 + \omega_y^2\right) = 0, \tag{3.13}$$

which is satisfied by

$$\omega = \sqrt{\frac{\omega_x^2 + \omega_y^2}{2}}. \tag{3.14}$$

Figure 3.1 shows the variation of ω, and therefore of the energy, of the isotropic

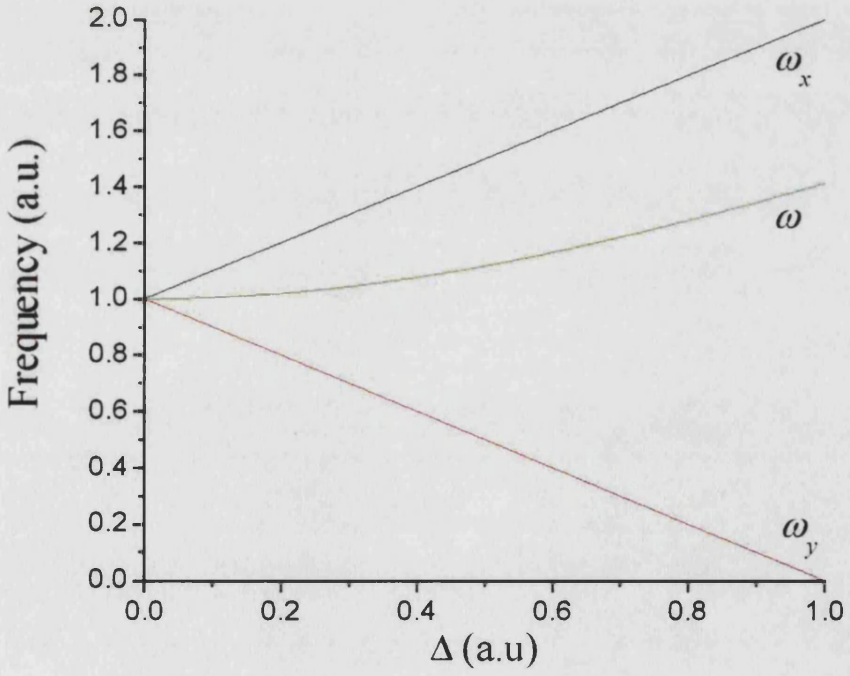

Figure 3.1: Comparison of ω, ω_x, and ω_y as functions of Δ

approximation to the anisotropic wavefunction as the difference between ω_x and ω_y is increased. Letting

$$\omega_x = \omega_m + \Delta, \tag{3.15a}$$

$$\omega_y = \omega_m - \Delta, \tag{3.15b}$$

gives

$$\omega = \sqrt{\omega_m^2 + \Delta^2}, \tag{3.16}$$

and it can be clearly seen that as the difference between ω_x and ω_y increases, so the variationally optimal frequency ω favours the higher frequency ω_x. This feature of the variational method shows that in a system where the potential energy is not an isotropic function, e.g. in the case of the potential energy along and across a molecular bond, the variational energy will be minimised by a function favouring the more localising potential. This further implies that with a small basis set, but one which adequately spans the parameter space of each potentials well, it would be expected that the more energetic components of a given state would be better approximated.

3.3 The Tunnel Splitting Energy

Consider the 1D potential energy function

$$V(x) = \frac{1}{2} m\omega^2 \left(|x| - x_0\right)^2 . \tag{3.17}$$

This function (see Figure 3.2) describes a double potential well separated by a barrier of height $V_0 = \frac{1}{2} m\omega^2 x_0^2$. A sensible set of trial wavefunctions would therefore be

$$\varphi_+(x) = \frac{1}{\sqrt{2(1+S_{AB})}} \left(\varphi_A(x) + \varphi_B(x)\right) \tag{3.18a}$$

$$\varphi_-(x) = \frac{1}{\sqrt{2(1-S_{AB})}} \left(\varphi_A(x) - \varphi_B(x)\right) \tag{3.18b}$$

where

$$\varphi_A(x) = \left(\frac{m\omega}{\pi}\right)^{\frac{1}{4}} \exp\left[-\frac{1}{2}m\omega\left(x - x_0\right)^2\right] \tag{3.19a}$$

$$\varphi_B(x) = \left(\frac{m\omega}{\pi}\right)^{\frac{1}{4}} \exp\left[-\frac{1}{2}m\omega\left(x + x_0\right)^2\right] \tag{3.19b}$$

and

$$S_{AB} = \int \varphi_A(x)\varphi_B(x)\, dx. \tag{3.20}$$

φ_+ and φ_- are therefore the symmetric and antisymmetric combinations of the exact solutions to the Schrödinger equation for the harmonic oscillator potentials $V(x) = \frac{1}{2}m\omega^2\left(x \pm x_0\right)^2$. In the limit $x_0 \to \infty$, φ_+ and φ_- are the exact solutions to the Schrödinger equation for the potential of Equation 3.17. The tunnel splitting energy ΔE is defined as

$$\Delta E = E_- - E_+ \tag{3.21}$$

where

$$E_- = \left\langle \varphi_+ \middle| \widehat{H} \middle| \varphi_+ \right\rangle \tag{3.22a}$$

$$E_- = \left\langle \varphi_- \middle| \widehat{H} \middle| \varphi_- \right\rangle \tag{3.22b}$$

$$\widehat{H} = -\frac{1}{2m}\frac{d^2}{dx^2} + \frac{1}{2}m\omega^2\left(|x| - x_0\right)^2. \tag{3.23}$$

The Hamiltonian can, of course, be separated into kinetic and potential energy contributions and so the tunnel splitting energy can be expressed as

$$\Delta E = \Delta T + \Delta V = \left(T_- - T_+\right) + \left(V_- - V_+\right). \tag{3.24}$$

Letting $\chi = \sqrt{m\omega}x_0$, the kinetic energy term is given by

$$\begin{aligned} \Delta T &= \frac{S_{AB}}{m(1 - S_{AB}^2)} \int \varphi_B'(x)\varphi_B'(x)\, dx - \frac{1}{m(1 - S_{AB}^2)} \int \varphi_A'(x)\varphi_B'(x)\, dx \\ &= \frac{\omega\chi^2 \exp[\chi^2]}{\exp[2\chi^2] - 1}, \end{aligned} \tag{3.25}$$

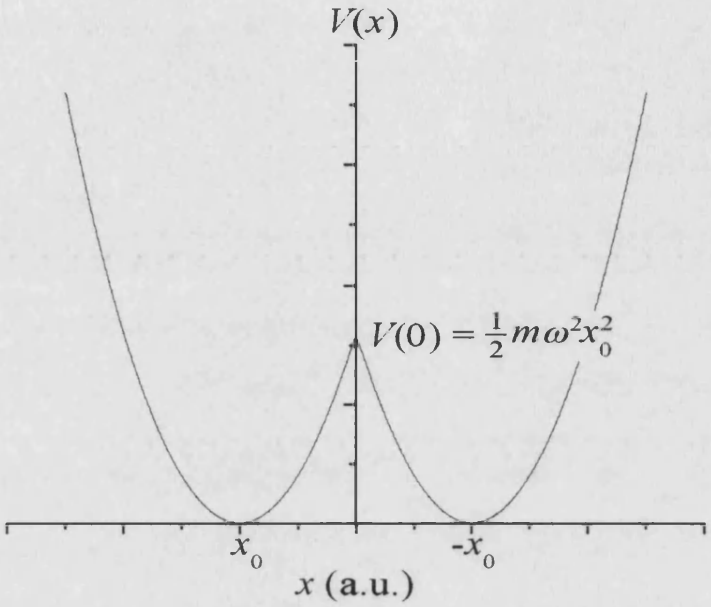

Figure 3.2: The double potential well described by Equation 3.17.

and the potential energy term by

$$\begin{aligned}\Delta V &= -2m\omega \int (|x| - x_0)^2 \, \varphi_A(x)\varphi_B(x) \, dx \\ &= \frac{2\omega}{\sqrt{\pi}} \frac{\chi\,(\exp[\chi^2] - 1)}{\exp[2\chi^2] - 1} + \frac{2\omega\chi^2 \exp[\chi^2]\,(1 - 2\,\mathrm{erf}[\chi])}{\exp[2\chi^2] - 1}. \end{aligned} \tag{3.26}$$

This gives for the tunnel splitting energy

$$\Delta E = \frac{2\omega}{\sqrt{\pi}} \frac{\chi}{1 + \exp[\chi^2]} + \frac{2\omega\chi^2 \exp[\chi^2](1 - \mathrm{erf}[\chi])}{\exp[2\chi^2] - 1}. \tag{3.27}$$

For large χ, ($x_0 \gg (m\omega)^{-\frac{1}{2}}$), Equation 3.27 reduces to

$$\Delta E = \frac{2\omega\chi}{\sqrt{\pi}} \exp[-\chi^2], \tag{3.28}$$

which equals the value for the tunnel splitting (in a.u.) given by Herring's formula [61]

$$\Delta E = \frac{2}{m} \varphi_A(0)\varphi'_A(0). \tag{3.29}$$

Method	ΔE (a.u.)	ΔE (eV)
Numerical	2.364×10^{-4}	6.433×10^{-3}
Analytical	2.320×10^{-4}	6.318×10^{-3}
Herring's Formula	2.322×10^{-4}	6.314×10^{-3}

Table 3.1: Tunnel splitting energy for the double harmonic potential well

Figure 3.3 shows the two lowest energy numerical solutions to the Schrödinger equation for the potential of Equation 3.17 with $\omega = 0.01$ a.u., $m = 206.7683$ a.u., and $x_0 = 1.5$ a.u. This value of m is the muon mass, and the values of ω and x_0 are those for which physically realistic energies can be obtained. Table 3.1 shows the tunnel splitting energy for this system as calculated numerically, and using Equations 3.27 and 3.28. This shows that Herring's formula is a good approximation to the analytical tunnel splitting energy for the parameters described above. Furthermore, Table 3.1 shows that the basis chosen for these calculations is highly accurate. Figure 3.4 shows how Equations 3.27 and 3.28 behave with $\omega = 0.01$ a.u. and $m = 206.7683$ a.u. as x_0 is varied. As $x_0 \to 0$, and the potential barrier tends to zero, the analytical solution gives $\Delta E = 0.01$ a.u. This is in fact the difference in energy between the first excited and ground states, as would be expected since the double harmonic well reverts to a single harmonic well in the limit $x_0 \to 0$. Figure 3.4 also shows the zero point energy and barrier height for this system, and a tunnel splitting energy can only be defined for this system when the barrier height is greater than the zero point energy, which occurs for $\chi > 1$. For values of $\chi \gtrsim 1.5$, Herring's formula gives a good estimate of the tunnel splitting energy. In Section 2.4, Herring's formula is derived in three dimensions, but in this case, since the eigenvalues of the system are separable, the contributions to the energy in the y and z directions cancel.

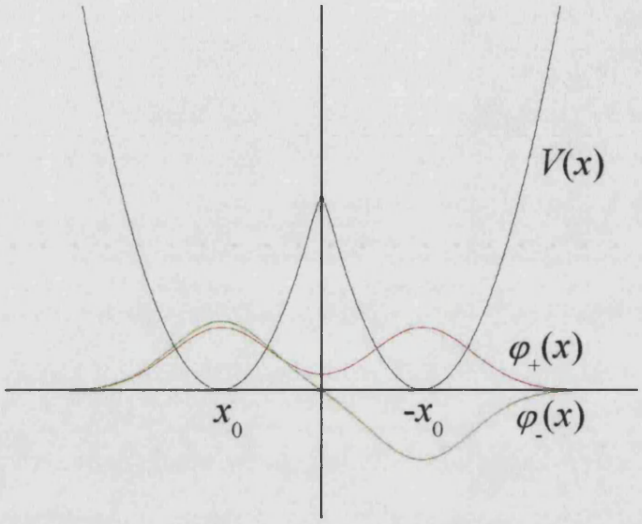

Figure 3.3: Symmetric (φ_+) and antisymmetic (φ_-) wavefunctions for the double harmonic potential well. The potential energy surface $V(x)$ is shown as a guide to the eye

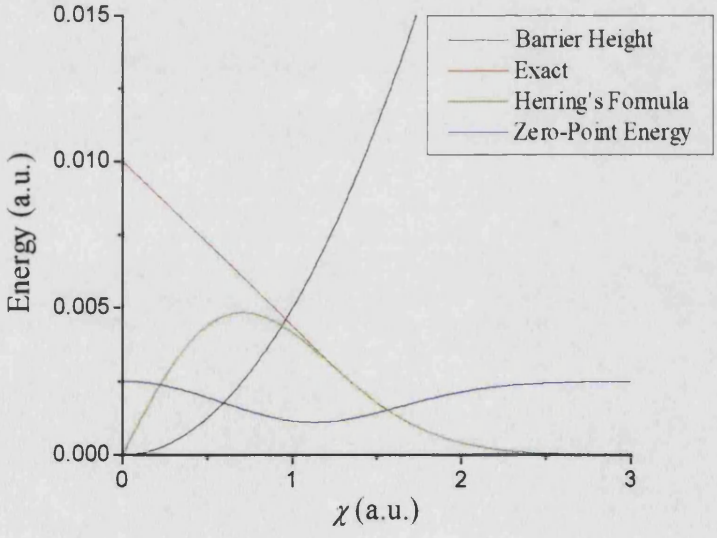

Figure 3.4: Comparison of the exact tunnel-splitting energy and that calculated using Herring's formula

3.4 The Correlation Energy

The correlation energy cannot be evaluated analytically for particles interacting through a Coulombic potential. However, as shown by Moshinsky and Kittel [92], if the particles are coupled harmonically, then the correlation energy can be calculated exactly. Furthermore, the total energy of the system can be evaluated within the Hartree-Fock framework, allowing for a quantitative analysis of the error induced using this approximation. The starting point for this calculation is the Hamiltonian

$$\widehat{H} = -\frac{\nabla_1^2}{2m_1} - \frac{\nabla_2^2}{2m_2} + \frac{1}{2}k\mathbf{r}_1^2 + \frac{1}{2}k\mathbf{r}_2^2 + \frac{\gamma}{2}(\mathbf{r}_1 - \mathbf{r}_2)^2. \tag{3.30}$$

The solution to the Schrödinger equation for this Hamiltonian describes two particles of masses m_1 and m_2 respectively, moving in a common harmonic potential of spring constant k, and coupled via the parameter γ. The following sections present the exact and Hartree-Fock solutions to the Schrödinger equation for this Hamiltonian.

3.4.1 Exact Solution

To solve the equation

$$\widehat{H}_E\varphi_E(\mathbf{r}_1, \mathbf{r}_2) = E_E\varphi_E(\mathbf{r}_1, \mathbf{r}_2), \tag{3.31}$$

where $\widehat{H}_E$ is that of Equation 3.30, the Hamiltonian must first be diagonalised. Making the transformation of variables

$$\mathbf{r}_1' = \sqrt{m_1}\mathbf{r}_1 \tag{3.32a}$$

$$\mathbf{r}_2' = \sqrt{m_2}\mathbf{r}_2 \tag{3.32b}$$

transforms the Hamiltonian to

$$\widehat{H} = -\frac{\nabla_1'^2}{2} - \frac{\nabla_2'^2}{2} + \frac{k}{2m_1}\mathbf{r}_1'^2 + \frac{k}{2m_2}\mathbf{r}_2'^2 + \frac{\gamma}{2}\left(\frac{\mathbf{r}_1'}{\sqrt{m_1}} - \frac{\mathbf{r}_2'}{\sqrt{m_2}}\right)^2. \tag{3.33}$$

The coefficients of the potential energy term can be expressed in matrix form as

$$c_v = \begin{bmatrix} \frac{k+\gamma}{2m_1} & \frac{-\gamma}{2\sqrt{m_1 m_2}} \\ \frac{-\gamma}{2\sqrt{m_1 m_2}} & \frac{k+\gamma}{2m_2} \end{bmatrix},$$

with eigenvectors $\mathbf{r}_A$ and $\mathbf{r}_B$ given by

$$\mathbf{r}_A = \frac{1}{n_A}\left(\frac{2(m_1 - m_2)(k+\gamma) + \sigma}{\eta}\mathbf{r}_1' + \mathbf{r}_2'\right) \tag{3.34a}$$

$$\mathbf{r}_B = \frac{1}{n_B}\left(\frac{2(m_1 - m_2)(k+\gamma) - \sigma}{\eta}\mathbf{r}_1' + \mathbf{r}_2'\right) \tag{3.34b}$$

where

$$n_A = \sqrt{1 + \frac{\left(2(m_1 - m_2)(k+\gamma) + \sigma\right)^2}{\eta^2}} \tag{3.35a}$$

$$n_B = \sqrt{1 + \frac{\left(2(m_1 - m_2)(k+\gamma) - \sigma\right)^2}{\eta^2}} \tag{3.35b}$$

$$\sigma = \sqrt{4(m_1 + m_2)^2(k+\gamma)^2 - 16km_1m_2(k+2\gamma)} \tag{3.35c}$$

$$\eta = 4\sqrt{m_1 m_2}\gamma. \tag{3.35d}$$

The potential energy term of Equation 3.33 is diagonalised by this transformation to $\mathbf{r}_A$ and $\mathbf{r}_B$ and can be written as

$$V(\mathbf{r}_A, \mathbf{r}_B) = \frac{1}{2}k_A\mathbf{r}_A^2 + \frac{1}{2}k_B\mathbf{r}_B^2, \tag{3.36}$$

where

$$k_A = \frac{(m_1 + m_2)(k+\gamma)\sigma - \chi}{2m_1m_2\sigma} \tag{3.37a}$$

$$k_B = \frac{(m_1 + m_2)(k+\gamma)\sigma + \chi}{2m_1m_2\sigma}, \tag{3.37b}$$

with

$$\chi = \left(2(m_1 - m_2)^2(k+\gamma)^2 + 8m_1m_2\gamma^2\right) \tag{3.38}$$

The Hamiltonian can then be written as

$$\begin{aligned} \widehat{H}_E &= \widehat{H}_A + \widehat{H}_B \\ &= -\frac{\nabla_A^2}{2} + \frac{1}{2}k_A\mathbf{r}_A^2 - \frac{\nabla_B^2}{2} + \frac{1}{2}k_B\mathbf{r}_B^2. \end{aligned} \tag{3.39}$$

and the Schrödinger equation has a solution of the form

$$\varphi_E(\mathbf{r}_A, \mathbf{r}_B) = \varphi_A(\mathbf{r}_A)\varphi_B(\mathbf{r}_B), \tag{3.40}$$

where

$$\varphi_A(\mathbf{r}_A) = \left(\frac{k_A}{\pi^2}\right)^{\frac{3}{8}} \exp\left[-\frac{\sqrt{k_A}\mathbf{r}_A^2}{2}\right] \tag{3.41a}$$

$$\varphi_B(\mathbf{r}_B) = \left(\frac{k_B}{\pi^2}\right)^{\frac{3}{8}} \exp\left[-\frac{\sqrt{k_B}\mathbf{r}_B^2}{2}\right], \tag{3.41b}$$

and N_A and N_B are normalisation constants. Transforming back to the original coordinates gives for the final wavefunction

$$\varphi_E(\mathbf{r}_1, \mathbf{r}_2) = N_{12} \exp\left[-\left(\alpha_{11}\mathbf{r}_1^2 + \alpha_{22}\mathbf{r}_2^2 + \alpha_{12}\mathbf{r}_1 \cdot \mathbf{r}_2\right)\right], \tag{3.42}$$

where

$$\alpha_{11} = \sqrt{\frac{m_1}{m_2}}\left((2+\vartheta\sigma)\frac{\zeta_-}{16} + (2-\vartheta\sigma)\frac{\zeta_+}{16}\right) \tag{3.43}$$

$$\alpha_{22} = \sqrt{\frac{m_2}{m_1}}\left((2-\vartheta\sigma)\frac{\zeta_-}{16} + (2+\vartheta\sigma)\frac{\zeta_+}{16}\right) \tag{3.44}$$

$$\alpha_{12} = \frac{2\sqrt{m_1m_2}\gamma}{\zeta_- + \zeta_+}, \tag{3.45}$$

and

$$\vartheta = \frac{(m_1 - m_2)k}{(m_1+m_2)^2(k+\gamma)^2 - 4k(m_1m_2)(k+2\gamma)} \tag{3.46a}$$

$$\zeta_+ = \sqrt{2(m_1+m_2)(k+\gamma) + \sigma} \tag{3.46b}$$

$$\zeta_- = \sqrt{2(m_1+m_2)(k+\gamma) - \sigma}. \tag{3.46c}$$

Although unwieldy, these terms are presented in full here to allow verification of certain limiting cases. Under the condition $m_1 = m_2 = m$, Equation 3.42 simplifies to

$$\varphi_E(\mathbf{r}_1, \mathbf{r}_2) = N_{12} \exp\left[-\frac{1}{4}\left(\sqrt{km}(\mathbf{r}_1 + \mathbf{r}_2)^2 + \sqrt{(k+2\gamma)m}(\mathbf{r}_1 - \mathbf{r}_2)^2\right)\right], \quad (3.47)$$

in agreement with [91]. In the limit $\gamma \to 0$, where particles 1 and 2 decouple, Equation 3.42 simplifies to

$$\varphi_E(\mathbf{r}_1, \mathbf{r}_2) = N_{12} \exp\left[-\frac{1}{2}\left(\sqrt{km_1}\mathbf{r}_1^2 + \sqrt{km_2}\mathbf{r}_2^2\right)\right], \quad (3.48)$$

as would be expected since the Hamiltonian of Equation 3.30 separates in this limit.

The energy of the two-particle system described by Equation 3.42 can now be evaluated, and is given by

$$\begin{aligned} E_E &= \frac{3}{2}\left(\sqrt{k_A} + \sqrt{k_B}\right) \\ &= \frac{3}{4\sqrt{m_1 m_2}}\left(\zeta_+ + \zeta_-\right). \end{aligned} \quad (3.49)$$

3.4.2 Hartree-Fock Solution

Under the Hartree-Fock approximation, it is assumed from the outset that the two particle wavefunction can be written as the product of two one particle wavefunctions, i.e.

$$\varphi_{HF}(\mathbf{r}_1, \mathbf{r}_2) = \varphi_1(\mathbf{r}_1)\varphi_2(\mathbf{r}_2). \quad (3.50)$$

The particles satisfy the equations

$$\widehat{H}^{(2)}_{\mathbf{r}_1}\varphi_1(\mathbf{r}_1) = \varepsilon_1\varphi_1(\mathbf{r}_1) \quad (3.51a)$$

$$\widehat{H}^{(1)}_{\mathbf{r}_2}\varphi_2(\mathbf{r}_2) = \varepsilon_2\varphi_2(\mathbf{r}_2). \quad (3.51b)$$

where

$$\widehat{H}^{(n)}_{\mathbf{r}_l} = \left(-\frac{\nabla_l^2}{2m_l} + \frac{1}{2}k\mathbf{r}_l^2 + \frac{\gamma}{2}\int \varphi_n^*(\mathbf{r}_n)\left(\mathbf{r}_l - \mathbf{r}_n\right)^2 \varphi_n(\mathbf{r}_n)d\mathbf{r}_n\right) \tag{3.52}$$

Expanding the integral gives

$$\begin{aligned}\int \varphi_n^*(\mathbf{r}_n)\left(\mathbf{r}_l - \mathbf{r}_n\right)^2 \varphi_n(\mathbf{r}_n)d\mathbf{r}_n &= \int \varphi_n^*(\mathbf{r}_n)\mathbf{r}_n^2\varphi_n(\mathbf{r}_n)d\mathbf{r}_n \\ &\quad +\mathbf{r}_l^2\int \varphi_n^*(\mathbf{r}_n)\varphi_n(\mathbf{r}_n)d\mathbf{r}_n \\ &\quad -2\mathbf{r}_l\int \varphi_n^*(\mathbf{r}_n)\mathbf{r}_n\varphi_n(\mathbf{r}_n)d\mathbf{r}_n \\ &= c_n + \mathbf{r}_l^2, \end{aligned} \tag{3.53}$$

assuming that the particles are localised at $\mathbf{r} = 0$, which is ensured by the presence of the external potential. Equations 3.51a and 3.51b then reduce to

$$\left(-\frac{\nabla_1^2}{2m_1} + \frac{1}{2}\left(k+\gamma\right)\mathbf{r}_1^2\right)\varphi_1(\mathbf{r}_1) = \left(\varepsilon_1 - \frac{\gamma c_2}{2}\right)\varphi_1(\mathbf{r}_1) \tag{3.54}$$

$$\left(-\frac{\nabla_2^2}{2m_2} + \frac{1}{2}\left(k+\gamma\right)\mathbf{r}_2^2\right)\varphi_2(\mathbf{r}_2) = \left(\varepsilon_2 - \frac{\gamma c_1}{2}\right)\varphi_2(\mathbf{r}_2). \tag{3.55}$$

The full ground state solution in the Hartree-Fock approximation is then given by

$$\begin{aligned}\varphi_{HF}(\mathbf{r}_1,\mathbf{r}_2) &= \left(\frac{k+\gamma}{\pi^2}\right)^{\frac{3}{4}}(m_1m_2)^{\frac{3}{8}} \times \\ &\quad \exp\left[-\frac{1}{2}\sqrt{k+\gamma}\left(\sqrt{m_1}\mathbf{r}_1^2 + \sqrt{m_2}\mathbf{r}_2^2\right)\right], \end{aligned} \tag{3.56}$$

which, in the limit $\gamma \to 0$, simplifies to

$$\varphi_{HF}(\mathbf{r}_1,\mathbf{r}_2) = \left(\frac{k}{\pi^2}\right)^{\frac{3}{4}}(m_1m_2)^{\frac{3}{8}}\exp\left[-\frac{1}{2}\left(\sqrt{km_1}\mathbf{r}_1^2 + \sqrt{km_2}\mathbf{r}_2^2\right)\right], \tag{3.57}$$

in agreement with Equation 3.48. This is to be expected, since in this limit the particles are decoupled, and so only experience the external potential.

The energy of the two-particle system described by Equation 3.56 can now be evaluated, and is given by

$$\begin{aligned} E_{HF} &= \frac{3\sqrt{k+\gamma}}{2}\left(\frac{1}{\sqrt{m_1}}+\frac{1}{\sqrt{m_2}}\right) \\ &= \frac{3}{2}\sqrt{\frac{k+\gamma}{m_1 m_2}}\left(\sqrt{m_1}+\sqrt{m_2}\right). \end{aligned} \tag{3.58}$$

similarities between Equations 3.49 and 3.58 can be observed, but little simplification is possible when the correlation energy $E_C = E_{HF} - E_E$ is evaluated. Therefore, in Section 3.4.4, the exact and Hartree-Fock energies will be calculated numerically in order for the dependence of the correlation energy on particle mass to be identified. It can be seen, however, that if $m_2 \gg m_1$, both E_E and E_{HF} show a $m_2^{-1/2}$ dependence, and so the correlation energy would be expected to have the same form.

3.4.3 Comparison of the Wavefunctions

Figure 3.5 shows the variation of the overlap $\langle\varphi_E|\varphi_{HF}\rangle$ with the ratio of the coupling of the particles to each other and to the environment, γ/k.

As can be seen, the Hartree-Fock wavefunction is least accurate for $m_2 = m_\mu$, i.e. the approximation becomes better as the heavier particle increases in mass. This is to be expected since a heavier particle will have a more localised wavefunction, and so less kinetic energy. This implies that the correlation energy ignored in the Hartree-Fock approximation will be smaller since this energy term arises from the correlated motion of the *two* particles. If one particle is static, this term is zero. The difference between the exact and Hartree-Fock wavefunctions is shown in Figure 3.6. These plots were generated for $\gamma = 1$, $k = 0.1$, values that will be shown in Section 3.4.4 to give wavefunctions with physically realistic energies. It should be noted that for clarity the wavefunctions have been plotted

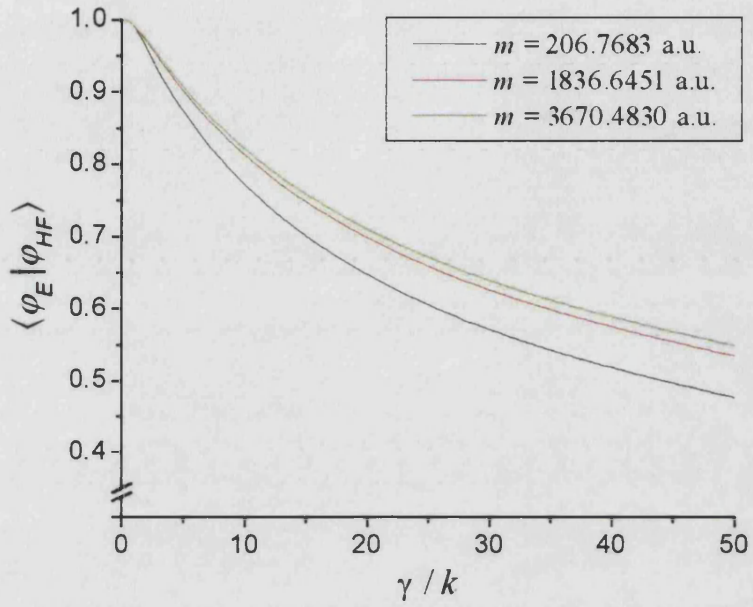

Figure 3.5: Variation of the overlap $\langle \varphi_E | \varphi_{HF} \rangle$ with γ/k for $m_2 = \{m_\mu, m_\mathrm{p}, m_\mathrm{d}\}$

over all four quadrants of the $\mathbf{r}_1 - \mathbf{r}_2$ plane. In fact the wavefunctions are only defined for $\mathbf{r}_1, \mathbf{r}_2 > 0$. As can be seen, the exact wavefunction shows the correlated motion of the two particles, which manifests itself as an increase in the two-particle density along the $\mathbf{r}_1 = \mathbf{r}_2$ axis when compared to the uncorrelated Hartree-Fock wavefunction. This correlation can be seen graphically to diminish as the ratio of the particle masses increases, as discussed above.

3.4.4 Comparison of the System Energies

The overlaps shown in Figure 3.5 are independent of the values of k and γ, and only depend upon their ratio. The energies, however, are dependent on the specific values of k and γ, and so realistic estimates of these parameters must be made to ensure that the correlation energies calculated are themselves physically

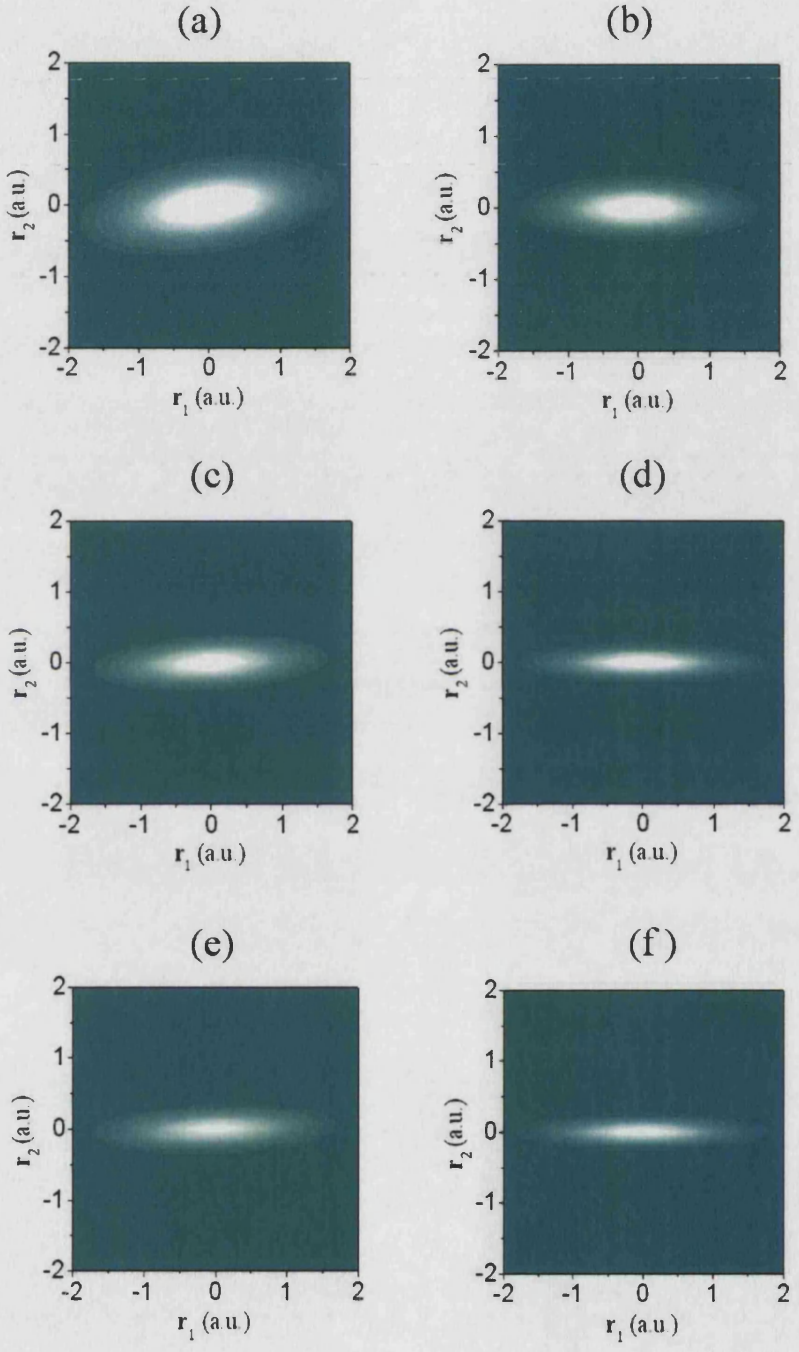

Figure 3.6: Comparison of exact (a,c,e) and Hartree-Fock (b,d,f) wavefunctions for $m_2 = m_\mu$ (a,b), $m_2 = m_\mathrm{p}$ (c,d), and $m_2 = m_\mathrm{d}$ (e,f)

realistic. The coupling parameter γ can be estimated by finding

$$\left\langle \varphi_E \left| \widehat{H} \right| \varphi_E \right\rangle_{k=0} \sim 0.5. \tag{3.59}$$

This gives the coupling between the two particles that, in the absence of an external potential, gives the energy of the electronic ground state for the hydrogen atom. This approximation makes the valid assumption that the kinetic energy of the heavier particle is negligible in comparison to other energies. In the limit that $m_2 \rightarrow \infty$ (and the kinetic energy of the heavier particle tends to zero), then, setting $\mathbf{r}_2 = 0$,

$$\varphi_E = \exp\left[-\frac{\sqrt{m_1\gamma}}{2}\mathbf{r}_1^2\right] \tag{3.60}$$

and, with $k = 0$;

$$\widehat{H} = -\frac{\nabla_1^2}{2m_1} + \frac{1}{2}\gamma\mathbf{r}_1^2. \tag{3.61}$$

The expectation value of Equation 3.59 is then given by

$$\left\langle \varphi_E \left| \widehat{H} \right| \varphi_E \right\rangle_{k=0} = \frac{1}{2}\sqrt{\frac{\gamma}{m_1}}. \tag{3.62}$$

Setting this equal to $E = 0.5$, and solving for γ gives

$$\begin{aligned} \gamma &= 4E^2 m_1 \\ &= 1. \end{aligned} \tag{3.63}$$

This value for γ can be used, along with experimental data, to estimate a value for k. A typical zero-point energy for a particle of mass $m = m_\mu$ would be $ZPE_\mu \sim 0.02$ a.u. This zero-point energy can be evaluated, with $\gamma = 1$, for a range of values of k, and furthermore, γ can itself be varied to ensure that the value obtained for k is robust against inaccuracy in the value of γ, which could arise, for example, if the electron density associated with the nucleus is less than unity. Table 3.2 summarises these calculations, and suggests that $k = 0.1$ is a

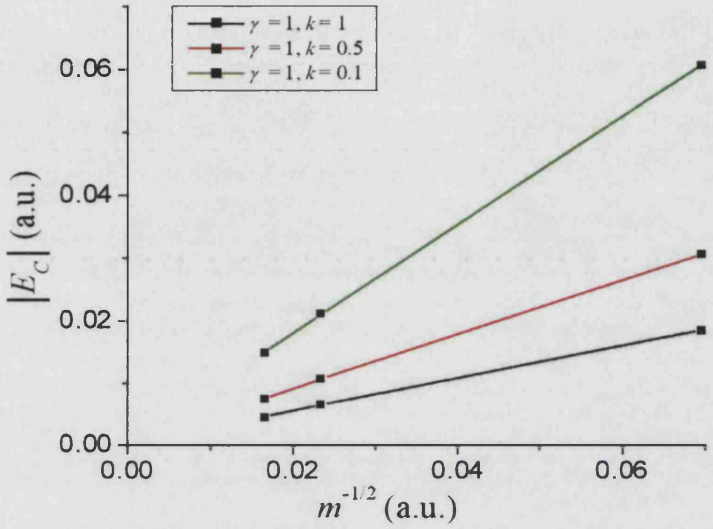

Figure 3.7: Variation of the correlation energy E_C with coupling parameter and particle mass

good approximation. The exact, Hartree-Fock, and correlation energies can now be evaluated. Table 3.3 gives these energies. For completeness, energies for a range of environment couplings have been calculated, in addition to energies for the uncoupled system, for which the correlation energy is zero. The variation of the correlation energy with coupling parameter and particle mass can be seen in Figure 3.7. Irrespective of the coupling parameters, the correlation energy is related to the mass of the heavier particle by

$$E_C \propto \frac{1}{m_2^{\frac{1}{2}}}, \tag{3.64}$$

as expected. Such a simple relationship suggests that something correspondingly simple may be apparent when a Coulombic interaction replaces the harmonic one, although the actual power dependence may differ.

It can be seen in Table 3.3 that the correlation energy is small when compared

γ	k	ZPE_μ (a.u.)
1	0.5	0.0418
1	0.1	0.0189
1	0.05	0.0134
0.5	0.5	0.0409
0.5	0.1	0.0189
0.5	0.05	0.0133
0.1	0.5	0.0385
0.1	0.1	0.0183
0.1	0.05	0.0132

Table 3.2: Variation of ZPE_μ with k and γ

γ	k	m_2 (a.u.)	E_E (a.u.)	E_{HF} (a.u.)	E_C (a.u.)
1	1	m_μ	2.25029	2.26885	0.01856
1	1	m_p	2.16433	2.17082	0.00649
1	1	m_d	2.15172	2.15634	0.00462
1	0.5	m_μ	1.93422	1.96488	0.03066
1	0.5	m_p	1.86929	1.87998	0.01069
1	0.5	m_d	1.85983	1.86744	0.00761
1	0.1	m_μ	1.62185	1.68262	0.06078
1	0.1	m_p	1.58886	1.60992	0.02107
1	0.1	m_d	1.58421	1.59918	0.01497
0	1	m_μ	1.60432	1.60432	0
0	1	m_p	1.53500	1.53500	0
0	1	m_d	1.52476	1.52476	0

Table 3.3: Exact, Hartree-Fock, and correlation energies for different values of k and γ

γ	k	m_2 (a.u.)	ZPE_E (a.u.)	ZPE_{HF} (a.u.)
1	1	m_μ	0.0579	0.0738
1	1	m_p	0.0201	0.0247
1	1	m_d	0.0144	0.0175
1	0.5	m_μ	0.0418	0.0639
1	0.5	m_p	0.0146	0.0214
1	0.5	m_d	0.0105	0.0152
1	0.1	m_μ	0.0189	0.0547
1	0.1	m_p	0.0066	0.0184
1	0.1	m_d	0.0048	0.0130

Table 3.4: Exact and Hartree-Fock zero-point energies for different values of k and γ

to the total system energy. Of more interest is a comparison of the exact and Hartree-Fock zero-point energies of the heavier particle, where the importance of correlation effects is highlighted. These energies are shown in Table 3.4. For $\gamma = 1$, $k = 0.5$, the exact zero-point energy is approximately three times that of the Hartree-Fock case. Since this energy is directly proportional to the vibrational frequency of the particle, this shows that vibrational frequencies of particles of mass $10^2 - 10^3$ a.u. will be over-estimated by a factor of three in the Hartree-Fock approximation. The degree of this overlocalisation of the particle can be seen in Figure 3.8. Interestingly, the effect of correlation on a particle of electron mass is much less pronounced, suggesting that the Hartree-Fock approximation is sufficiently accurate to allow the evaluation of electron densities, even when the electron is allowed to interact with a quantum-mechanically described HLN.

The results presented in this chapter will be of great use when a self-consistent field model is used to evaluate the HLN wavefunction when the HLN is coupled to the electron density through the Coulomb interaction. The information gained regarding the behaviour of variational method will allow a more appro-

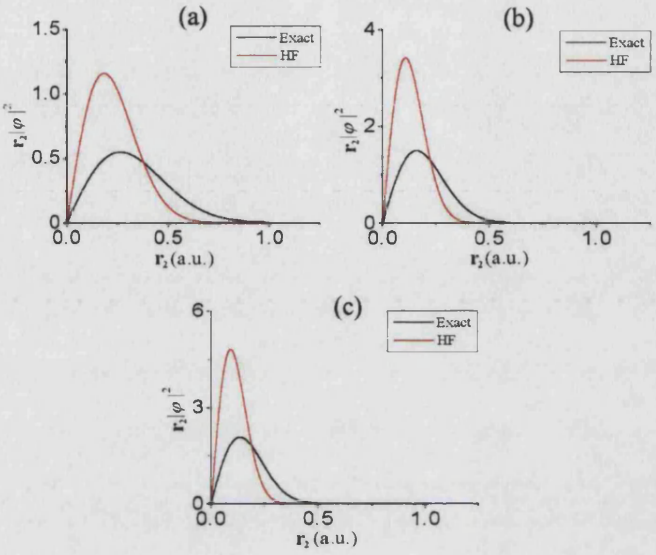

Figure 3.8: Exact and Hartree-Fock radial probability distributions for a) $m_2 = m_\mu$, b) $m_2 = m_\mathrm{p}$, and c) $m_2 = m_\mathrm{d}$. The overlocalisation of the Hartree-Fock distributions can be clearly seen.

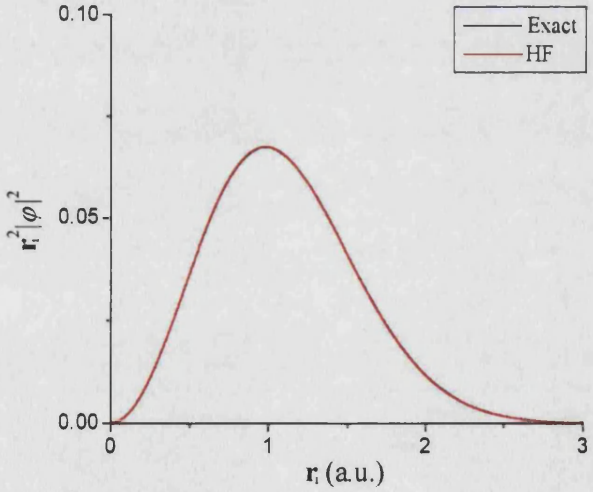

Figure 3.9: Exact and Hartree-Fock radial probability distribution for a particle of electron mass harmonically coupled to a particle of muon mass. The overlocalisation seen in Figure 3.8 is much less pronounced here, with the curve representing the exact distribution being covered by that representing the HF solution.

priate basis set to be chosen for the SCF calculations. The tunnel-splitting energy calculations ensures that Herring's formula can be trusted to give accurate tunnel-splitting energies (assuming the wavefunctions are themselves accurate). Finally, the calculations regarding the correlation energies suggests that similar features and trends may be present in the Coulombic model, and illustrates the huge correlation effects that are present when particles of such different masses interact.

Chapter 4

A Parametrised Correlation Model

4.1 Anharmonicity in the potential

When attempting to solve the Schrödinger equation for the hydrogen-like nucleus (HLN), a description of the potential energy experienced by the particle is required. The total energy of a 1-D system can be expanded in a Taylor series about the equilibrium position of the nucleus x_0 as

$$V(x) = V(x_0) + (x - x_0)V'(x_0) + \frac{(x - x_0)^2}{2}V''(x_0) + \frac{(x - x_0)^3}{3!}V'''(x_0) + \ldots \quad (4.1)$$

in which the terms first order in displacement vanish since the force on the particle is equal to zero at the equilibrium geometry. The retention of only the second order term leads to the harmonic approximation, for which the ground state solution to the Schrödinger equation takes the form of Equation 3.4. If other terms in the potential energy are retained, solutions become more complicated, and in general the Schrödinger equation becomes intractable. These other terms describe the anharmonicity in the potential energy surface, and of most interest here are the odd terms in $V(x)$ which give an asymmetric potential energy surface. This is typically the case for a model potential describing the variation in energy along a bond between two nuclei. Figure 4.1 shows the effect of this

anharmonicity on both the eigenfunctions and energies of a particle. The asymmetry in the potential is reflected in an asymmetry in the eigenfunction, leading to a mass dependent increase in the equilibrium bond length. The energies of these states are also affected, with the energy separation between successively higher states tending to zero as the dissociation energy E_d is approached.

Two approaches can be taken in choosing localised basis sets to describe this asymmetric wavefunction. A single centre approach can be taken, in which the asymmetry of the wavefunction is modelled by using basis functions with angular momentum numbers $l_x > 0$ (where x gives the bond direction), or alternatively, a multi-centre approach can be taken using only spherically symmetric Gaussians. In this approach the basis consists of a set of functions positioned on more than one centre along the bond. A linear combination of these basis functions is then used to model the asymmetry.

4.2 Hartree-Fock Calculations on the Reference Systems

Before the parametrised correlation model is presented, it is worth considering the results of Hartree-Fock calculations made on the set of reference systems used for the parametrisation. These calculations were made using Gaussian 98 [45] at the unrestricted Hartree-Fock level, using a 6-31G basis set. The calculations essentially take the form presented in Section 2.1.1. Modifications to Gaussian 98 have been made in order to allow the evaluation of the two-particle integrals between distinguishable particles, using the integration methods described in Section 2.3.2. These modifications allow the matrix elements of Equation 2.34 (assuming $V_X = 0$) to be evaluated, and standard routines [105] have been used to allow the resulting eigenvalue equation to be solved. This yields both

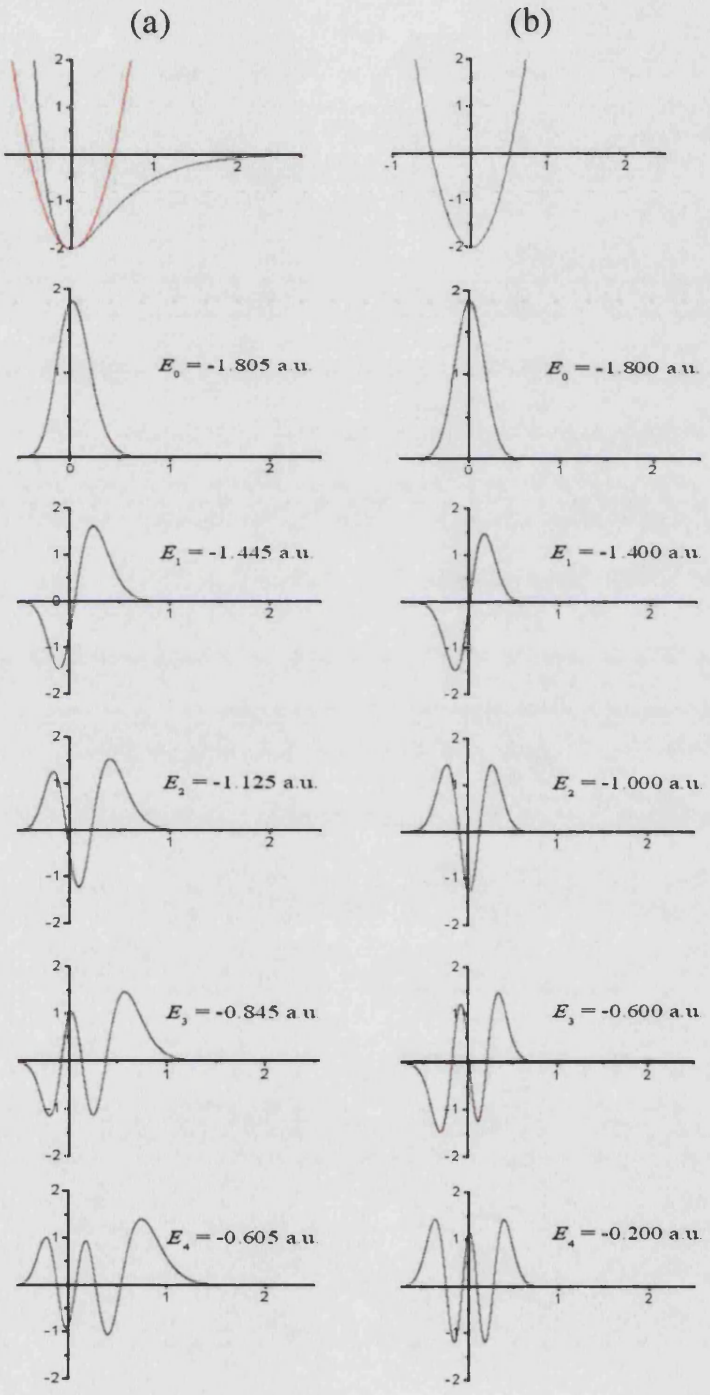

Figure 4.1: The five lowest energy levels of (a) the Morse and (b) the harmonic potential. Here the wavefunction is plotted as a function of position.

System	ε_{HF} (a.u.)	ZPE_{HF}	System	ε_{HF} (a.u.)	ZPE_{HF}
C_2HMu	-0.90508	1.473	CH_3MuN	-0.91695	1.493
C_2H_2	-0.98220	0.562	CH_4N	-0.99543	0.570
C_2HD	-0.99360	0.342	CH_3DN	-1.00696	0.344
C_2H_2Mu	-0.97335	1.519	CH_4MuN	-0.93767	1.509
C_2H_3	-1.05255	0.572	CH_5N	-1.01696	0.574
C_2H_2D	-1.06410	0.345	CH_4DN	-1.02854	0.345
C_2H_3Mu	-0.97934	1.532	MuO	-0.82171	1.461
C_2H_4	-1.05917	0.575	HO	-0.89938	0.569
C_2H_3D	-1.07077	0.346	DO	-0.91090	0.344
C_2H_4Mu	-0.99205	1.522	HMuO	-0.85507	1.454
C_2H_5	-1.07132	0.572	H_2O	-0.93234	0.566
C_2H_4D	-1.08288	0.345	HDO	-0.94381	0.343
H_2MuN	-0.93188	1.497	$CHMuO_2$	-0.79236	1.411
H_3N	-1.01060	0.571	CH_2O_2	-0.86759	0.556
H_2DN	-1.02214	0.345	$CHDO_2$	-0.87892	0.340
CH_2MuN	-0.90702	1.518	CH_3MuO	-0.86346	1.462
CH_3N	-0.98678	0.576	CH_4O	-0.94106	0.568
CH_2DN	-0.99840	0.346	CH_3DO	-0.95256	0.344

Table 4.1: Hartree-Fock eigenvalues and zero-point energies for the hydrogen-like nuclei in the parametrisation reference systems. Quoted energies are in eV

the energy and wavefunction of the HLN, from which various properties can be found, including the zero-point energy and extension in bond length. The HLN basis set used for these calculations (and for all other calculations in this thesis) were two sets of spherically-symmetric Gaussians, centred on two positions along the bond (see Section 4.4), with exponents {25.0, 10.0, 4.0, 1.2, 0.4}, found to give energies converged to 0.01 eV. The results of these Hartree-Fock calculations can be seen in Table 4.1. As will be shown in Section 4.4, the Hartree-Fock HLN wavefunction exhibits the overlocalisation observed in the analytical calculations of Section 3.4.4.

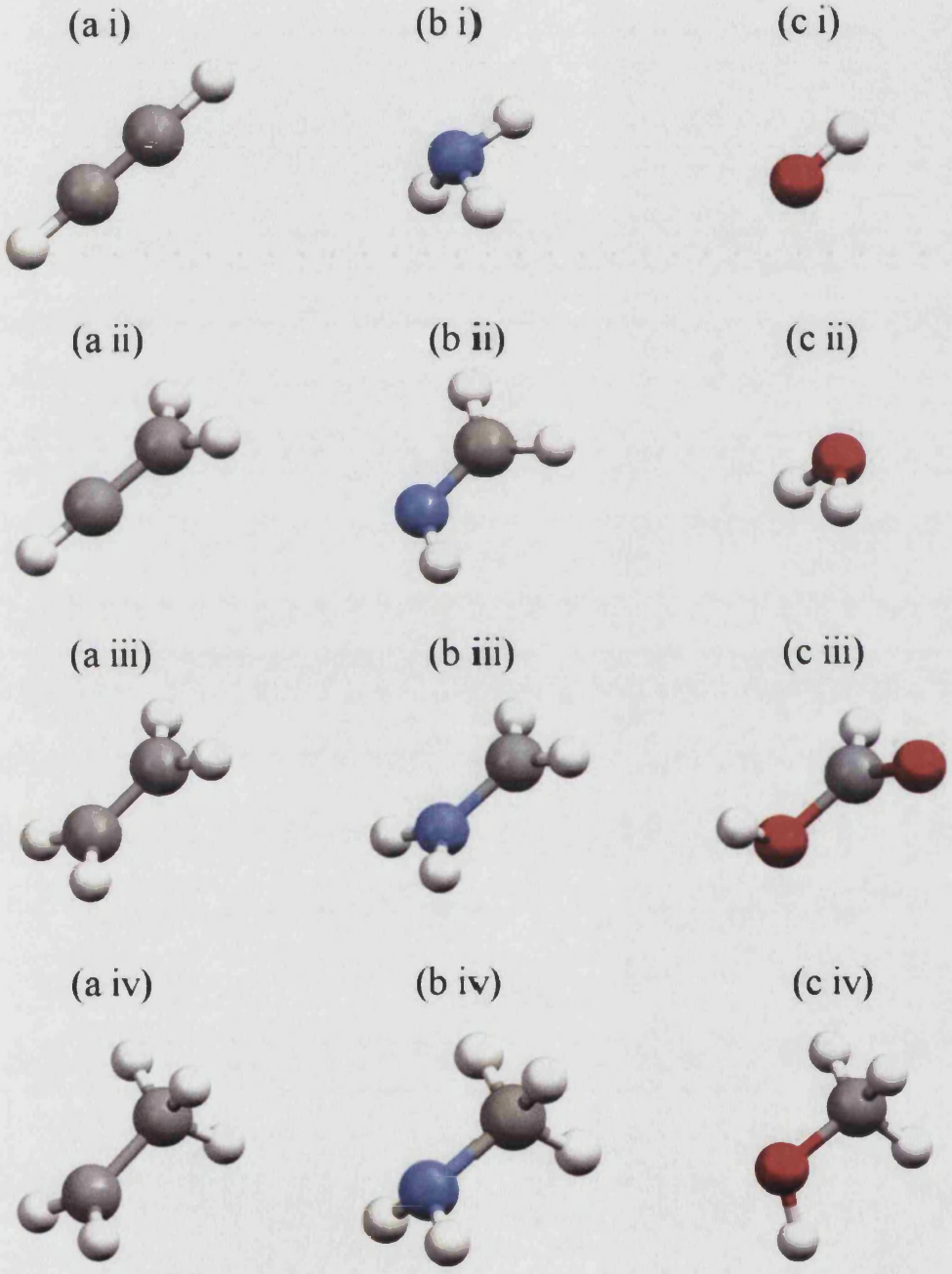

Figure 4.2: Reference systems for the parametrisation of the correlation model. a i-iv) C-X bond, b i-iv) N-X bond, c i-iv) O-X bond

4.3 The Model

The problem at hand is one of evaluating the correlation energy between the hydrogen-like nucleus and the electron density. The correlation energy is defined as the difference between the Hartree-Fock energy and the true ground state energy. Since the Hartree-Fock energy is a variational approximation to the true ground state energy, it becomes obvious that the correlation energy will be negative. In the case of electron-electron correlation this energy represents the instantaneous electrostatic repulsion experienced by the electrons which is ignored in Hartree-Fock theory, a mean field approximation. The correlation energy between the hydrogen-like nucleus and the electron density, however, represents the degree to which the nuclei's trapped electron density follows the motion of the heavier, slower HLN. We can use this fact to obtain an upper and lower bound on the correlation energy. In the Hartree-Fock approximation, the HLN and the electron density are assumed to be completely uncorrelated, and so the energy associated with their interaction is an averaged one. In contrast, the Born-Oppenheimer approximation assumes the heavier particle (in this case the HLN) to be static, and so therefore the motion of the electron density is fully correlated to it. The true correlated interaction energy *must* therefore lie between these two values, which will be referred to as $V^{(HF)}$ and $V^{(BO)}$. Figure 4.3 shows how the Hartree-Fock (calculated using Equation 2.8) and Born-Oppenheimer (calculated using Equation 2.14) potential energies vary as a function of particle separation for a fixed particle mass ratio (in this case the muon-electron mass ratio). The HF curve was generated by assuming that the muon could be described by a Gaussian, chosen so that the zero-point energy of the muon was equal to 0.5 eV. The BO curve was generated by assuming the muon to be point-like.

In both cases a Gaussian was also used to describe the electron wavefunction, chosen such that the electron zero-point energy was equal to $0.5\sqrt{m_\mu/m_e} \simeq 7.2$ eV . As can be seen, the difference between the two potentials rapidly drops to zero, implying that the effects of correlation are only important for the electron density in close proximity (~1 Å) to the hydrogen-like nucleus. In terms of electronic basis functions, this means that correlation effects would only appear to be important for matrix elements where the associated electron density is at least partially centred at the HLN site. Since the effects of HLN-electron correlation

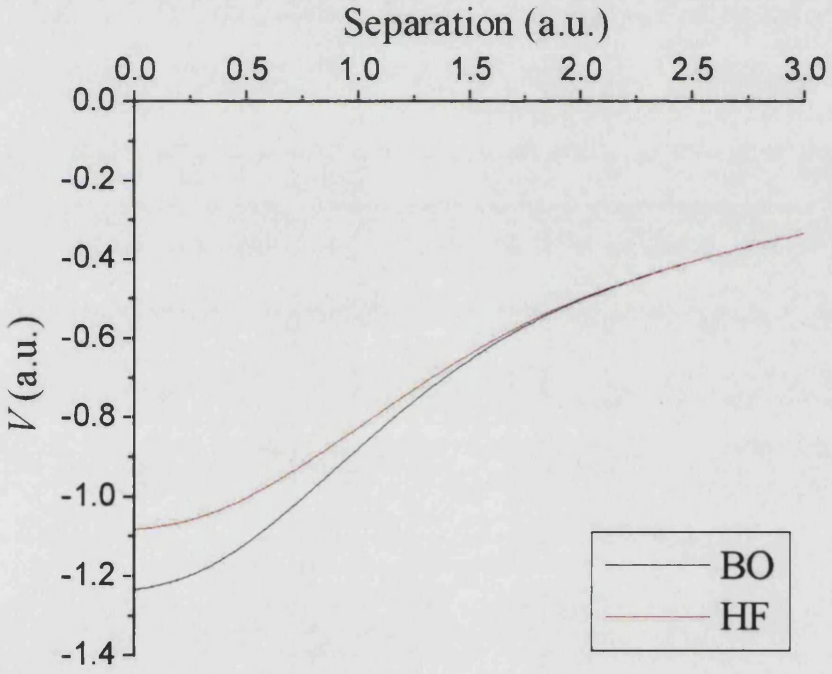

Figure 4.3: Variation of the Born-Oppenheimer and Hartree-Fock potential energies as a function of particle separation

are only important over a short range, the total potential energy experienced by the HLN in the Hartree-Fock approximation can be approximately separated into two components. One component, V_L, corresponds to the combined po-

tential energy contributions from the other nuclei in the system, and from the electron density at a distance such that correlation effects are unimportant (i.e. $|\mathbf{r}_\mu - \mathbf{r}_e| > 1$ Å). This contribution can be described by a function inversely proportional to some power of x, where x is the direction in which the HLN is bound to the system. The other contribution, V_S, corresponds to the potential energy experienced by the HLN due to the electron density for which $|\mathbf{r}_\mu - \mathbf{r}_e| < 1$Å. Since in the HF approximation this electron density is not free to follow the motion of HLN, this contribution is responsible for the overlocalisation of the HLN wavefunction, and, from the calculations of Section 4.2, can be well described by a function proportional to $(\mathbf{r} - \mathbf{r}_\mu)^{2n}$. The potential energy experienced by the HLN in the HF approximation can then be written

$$V^{(HF)} \simeq V_L + V_S.$$

In the HF approximation, the HLN Hamiltonian matrix elements take the form

$$H_{\lambda\sigma}^{(HF)} = \left\langle \varphi_\lambda^*(\mathbf{r}_\mu) \left| \frac{-\nabla_\mu^2}{2m_\mu} \right| \varphi_\sigma(\mathbf{r}_\mu) \right\rangle + V_{\lambda\sigma}^{(HF)}, \tag{4.2}$$

where

$$V_{\lambda\sigma}^{(HF)} = -\sum_{\nu\kappa}^{elec.} P_{\nu\kappa}^{(e)} \left(\varphi_\lambda^*(\mathbf{r}_\mu)\varphi_\sigma(\mathbf{r}_\mu) \left| \mathbf{r}_{e\mu}^{-1} \right| \varphi_\nu^*(\mathbf{r}_e)\varphi_\kappa(\mathbf{r}_e) \right), \tag{4.3}$$

and $\mathbf{r}_{e\mu} = |\mathbf{r}_e - \mathbf{r}_\mu|$. An analogous term in the BO approximation does not exist, since the HLN probability density, $\varphi_\lambda^*(\mathbf{r}_\mu)\varphi_\sigma(\mathbf{r}_\mu)$, is represented by a Dirac delta function, $\delta(\mathbf{r}_\mu)$, and so doesn't have any degree of delocalisation. However, if the HLN density is described by functions with well defined maxima at their centre, such as spherically symmetric Gaussians, then an approximate Born-Oppenheimer potential $V^{(BO)}$, can be defined;

$$V_{\lambda\sigma}^{(BO)} = -\sum_{\nu\kappa}^{elec.} P_{\nu\kappa}^{(e)} S_{\lambda\sigma} \left(\varphi_\nu^*(\mathbf{r}_e) \left| \mathbf{r}_{e\mu}^{-1} \right| \varphi_\kappa(\mathbf{r}_e) \right), \tag{4.4}$$

where $S_{\lambda\sigma}$ is an overlap matrix element,and here $\mathbf{r}_\mu$ corresponds to the site on which the HLN basis functions are centred, and not a variable of integration. An important point here is that Equation 4.4 is also the long distance limiting behaviour of $V_{\lambda\sigma}^{(HF)}$, i.e.

$$\lim_{\mathbf{r}_{e\mu}\to\infty} V_{\lambda\sigma}^{(HF)} = V_{\lambda\sigma}^{(BO)}. \tag{4.5}$$

Before going any further, an important point must be made. Since functions with well defined maxima at their centre are required for the approximation of Equation 4.4 to be valid, and the intention here is to build a model potential using this approximation, the types of basis functions that can be used are restricted to those with zero angular momentum. To model asymmetry in the potential then requires more than one basis centre to be placed on the potential energy surface along the direction of the asymmetry. However, severe numerical problems are caused by the large non-diagonal overlap matrix elements present when multiple centres are placed in close proximity to each other. These problems do not manifest themselves when only two centres are placed in close proximity, and so this approach essentially restricts the HLN basis set to be distributed over no more than two sites per potential well. It is also worth noting that off-diagonal matrix elements involving basis functions on different centres can still be described using the approximation of Equation 4.4 since the Gaussian product theorem (cf. Section 2.3.1) ensures that a Gaussian function localised between these two centres can be defined.

We can now consider the model potential that can be constructed from a linear combination of $V^{(BO)}$ and $V^{(HF)}$, i.e.

$$V_C = \alpha V^{(BO)} + \beta V^{(HF)}, \tag{4.6}$$

and the effect such a model potential would have on the HLN wavefunction. In

the limit $\alpha = 0$, $\beta = 1$, V_C reduces to $V^{(HF)}$, whilst in the opposite case ($\alpha = 1$, $\beta = 0$), the potential energy becomes proportional to the overlap matrix, giving

$$\begin{aligned} \varepsilon \cdot \mathbf{S} \cdot \mathbf{C} &= \mathbf{H} \cdot \mathbf{C} \\ &= (\mathbf{K} + \mathbf{V}) \cdot \mathbf{C} \\ &= (\mathbf{K} + \eta \mathbf{S}) \cdot \mathbf{C} \end{aligned}$$

$$\therefore \mathbf{K} \cdot \mathbf{C} = (\varepsilon + \eta) \cdot \mathbf{S} \cdot \mathbf{C} \tag{4.7}$$

The ground state of the HLN in a system described by such a model potential would be obtained by either adopting the most diffuse form allowed by the basis set, or by attempting to assume a plane wave solution. Neither of these cases is a good representation of the true potential, expected to be approximately Morse-like along the bond, and harmonic, yet significantly less confining than the HF potential, normal to the bond. A more useful form for the model potential would be

$$V_C = f_c V^{(BO)} + (1 - f_c) V^{(HF)}, \tag{4.8}$$

where f_c can be varied. It can be seen quite clearly that the effect of increasing f_c would be to effectively reduce the curvature of the potential energy surface normal to the bond, since $V^{(BO)}$ is only weakly dependent on the degree of localisation of the HLN density associated with a given matrix element. This is the effect that would be expected if HLN-electron correlation effects were included. The effect that increasing f_c would have on the potential energy along the bond, however, is less clear. It would appear upon first inspection that V_C would be a poor approximation to a Morse potential, but, as will be shown, only a small region of the Morse potential need be well described in order to obtain an accurate component of the HLN wavefunction along the bond. Figure 4.4 shows

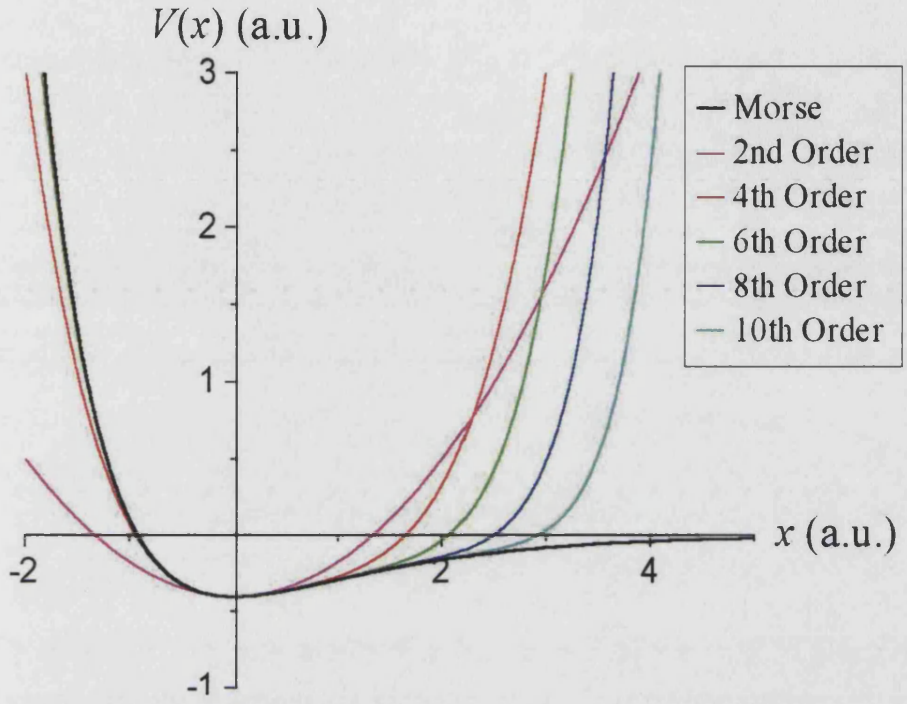

Figure 4.4: The Morse potential, and series expansions

successively higher order series-expansions of the Morse potential. Although the 'tail' of the function is very badly described by even a 10th order expansion, around the minimum the function is well described by only a 4th or 6th order expansion. The general form of the Morse potential is given by

$$V_M(x) = D_e \left(1 - \exp\left[-\beta x\right]\right)^2 - D_e, \tag{4.9}$$

and values of $D_e = 0.4$ a.u., $\beta = 0.75$ a.u. describe a function for which the solution to the one dimensional Schrödinger equation for a particle of muon mass yields a zero-point energy of 0.308 eV, and a bond length increase of 0.031 Å, comparable to values found numerically in the subsequent sections. Table 4.2 gives the corresponding values for series expansions of the Morse potential, along with those obtained from a numerical interpolation of the function over the

Function	ZPE (eV)	Δx (Å)
Morse	0.308	0.031
2nd Order	0.317	0.000
4th Order	0.311	0.030
6th Order	0.308	0.031
Interpolation	0.308	0.031

Table 4.2: Zero-point energies and bond length increases for the muon in various approximations to the Morse potential

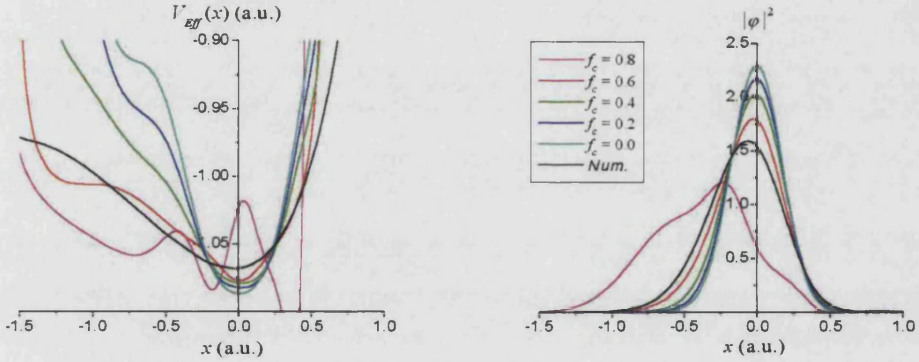

Figure 4.5: V_{Eff} and $|\varphi_0|^2$, obtained for various values of f_c, for the muon in C_2H_4Mu. Numerical reference calculations are shown in bold black.

range $-1.5 \leq x \leq 1.0$ a.u. The results presented in Table 4.2 suggest that if the PES can be modelled well over the range $-1.5 \leq x \leq 1.0$ (where the minimum of the energy is at $x = 0$), then accurate wavefunctions can be calculated. For the model potential of Equation 4.8, the effective potential experienced by the HLN can be obtained after a SCF calculation has been performed by evaluating

$$V_{Eff.} = \frac{(E_0 - K)\varphi_0}{\varphi_0}, \tag{4.10}$$

where φ_0 is the ground state HLN wavefunction obtained from the SCF calculation, and E_0 is the corresponding eigenvalue. Figures 4.5 and 4.6 show V_{Eff} and $|\varphi_0|^2$ for various values of f_c, obtained for the muon in the system C_2H_4Mu.

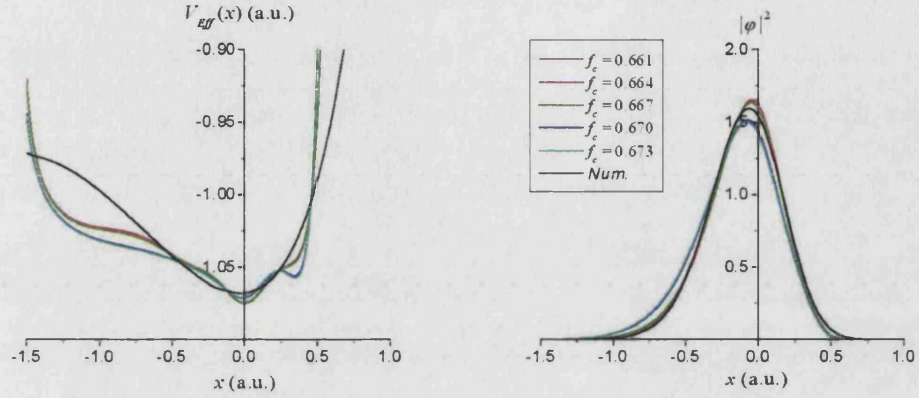

Figure 4.6: As Figure 4.5, over a more accurate range of f_c.

f_c	ZPE (eV)	Δx (Å)	f_c	ZPE (eV)	Δx (Å)
0.800	0.327	0.195	0.661	0.517	0.054
0.600	0.672	0.035	0.664	0.509	0.055
0.400	1.041	0.014	0.667	0.501	0.057
0.200	1.307	0.007	0.670	0.491	0.063
0.000	1.524	0.004	0.673	0.478	0.071
Numerical	0.497	0.051	Numerical	0.497	0.051

Table 4.3: zero-point energies and bond length increases for the muon in C_2H_4Mu

More details of this calculation are given in Section 4.4.2. As can be seen, for the case $f_c = 0$, corresponding to HF-approximation, the curvature of the PES is far too pronounced, and the corresponding probability density is over-localised. In contrast, the model seems to break down by the time f_c is reduced to 0.4. For values of $f_c \sim 0.667$, good agreement is obtained for both V_{Eff} over the required range and $|\varphi_0|^2$. Table 4.3 shows the zero-point energies and bond length increases corresponding to the results presented in Figures 4.5 and 4.6. Again, good agreement with the numerical reference calculations is obtained using $f_c \sim 0.667$. This suggests that the model potential of Equation 4.8 is a good candidate to model the correlated interaction between the HLN and the electron

density in a given system. Using this model potential, the HLN Hamiltonian matrix elements are given by

$$H_{\lambda\sigma} = \left\langle \varphi^*_\lambda(\mathbf{r}_\mu) \left| \frac{-\nabla^2_\mu}{2m_\mu} \right| \varphi_\sigma(\mathbf{r}_\mu) \right\rangle + f_c V^{(BO)} + (1 - f_c) V^{(HF)}. \tag{4.11}$$

f_c can be considered to be a 'correlation factor', which controls the degree to which the Hartree-Fock and Born-Oppenheimer potentials are mixed. In effect, f_c controls the degree to which the motion of the electron density is correlated to that of the hydrogen-like nucleus, with, as previously stated, $f_c = 0$ corresponding to the Hartree-Fock approximation with no correlation, and $f_c = 1$ corresponding to the Born-Oppenheimer approximation, with complete correlation. This factor would be expected to be dependent on the mass of the nucleus, since the vibrational motion of a more massive particle will have a smaller amplitude, and so will appear more point-like to the electron density. It would also be expected to be dependent on the chemical environment experienced by the hydrogen-like nucleus, although it is not obvious that a direct physical property of the system could be used to define this dependency. A set of reference systems were therefore used in an attempt to parametrise this model.

Throughout this section, it has been assumed that the effects of HLN-electron correlation do not alter the electron density. Although this sounds rather drastic, it has been shown [104], that the effect of HLN-electron correlation on the electron density when considering interstitial defects is crystalline silicon is indeed very small. Furthermore, the results presented in Section 3.4.4 show that when the HLN is coupled harmonically to the electron the difference between the electronic components of the Hartree-Fock and exact wavefunction is negligible. This suggests that the approximation made here is valid.

4.4 Parametrisation of the Model; Test Systems

There is a large body of experimental data for molecular systems containing Mu, H, and D, and much work, both experimental and theoretical, has been completed on the behaviour of these hydrogen-like nuclei in small organic molecules. In many of these systems, the HLN interacts with the system through C-X, N-X, and O-X bonds, where X={Mu, H, D}. The parametrisation of the model presented here focuses on the quantum-mechanical features of these bonds. Successful parametrisation of systems containing these bonds would illustrate the behavior of the correlation factor, f_c, with respect to nuclear mass and bond type, and would potentially allow predictive use of the model in both larger systems containing these bonds, and other systems such as crystalline systems containing defect complexes.

4.4.1 Reference Calculations

The parametrised model was implemented in Gaussian 98 [45], and calculations were made in a similar manner to that described in Section 4.2 but incorporating the new model potential in place of the Hartree-Fock one. The same software was employed to make the reference calculations. These reference calculations were made by first assuming that the vibrational motion of the HLN could be decoupled into a motion along the bond, and two orthogonal motions normal to the bond. The potential energy surface on which the HLN moves could then be described as $V(x,y,z) = V_x(x) + V_y(y) + V_z(z)$. These one dimensional potential energy surfaces were then sampled by evaluating the total electronic energy of a given system as the position of the HLN (assumed here to be point-like) was moved from its equilibrium geometry in one of the orthogonal directions. These calculations were used to construct three one-dimensional

potential energy surfaces consisting of approximately 50 points each for which the HLN Schrödinger equation could be numerically solved, using the 'shooting method'. In this method, the HLN wavefunction is assumed to be zero with an arbitrary first derivative at a point far from the potential energy minimum, and its corresponding energy is varied iteratively until a converged solution is achieved. This occurs when the wavefunction has the expected physical properties, i.e. the wavefunction and its first derivative are continuous, the function vanishes at large distances from the minimum, i.e.

$$\lim_{i \to \pm\infty} \varphi(i) = 0, \tag{4.12}$$

and further variation in the energy results in no significant variation in the wavefunction. The numerical wavefunction can then be used to calculate physical properties of the HLN, which can in turn be used for the parametrisation of the model. The properties chosen for the parametrisation were the zero-point energy of the nucleus both along (ZPE_x) and across ($ZPE_{y,z}$) a given bond, and the isotope dependent variation of the bond length, $\Delta x = \langle \varphi \, | \widehat{x} | \, \varphi \rangle$.

4.4.2 The C-X Bond

The reference systems chosen for the parametrisation of the C-X bond were C_2HX, C_2H_2X, C_2H_3X, and C_2H_4X, isotopomers of acetylene, the vinyl radical, ethylene, and the ethyl radical respectively. The results of the reference calculations can be seen in Table 4.4.

The model was parametrised by attempting to obtain as close agreement as possible with the reference calculations through the variation of f_c, whilst keeping the HLN basis set unchanged. One of the basis centres used in the calculations was located at the classical equilibrium position of the HLN, and the other at a

System	ZPE_x	ZPE_y	ZPE_z	$ZPE_{Tot.}$	Δx (Å)
C_2HMu	0.312	0.088	0.090	0.490	0.043
C_2H_2	0.10	0.026	0.026	0.152	0.016
C_2HD	0.073	0.017	0.017	0.107	0.011
C_2H_2Mu	0.271	0.120	0.082	0.473	0.050
C_2H_3	0.097	0.040	0.023	0.160	0.015
C_2H_2D	0.069	0.028	0.015	0.112	0.010
C_2H_3Mu	0.288	0.128	0.110	0.526	0.046
C_2H_4	0.097	0.040	0.030	0.167	0.016
C_2H_3D	0.068	0.028	0.021	0.117	0.013
C_2H_4Mu	0.269	0.110	0.118	0.497	0.051
C_2H_5	0.093	0.038	0.040	0.171	0.017
C_2H_4D	0.066	0.027	0.028	0.121	0.012

Table 4.4: Results of the C-X bond reference calculations. Quoted energies are in eV

distance of ~0.3 Å from the first, in the direction of the bond. The sensitivity of the zero-point energy and Δx to this separation was found to be very small about this value. Table 4.5 shows the variation in the correlation factor, as well as the optimised zero-point energies and increases in bond length, for the twelve systems. Although the calculated zero-point energies are in good agreement with the reference calculations, Δx is underestimated for the heavier nuclei. These parameters for f_c, however, ensure a larger overlap with the wavefunctions of the reference calculations, and attempts to obtain better agreement in the variation of the bond length results in an over-emphasised tail in the wavefunction. It is possible that this underestimation of Δx is associated with the use of the variational method, which gives more reliable energies than wavefunctions.

It was shown in Section 3.4.4 that, over the HLN mass range considered here, the correlation energy was found to be directly proportional to $m^{-1/2}$, and so the behaviour of the correlation factor as a function of nuclear mass

System	f_c	$ZPE_{Tot.}$ (eV)	Δx (Å)
C_2HMu	0.670	0.493	0.053
C_2H_2	0.770	0.157	0.010
C_2HD	0.794	0.101	0.009
C_2H_2Mu	0.675	0.468	0.058
C_2H_3	0.757	0.163	0.010
C_2H_2D	0.778	0.116	0.008
C_2H_3Mu	0.655	0.524	0.048
C_2H_4	0.757	0.166	0.010
C_2H_3D	0.778	0.120	0.007
C_2H_4Mu	0.667	0.501	0.052
C_2H_5	0.758	0.174	0.009
C_2H_4D	0.781	0.123	0.007

Table 4.5: Optimal values of f_c, along with the corresponding zero-point energies and increases in bond length for the C-X bond reference systems

was investigated. Figure 4.7 illustrates this behaviour, and suggests that the correlation factor could be fitted to a function of the form

$$f_c^C(m) = k_c - \frac{g_c}{m^{\frac{1}{4}}}, \tag{4.13}$$

with the values of $k_c = 0.888$, $g_c = 0.850$. This gives for the correlation factors for the three nuclear masses in a C-X bond;

$$\begin{aligned} f_{c\mu}^C &= 0.663 \\ f_{cp}^C &= 0.758 \\ f_{cd}^C &= 0.779 \end{aligned}$$

These factors can now be reapplied to the reference systems to compare with the reference calculations. The correlation energy term can also be calculated as the difference between the eigenvalues calculated in the parametrised correlation model and those calculated within the Hartree-Fock framework. The results of these calculations can be seen in Table 4.6.

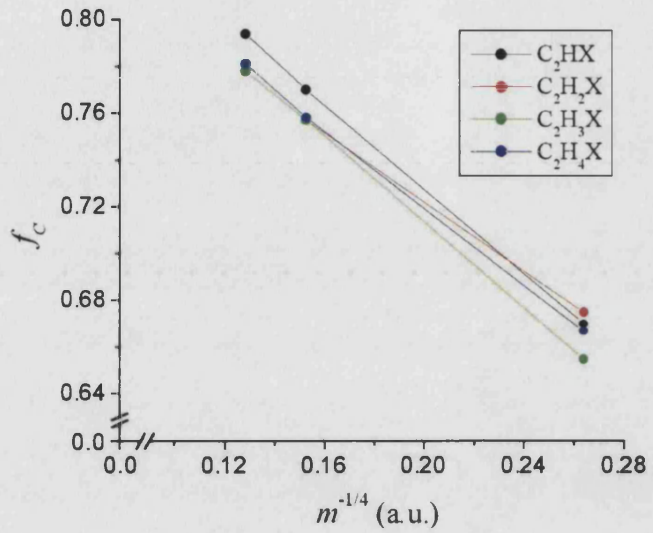

Figure 4.7: Dependence of f_c on nuclear mass in the C-X bond reference systems

If the zero-point energies calculated using the parametrised model are compared with those at the Hartree-Fock level (see Table 4.1), then a reduction to approximately one third of the HF values is again observed, as seen in Section 3.4.4. Figure 4.8 shows the dependence of the correlation energy upon nuclear mass. In contrast to the calculations of Section 3.4.4, the correlation energy is seen here to be proportional to $m^{-1/2}$. These results suggest that, although the effect of the correlation on the HLN wavefunction is largely independent of the nature of the interaction between the nucleus and the electron density (i.e. harmonic and Coulombic interactions show the same general features), the correlation energy itself *is* sensitive to the nature of the interaction.

Finally, examples of the wavefunctions calculated using the parametrised model for the C-X bond are presented. The probability densities shown in Figure 4.9 are those calculated for a hydrogen-like nucleus in the isotopomers of the ethyl radical. The agreement along the bond (i.e. the x-component) is excellent, but

System	ZPE_C (eV)	$\frac{ZPE_C}{ZPE_N}$	Δx_C (Å)	$\Delta x_C/\Delta x_N$	E_C (eV)
C_2HMu	0.510	1.041	0.050	1.163	-1.699
C_2H_2	0.204	1.342	0.005	0.312	-0.592
C_2HD	0.181	1.692	0.002	0.182	-0.447
C_2H_2Mu	0.498	1.060	0.052	1.040	-1.797
C_2H_3	0.157	0.981	0.010	0.667	-0.649
C_2H_2D	0.103	0.920	0.009	0.900	-0.518
C_2H_3Mu	0.503	0.967	0.052	1.130	-1.807
C_2H_4	0.161	0.964	0.010	0.625	-0.651
C_2H_3D	0.106	0.906	0.009	0.692	-0.522
C_2H_4Mu	0.511	1.022	0.050	0.980	-1.784
C_2H_5	0.175	1.023	0.008	0.471	-0.641
C_2H_4D	0.142	1.174	0.005	0.417	-0.497

Table 4.6: Zero-point energies, increases in bond lengths and correlation energies as calculated using the parametrised correlation model for the C-X bond

the localisation across the bond is still overestimated. the reasons for this are twofold. Firstly, as was shown in Section 3.2, the higher energy components would be expected to be better approximated using the variational method, and secondly, the two basis centres along the bond used in the parametrised model give a much higher degree of flexibility in the basis set along the bond.

If the components of the probability density across the bond are approximated by Gaussians, then the exponent is approximately 25% too large for the muon, 33% too large for the proton, and 40% too large for the deuteron. This corresponds to the same magnitude increases in the vibrational frequency ω of the particles, and since for the harmonic oscillator the zero-point energy increases linearly with ω, so the energies are overestimated by the same amount. The zero-point energy across the bond accounts for approximately 35% of the total zero point energy, and so the overlocalisation across the bond would be expected to introduce an error in the energy of between $\sim$10% for the muon and

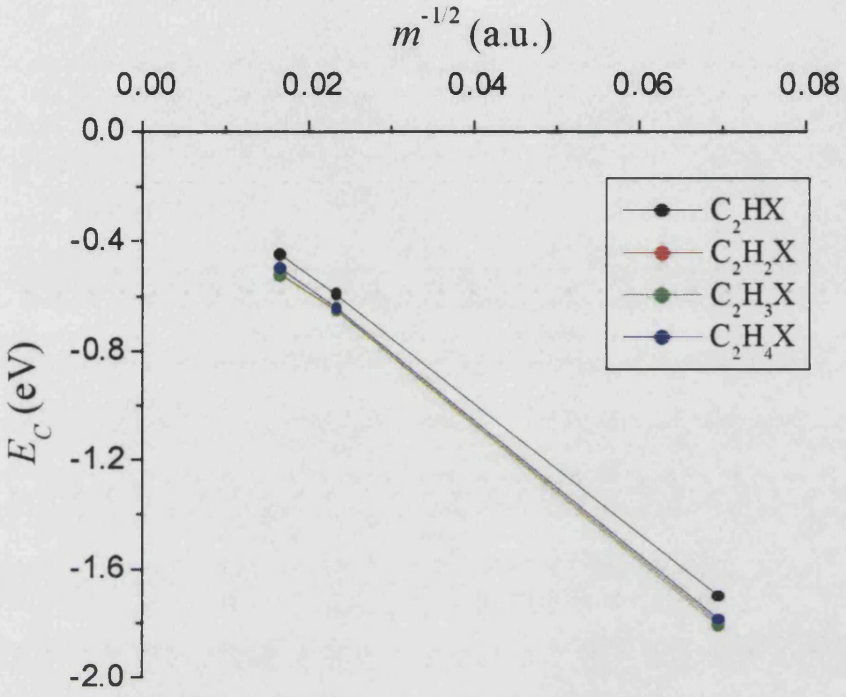

Figure 4.8: Variation of the correlation energy, E_C, with nuclear mass for the parametrised C-X bond

~15% for the deuteron.

4.4.3 The N-X Bond

For the parametrisation of the N-X bond, the same computational methods were applied as in Section 4.4.2. The reference systems used in the parametrisation were H_2XN, CH_2XN, CH_3XN, CH_4XN, isotopomers of ammonia, methanimine, the amino-methyl radical, and methylamine. Results of the numerical reference calculations are shown in Table 4.7.

The zero-point energies for the hydrogen-like nucleus in the N-X bond reference systems are approximately 10% larger than those in the C-X bond reference systems, and there is a corresponding reduction in Δx, which in combination sug-

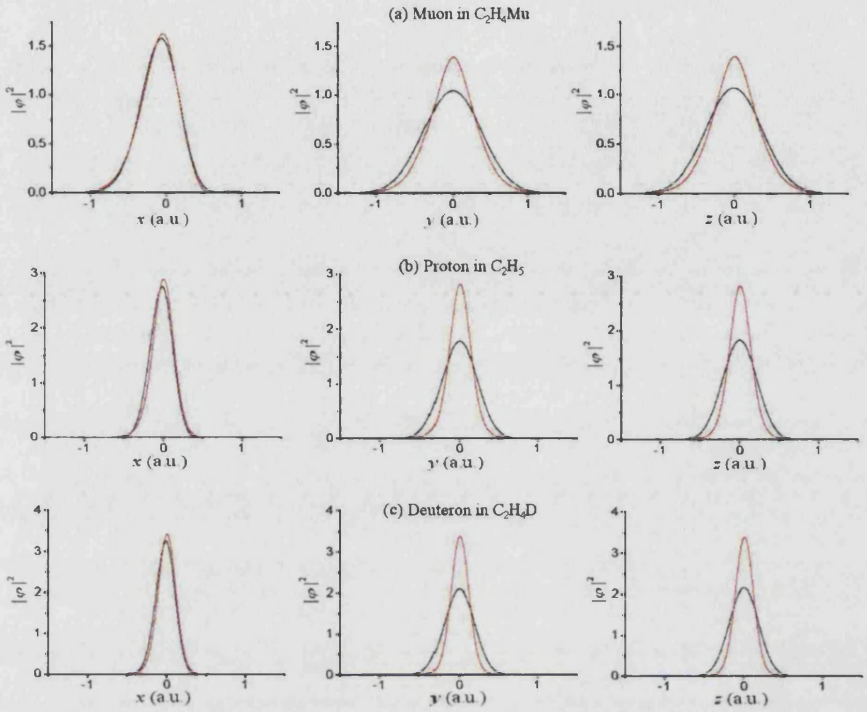

Figure 4.9: Probability densities along (x) and normal to (y, z) the bond for a) a muon in C_2H_4Mu, b) a proton in C_2H_5, and c) a deuteron in C_2H_4D. Numerical calculations in black, parametrised model calculations in red.

gest a greater degree of localisation of the nuclear wavefunction. As before f_c was varied to find the optimal values for the zero-point energy and Δx for each of the test system. Table 4.8 summarises these calculations.

Figure 4.10 shows the variation of f_c with nuclear mass. Again the $m^{-1/4}$ dependence of f_c is clearly evident, and allows for a fit of the form given by Equation 4.13. The fitted correlation factors for the N-X bond are

$$\begin{aligned} f_{c\mu}^N &= 0.627 \\ f_{cp}^N &= 0.745 \\ f_{cd}^N &= 0.771, \end{aligned}$$

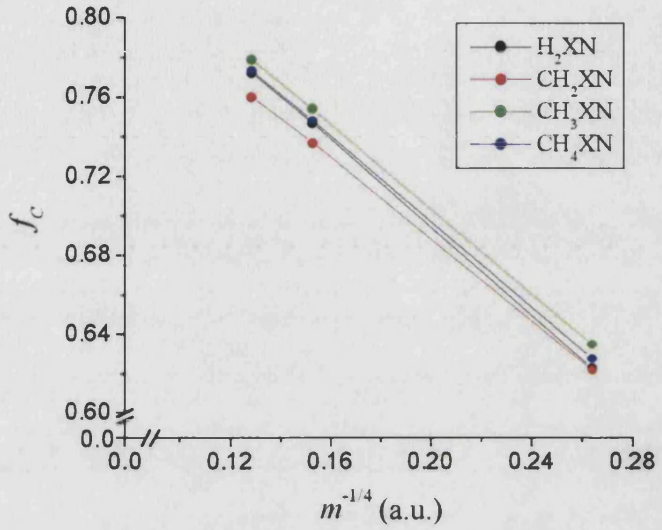

Figure 4.10: Dependence of f_c on nuclear mass for the N-X bond reference systems

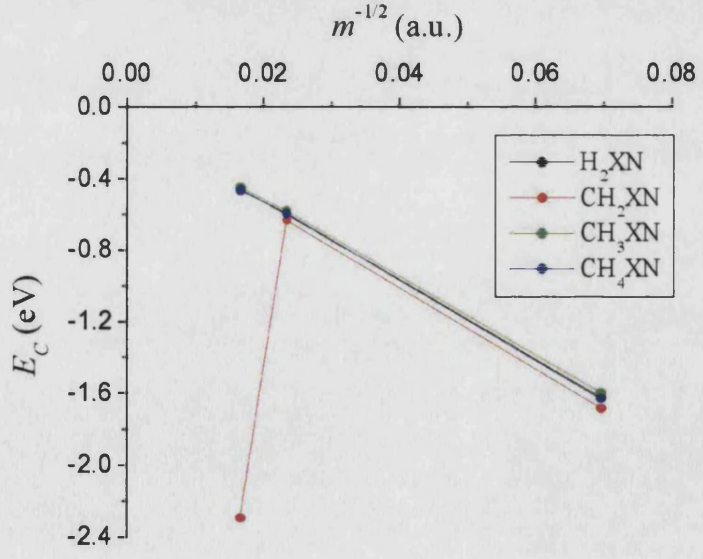

Figure 4.11: Variation of correlation energy, E_C, with nuclear mass for the parametrised N-X bond

System	ZPE_x	ZPE_y	ZPE_z	$ZPE_{Tot.}$	Δx (Å)
H_2MuN	0.340	0.129	0.091	0.560	0.042
H_3N	0.117	0.043	0.026	0.186	0.012
H_2DN	0.084	0.030	0.017	0.131	0.008
CH_2MuN	0.312	0.124	0.106	0.542	0.047
CH_3N	0.108	0.040	0.034	0.182	0.015
CH_2DN	0.077	0.028	0.025	0.130	0.010
CH_3MuN	0.321	0.142	0.079	0.542	0.045
CH_4N	0.112	0.046	0.021	0.179	0.015
CH_3DN	0.078	0.033	0.013	0.124	0.010
CH_4MuN	0.330	0.111	0.120	0.561	0.043
CH_5N	0.114	0.035	0.038	0.187	0.015
CH_4DN	0.081	0.024	0.027	0.132	0.010

Table 4.7: Results of the N-X bond reference calculations. Quoted energies are in eV

and Table 4.9 gives the bond length increases, in addition to the zero-point and correlation energies, for the HLN in the N-X bond reference systems calculated using the parametrised model with the parameters defined above. It can be seen for the first time, in the case of CH_2DN, that the parametrised model breaks down, predicting too small a zero-point energy, and too large a bond length increase. This breakdown becomes even more apparent in Figure 4.11 which shows the dependence of the correlation energy on the nuclear mass. For three of the four sets of test systems the $m^{-1/2}$ dependence of E_C is again clearly seen, and even for the remaining set CH_2XN, the dependence is clear for X={Mu, H}. The large discrepancy in the CH_2DN results suggests that the model may be very sensitive to the parametrisation when the HLN is of large mass. In principle, thresholding could be introduced within the code to compare the Hartree-Fock and parametrised model eigenvalues to alert the user to deviations from expected behaviour. Figure 4.12 shows the results of calculations made using the

System	f_c	$ZPE_{Tot.}$ (eV)	Δx (Å)
H_2MuN	0.623	0.559	0.043
H_3N	0.747	0.183	0.008
H_2DN	0.772	0.131	0.006
CH_2MuN	0.622	0.541	0.045
CH_3N	0.737	0.182	0.008
CH_2DN	0.760	0.134	0.006
CH_3MuN	0.635	0.541	0.045
CH_4N	0.754	0.180	0.008
CH_3DN	0.779	0.129	0.006
CH_4MuN	0.628	0.553	0.044
CH_5N	0.748	0.185	0.008
CH_4DN	0.773	0.130	0.006

Table 4.8: Optimal values for f_c, along with the corresponding zero-point energies and increases in bond length for the N-X bond reference systems

System	ZPE_C (eV)	$\frac{ZPE_C}{ZPE_N}$	Δx_C (Å)	$\Delta x_C/\Delta x_N$	E_C (eV)
H_2MuN	0.549	0.980	0.044	1.048	-1.622
H_3N	0.193	1.038	0.007	0.583	-0.593
H_2DN	0.141	1.076	0.005	0.625	-0.460
CH_2MuN	0.528	0.974	0.047	1.000	-1.683
CH_3N	0.131	0.720	0.015	1.000	-0.634
CH_2DN	0.033	0.254	0.058	5.800	-2.294
CH_3MuN	0.560	1.033	0.043	0.956	-1.595
CH_4N	0.215	1.201	0.005	0.333	-0.579
CH_3DN	0.179	1.443	0.002	0.200	-0.446
CH_4MuN	0.555	0.989	0.043	1.000	-1.630
CH_5N	0.198	1.059	0.006	0.400	-0.595
CH_4DN	0.149	1.129	0.004	0.400	-0.463

Table 4.9: Zero-point energies, increases in bond lengths and correlation energies as calculated using the parametrised correlation model for the N-X bond

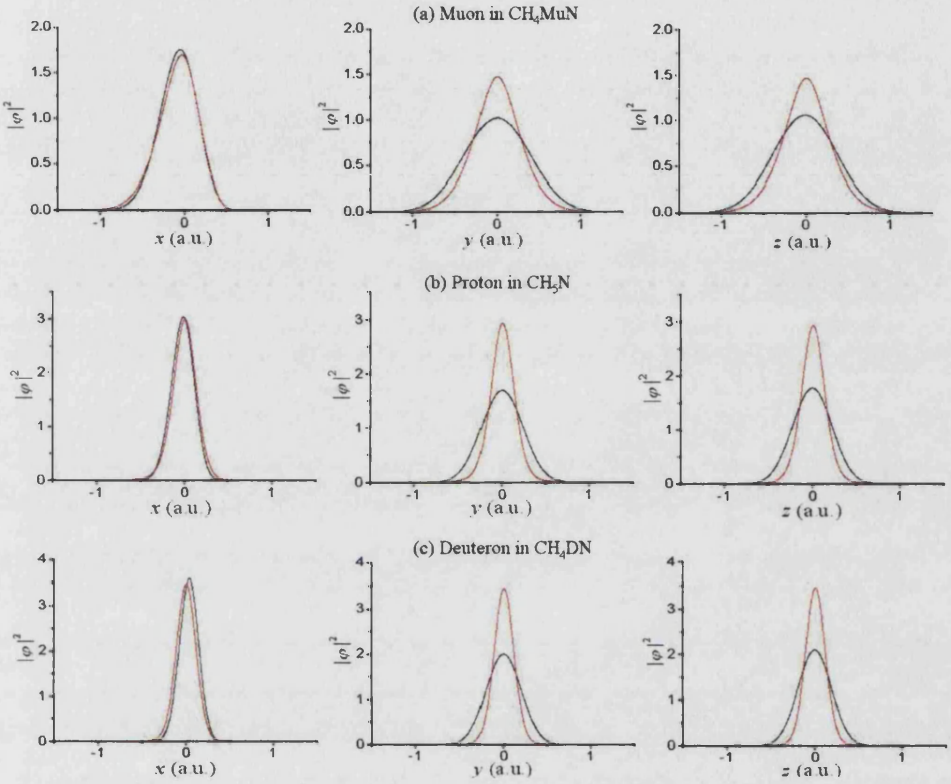

Figure 4.12: Probability densities along (x) and normal to (y, z) the bond for a) a muon in CH_4MuN, b) a proton in CH_5N, and c) a deuteron in CH_4DN. Numerical calculations in black, parametrised model calculations in red.

parametrised model for the HLN in the isotopomers of methylamine.

4.4.4 The O-X Bond

The reference systems used in the parametrisation of the O-X bond were XO, HXO, $CHXO_2$, and CH_3XO, isotopomers of the hydroxyl radical, water, formic acid, and methanol respectively. The results of the reference calculations can be seen in Table 4.10.

The differences in the zero-point energies between the isotopomers of the hydroxyl radical and those of water suggest that it may be difficult for a para-

System	ZPE_x	ZPE_y	ZPE_z	$ZPE_{Tot.}$	Δx (Å)
MuO	0.32	0.08	0.08	0.48	0.052
HO	0.113	0.020	0.020	0.153	0.016
DO	0.080	0.013	0.013	0.106	0.011
HMuO	0.39	0.14	0.09	0.62	0.046
H_2O	0.134	0.044	0.024	0.202	0.016
HDO	0.094	0.031	0.015	0.140	0.011
$CHMuO_2$	0.34	0.12	0.09	0.55	0.047
CH_2O_2	0.116	0.040	0.026	0.182	0.018
$CHDO_2$	0.082	0.028	0.017	0.127	0.013
CH_3MuO	0.347	0.129	0.080	0.556	0.045
CH_4O	0.120	0.042	0.020	0.181	0.014
CH_3DO	0.085	0.029	0.013	0.127	0.010

Table 4.10: Results o the O-X bond reference calculations Quoted energies are in eV

metrised model to correctly predict these zero-point energies although, as the test systems become larger, so the variation in the zero-point energies becomes smaller. The optimal values for f_c, along with the corresponding zero-point energies and increases in bond length, are presented in Table 4.11.

Figure 4.14 shows the variation of f_c with nuclear mass. Again the $m^{-1/4}$ dependence is seen, and so the $m^{-1/2}$ dependence in the correlation energy would be expected. The difference in the gradients of the curves in Figure 4.14 reflects the large difference in the zero-point energies, but nevertheless, correlation factors for the O-X bond can still be a calculated, and take the values

$$f_{c\mu}^{O} = 0.585$$

$$f_{c\mu}^{O} = 0.715$$

$$f_{c\mu}^{O} = 0.744.$$

Table 4.12 shows the zero-point energies, increases in bond length, and cor-

System	f_c	$ZPE_{Tot.}$ (eV)	Δx (Å)
MuO	0.605	0.482	0.053
HO	0.710	0.170	0.010
DO	0.735	0.108	0.009
HMuO	0.558	0.620	0.035
H_2O	0.714	0.204	0.007
HDO	0.744	0.138	0.006
$CHMuO_2$	0.575	0.563	0.042
CH_2O_2	0.719	0.185	0.008
$CHDO_2$	0.748	0.125	0.007
CH_3MuO	0.589	0.554	0.046
CH_4O	0.721	0.184	0.008
CH_3DO	0.747	0.131	0.006

Table 4.11: Optimal values for f_c, along with the corresponding zero-point energies and increases in bond length for the O-X bond reference systems

System	ZPE_C (eV)	$\frac{ZPE_C}{ZPE_N}$	Δx_C (Å)	$\Delta x_C/\Delta x_N$	E_C (eV)
MuO	0.532	1.108	0.046	0.885	-1.549
HO	0.139	0.908	0.013	0.813	-0.592
DO	0.037	0.349	0.044	4.000	-0.506
HMuO	0.556	0.897	0.043	0.935	-1.502
H_2O	0.200	0.990	0.007	0.438	-0.555
HDO	0.138	0.986	0.005	0.455	-0.436
$CHMuO_2$	0.540	0.982	0.044	0.936	-1.462
CH_2O_2	0.201	1.104	0.006	0.333	-0.537
$CHDO_2$	0.155	1.220	0.004	0.308	-0.414
CH_3MuO	0.564	1.014	0.042	0.933	-1.501
CH_4O	0.210	1.160	0.006	0.429	-0.554
CH_3DO	0.156	1.229	0.004	0.400	-0.433

Table 4.12: Zero-point energies, increases in bond lengths and correlation energies as calculated using the parametrised correlation model for the O-X bond

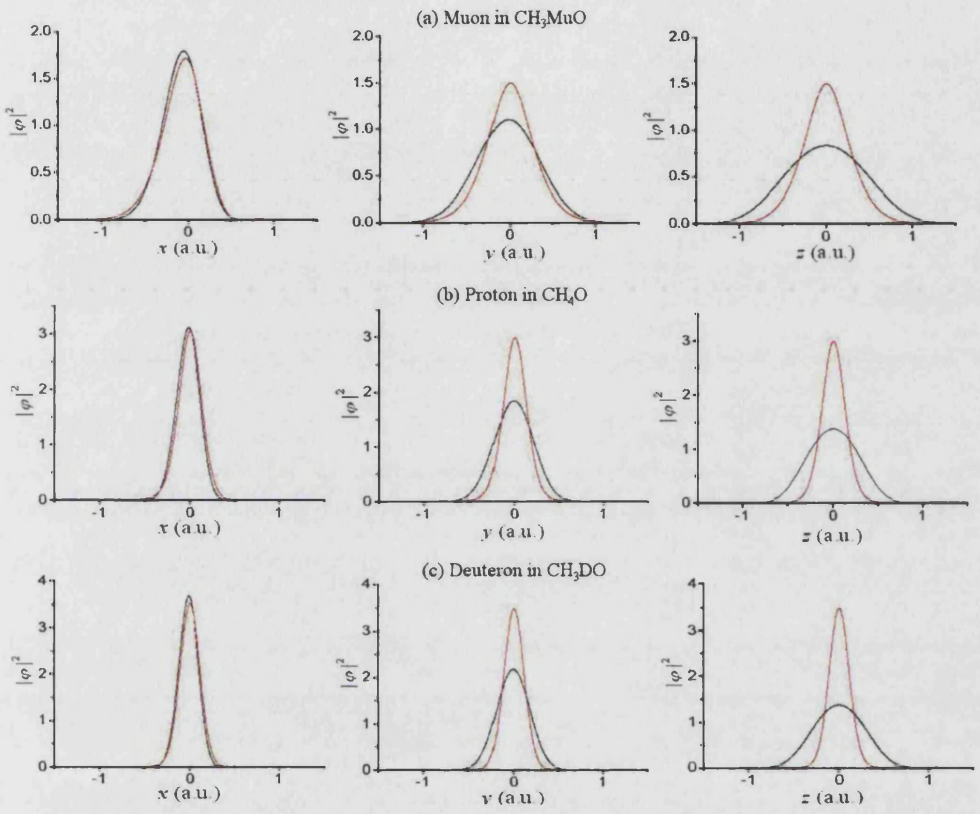

Figure 4.13: Probability densities along (x) and normal to (y, z) the bond for a) a muon in CH_3MuO, b) a proton in CH_4O, and c) a deuteron in C_2H_3DO. Numerical results in black, parametrised model results in red.

relation energies calculated using the parametrised model with the parameters defined above. Figure 4.15 shows the behaviour of the correlation energy with nuclear mass. Again, a deviation from the expected $m^{-1/2}$ behaviour is observed for DO. Comparison with Table 4.15 shows that the parametrised model also fails to accurately predict the zero-point energy for this system. This is further evidence that systems for which the parametrised model fails will be easily identifiable. Figure 4.13 shows the probabilities calculated for the HLN in the isotopomers of methanol using the parametrised correlation model.

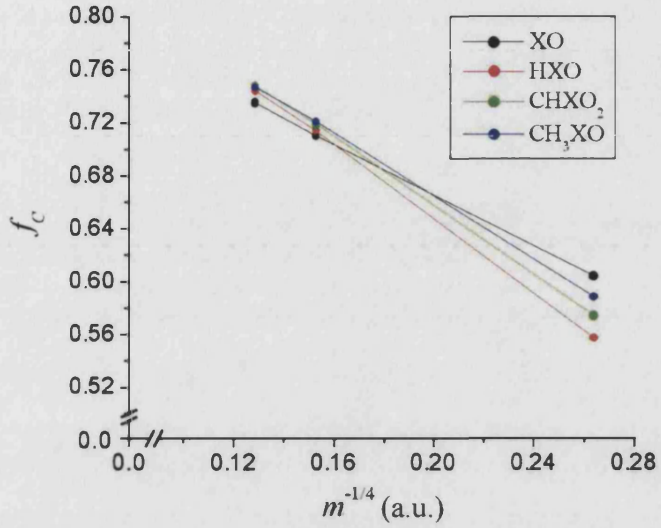

Figure 4.14: Dependence of f_c on nuclear mass for the O-X bond reference systems

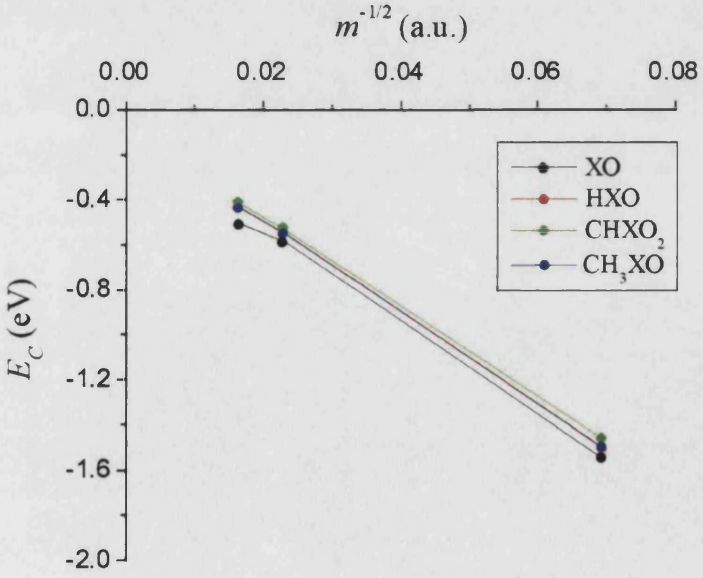

Figure 4.15: Variation of correlation energy, E_C, with nuclear mass for the parametrised O-X bond

Chapter 5

A Study of DNA Base Molecule Adducts

DNA has received much study during the 50 years since its double-helical structure was identified by James Watson and Francis Crick [134]. Of great importance was the discovery of the detrimental effects to health resulting from the attack of base molecules by free radicals, including atomic hydrogen [31, 56]. More recently, attention has turned to novel applications of the unique properties of DNA in areas as diverse as nanotechnology [139] and biocomputation [1]. These applications are possible due to the structure and self-replicating properties of DNA. DNA is formed of two helices hydrogen-bonded together via four base molecules; the pyrimidines, cytosine and thymine, and the purines, guanine and adenine. Figure 5.1 shows the *only* stable combinations of base molecule pairs, namely the cytosine-guanine (CG), and the adenine-thymine (AT) pair. The fact that these are the only base pairs formed in nature means that for a given single strand of DNA, there is only one matching complimentary strand, and herein lies the basic mechanism of self-replication. The bond energy in each base pair is $\sim k_B T$ and, although a chain of $\sim 20 - 30$ base pairs is stable at physiological temperatures, the work that must be done to separate the two

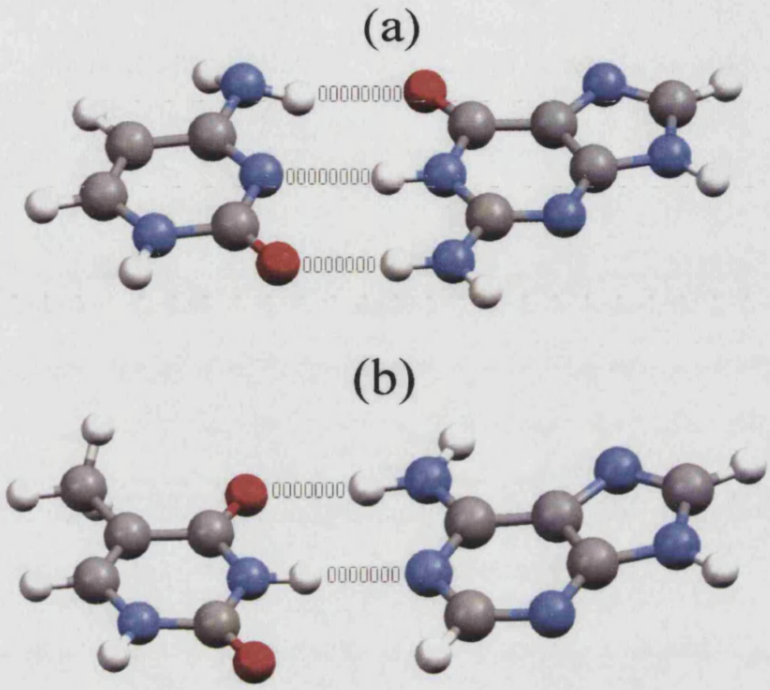

Figure 5.1: DNA base pairs. (a) The cytosine-guanine (CG) pair, and (b) the adenine-thymine (AT) pair. The pyrimidines are on the left of the figure, the purines on the right. The broken lines indicate hydrogen bonds.

strands pair by pair can be achieved by enzymes without breaking the covalently bonded backbone. Then, using free base molecules, each strand can be reconstructed into a new chain. However, since such small amounts of energy are required for these processes to occur, alteration to the base molecules via attack by free radicals can cause errors in the replicating process, leading to base-pair mismatch, bond breakage, and cleavage of the phosphate backbone. Previous work, both experimental and theoretical, has been carried out on the nature of radicals formed by hydrogen and muonium addition to these base pairs [4, 95, 131], but this chapter presents the first calculations on all possible hydrogen/muonium binding sites which include the quantum-mechanical properties of

the adduct forming particle, allowing isotope dependent effects to be studied.

5.1 Energies of the Adducts

In this section the potential hydrogen/muonium binding sites are identified for each of the four base molecules. Using the parametrised correlation model described in Chapter 4, unrestricted Hartree-Fock calculations were performed, again using the modified version of Gaussian 98, with electron correlation energies being calculated using Möller-Plessett perturbation theory at the MP4 level. The total energies obtained via these calculations are compared to identify the most stable adducts, which should be experimentally observable.

5.1.1 Cytosine

Figure 5.2 shows the cytosine molecule, with the six potential binding sites numbered. In cytosine, four of the potential adducts are formed by addition to an unsaturated carbon atom, one by addition to an unsaturated nitrogen atom, and one by addition to an unsaturated oxygen atom. The geometries of each of the six adducts were optimised at the MP4 level of theory, with the adduct particle being represented by a point charge. The calculated structures were then used to evaluate the total energies within the parametrised correlation model. It was shown in Sections 4.3 and 3.4 that the effects of correlation between the hydrogen-like nucleus and the electron density results in only a small change in the electron density distribution, and so the error incurred in using a point charge for the geometry optimisation was expected to be small. It should be borne in mind however, that the energy differences between adducts may also be very small, and since the error introduced by using a point charge in the geometry optimisation was dependent on the atom with which the HLN had formed

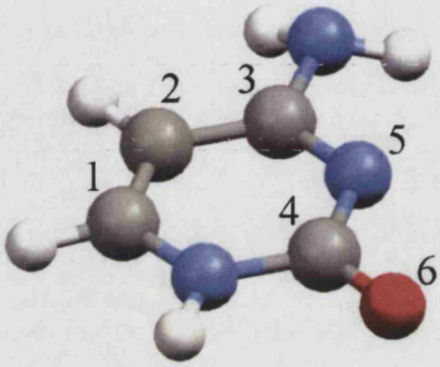

Figure 5.2: The cytosine molecule, with the six potential binding sites marked. In this and the following figures, white atoms represent hydrogen, grey carbon, blue nitrogen, and red oxygen.

a bond (due to the fact that the correlation energy is dependent on the type of bond formed), differences in total energies between adducts formed by addition to different atoms should be treated with caution if the difference is small. Table 5.1 shows the zero-point energy and energy eigenvalue of the hydrogen-like nucleus, along with the total energy of the system relative to the lowest energy structure. Classical total energies, $E_T^{(c)}$, are also given. The nomenclature used here is n-H-cytosine for the hydrocytosine adduct formed by addition at the site marked n in Figure 5.2, and n-Mu-cytosine for the muonated isotopomer of this adduct. This nomenclature will be used throughout the remainder of this chapter. As can be seen, the inclusion of quantum effects stabilises the C-X bond relative to the N-X and O-X bonds, and stabilises the N-X bond relative to the O-X bond. However, the adduct formed by addition to the unsaturated nitrogen atom is energetically most stable.

Figure 5.3 shows the molecular structure of each of the three lowest energy

Adduct	ZPE_μ (eV)	ε_μ (a.u.)	$E_T^{(\mu)}$ (eV)	$E_T^{(c)}$ (eV)
1-Mu-cytosine	0.520	-1.01656	0.339	0.458
2-Mu-cytosine	0.525	-0.99796	0.068	0.200
3-Mu-cytosine	0.529	-1.03023	1.464	1.558
4-Mu-cytosine	0.528	-1.02961	1.437	1.526
5-Mu-cytosine	0.570	-0.94074	0.000	0.000
6-Mu-cytosine	0.546	-0.87030	0.871	0.852

Adduct	ZPE_p (eV)	ε_p (a.u.)	$E_T^{(p)}$ (eV)	$E_T^{(c)}$ (eV)
1-H-cytosine	0.190	-1.05539	0.426	0.458
2-H-cytosine	0.201	-1.03634	0.164	0.200
3-H-cytosine	0.205	-1.06987	1.537	1.558
4-H-cytosine	0.205	-1.06898	1.507	1.526
5-H-cytosine	0.235	-0.98279	0.000	0.000
6-H-cytosine	0.210	-0.91253	0.857	0.852

Table 5.1: Energies of the six adducts formed by addition to cytosine. In order, these are the HLN zero-point energy, the ground state HLN eigenvalue, and the total energy of the system relative to the most stable adduct. Energies are given for a quantum muon (μ), quantum proton (p), and classical particle (c).

adducts of cytosine. For the lowest energy adduct, 5-X-cytosine, there is very little deformation of the six member ring, and so the delocalised electron density around this ring remains relatively unaffected. The amino group is rotated so as to be perpendicular to the plane of the ring. In 2-X-cytosine, a large, twisted deformation of the ring can be observed, with the amino group flattening and aligning to the deformation of the ring. Finally, in 1-X-cytosine, the ring structure is again largely unaffected, with the amino group flattening and aligning to the ring. From π-electron theory, the six electron system is disturbed by the formation of an adduct, leaving a five orbital structure. Since nitrogen is more electronegative than carbon, it would be expected that adduct formation via saturation of carbon bonds would be energetically the most stable. However, in

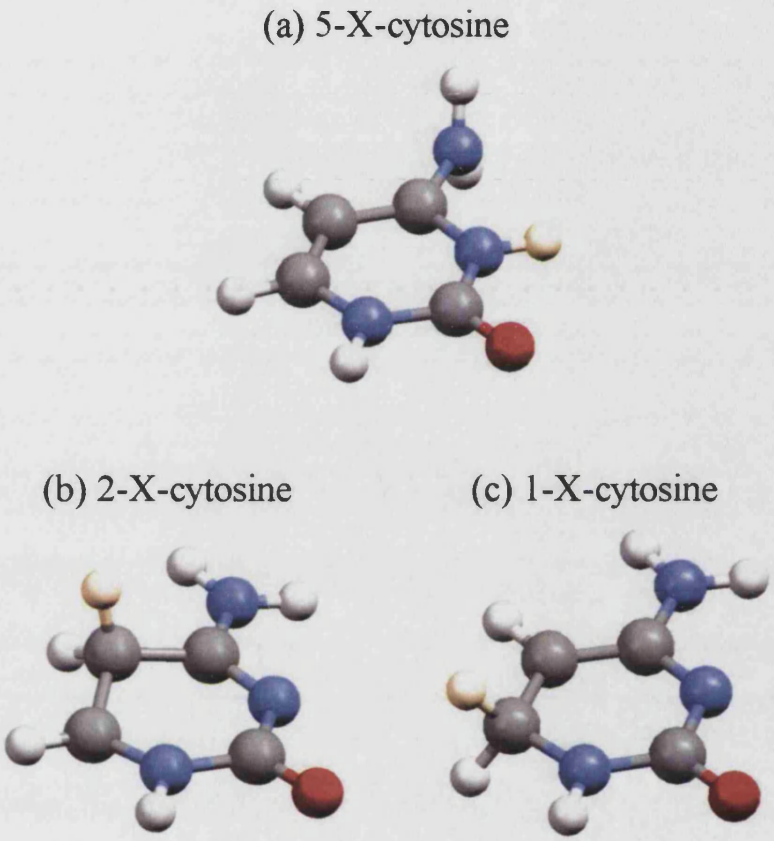

Figure 5.3: The three lowest energy adducts in order of increasing energy, formed by the addition of hydrogen/muonium to the cytosine molecule. H/Mu is represented by the atom shaded gold.

the case of cytosine, there is large deformation of the ring associated with adduct formation in 2-X-cytosine, which presumably lowers the bonding energy in the ring, and raises the total energy of the system above that of the adduct formed at the nitrogen.

5.1.2 Thymine

Figure 5.4 shows the thymine molecule with the six potential hydrogen/muonium binding sites numbered. In this case, four of the adducts are formed by addition

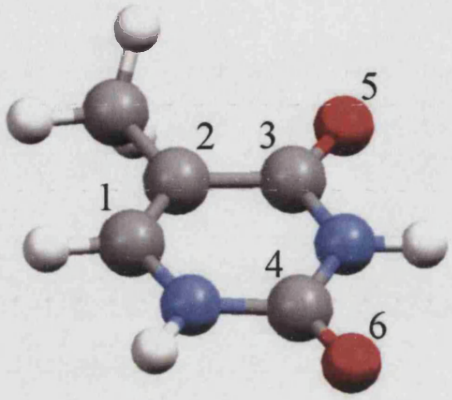

Figure 5.4: The thymine molecule, with the six potential binding sites marked.

to an unsaturated carbon molecule, and two by addition to an unsaturated oxygen molecule. Calculations were performed in the same manner as described in Section 5.1.1, and Table 5.2 summarises the results. In this case, addition to an unsaturated carbon yields the most stable adduct, and again the stabilisation of the C-X bond relative to the O-X bond is observed when quantum effects are included.

Figure 5.5 shows the two lowest energy adducts of the thymine molecule. For the lowest energy adduct, there is a large deformation of the six member ring structure, but this deformation is localised to the atom at which the adduct is formed and its nearest neighbours. The methyl group rotates to a staggered formation relative to the adduct particle. For the next lowest energy adduct, there is very little deformation of the molecule, with the hydrogens associated with the carbon saturated by addition of the adduct particle forming the expected structure. It may be expected that the π-electron system is more greatly disturbed in the formation of 1-X-thymine than in 2-X-thymine.

Adduct	ZPE_μ (eV)	ε_μ (a.u.)	$E_T^{(\mu)}$ (eV)	$E_T^{(c)}$ (eV)
1-Mu-thymine	0.522	-1.00616	0.107	0.106
2-Mu-thymine	0.533	-1.00106	0.000	0.000
3-Mu-thymine	0.529	-0.99540	1.174	1.155
4-Mu-thymine	0.530	-0.98523	1.547	1.518
5-Mu-thymine	0.553	-0.87023	0.991	0.840
6-Mu-thymine	0.555	-0.88074	1.377	1.230

Adduct	ZPE_p (eV)	ε_p (a.u.)	$E_T^{(p)}$ (eV)	$E_T^{(c)}$ (eV)
1-H-thymine	0.194	-1.04520	0.106	0.106
2-H-thymine	0.209	-1.04003	0.000	0.000
3-H-thymine	0.207	-1.03320	1.164	1.155
4-H-thymine	0.209	-1.02471	1.530	1.518
5-H-thymine	0.207	-0.91335	0.876	0.840
6-H-thymine	0.208	-0.92319	1.264	1.230

Table 5.2: Energies of the six adducts formed by addition to thymine. In order, these are the HLN zero-point energy, the total HLN energy, and the total energy of the system relative to the most stable adduct. Energies are given for a quantum muon, quantum proton, and classical particle

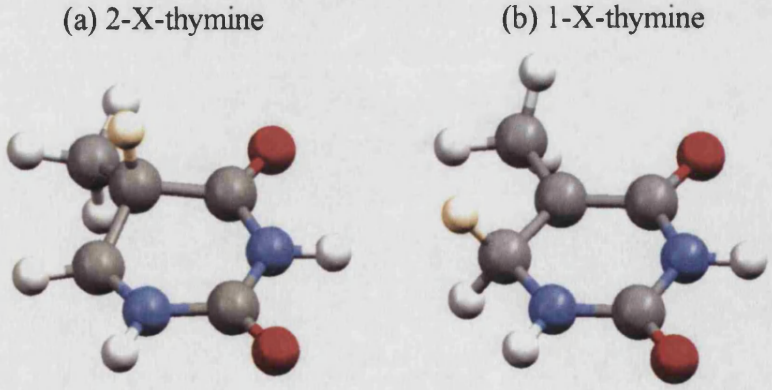

Figure 5.5: The two lowest energy adducts in order of increasing energy, formed by the addition of hydrogen/muonium to the thymine molecule.

5.1.3 Guanine

Guanine and adenine, the purine molecules in their respective DNA base pairs, have a double ring structure, a six member ring (similar in structure to those of cytosine and thymine) attached along a double carbon bond to a five member ring. This results in eight potential hydrogen/muonium binding sites, which can be seen numbered in Figure 5.6, which shows the guanine molecule. Table 5.3 shows the results of the single point energy calculations performed on these adducts. Again the C-X bond is stabilised relative O-X bond when quantum mechanical effects are included, and the lowest energy adduct, formed by addition to an unsaturated carbon, is stabilised relative to all other adducts, including those formed by addition to other unsaturated carbons, by the inclusion of these effects. An interesting new feature also appears in these calculations. the 7-H-guanine adduct is stable relative to 1- and 2-H-guanine in both the classical and quantum cases, but for the lighter muon, 1- and 2-Mu-guanine are both stabilised relative to 7-Mu-guanine. All three of these adducts are significantly higher in energy than the most stable adduct, and so would not be expected to be observed experimentally, but nevertheless, these calculations show that the inclusion of quantum mechanical effects are particularly important for a particle as light as the muon.

Figure 5.7 shows the two lowest energy adducts of guanine. For the lowest energy adduct, there is very little deformation of the molecular structure, with only the expected tetrahedral rearrangement of the C-H bonds on the saturated carbon to accommodate the adduct particle observed. For the next lowest energy adduct, there is some local deformation of the five member ring structure at the carbon nearest to the now saturated nitrogen, along with a tilting of the

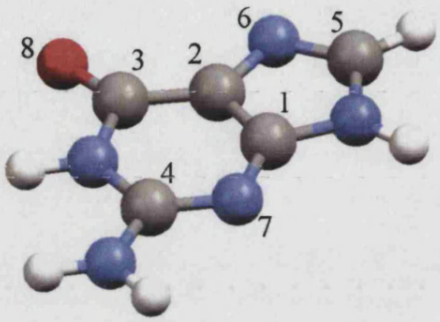

Figure 5.6: The guanine molecule, with the eight potential binding sites marked.

Adduct	ZPE_μ (eV)	ε_μ (a.u.)	$E_T^{(\mu)}$ (eV)	$E_T^{(c)}$ (eV)
1-Mu-guanine	0.530	-1.03452	0.697	0.677
2-Mu-guanine	0.534	-1.01518	0.712	0.702
3-Mu-guanine	0.529	-1.01323	1.161	1.139
4-Mu-guanine	0.528	-1.02732	0.751	0.715
5-Mu-guanine	0.517	-1.02925	0.000	0.000
6-Mu-guanine	0.560	-0.95445	0.466	0.358
7-Mu-guanine	0.565	-0.90905	0.735	0.620
8-Mu-guanine	0.551	-0.89979	0.943	0.792

Adduct	ZPE_p (eV)	ε_p (a.u.)	$E_T^{(p)}$ (eV)	$E_T^{(c)}$ (eV)
1-H-guanine	0.205	-1.07249	0.684	0.677
2-H-guanine	0.214	-1.05466	0.708	0.702
3-H-guanine	0.208	-1.04828	1.149	1.139
4-H-guanine	0.200	-1.06553	0.728	0.715
5-H-guanine	0.189	-1.06706	0.000	0.000
6-H-guanine	0.224	-0.99524	0.386	0.358
7-H-guanine	0.228	-0.94991	0.650	0.620
8-H-guanine	0.208	-0.94170	0.832	0.792

Table 5.3: Energies of the eight adducts formed by addition to guanine. In order, these are the HLN zero-point energy, the total HLN energy, and the total energy of the system relative to the most stable adduct. Energies are given for a quantum muon, quantum proton, and classical particle

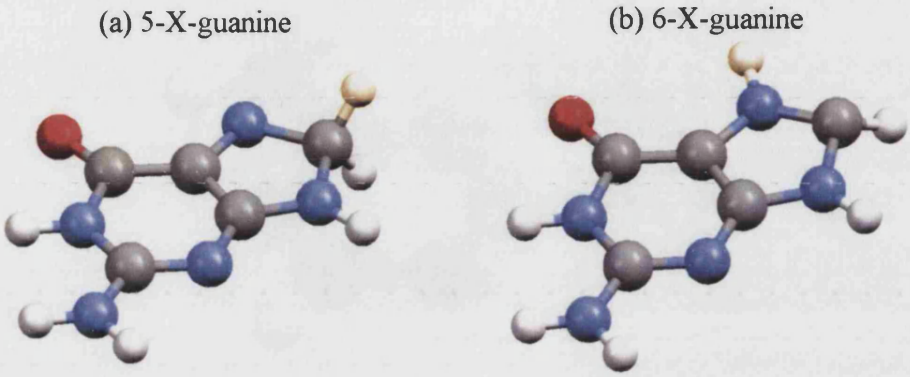

Figure 5.7: The two lowest energy adducts in order of increasing energy, formed by the addition of hydrogen/muonium to the guanine molecule.

respective C-X and N-X bonds out of the plane of the ring.

5.1.4 Adenine

The final DNA base molecule adenine also has the two ring structure observed in guanine, along with the eight potential hydrogen/muonium binding sites. In this case, five of the adducts are formed by addition to unsaturated carbon, two by addition to an unsaturated nitrogen, and one by addition to an unsaturated oxygen. Figure 5.8 shows the adenine molecule, with the potential binding sites numbered. Table 5.4 summarises the results of calculations performed on these systems. Again the most stable adduct, formed by addition to an unsaturated carbon, is stabilised by the inclusion of quantum mechanical effects, and again these effects result in a classically less stable adduct, 2-Mu-adenine, becoming stabilised relative to 7-Mu-adenine. In this case however, this relative stabilisation is also predicted at the proton mass. The energies are again significantly higher than those of the most stable adduct, and so this is not expected be experimentally observable.

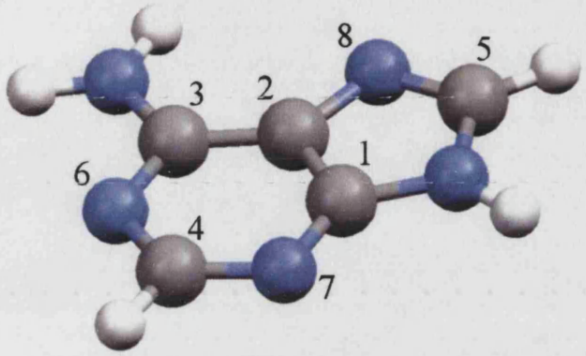

Figure 5.8: The adenine molecule, with the eight potential binding sites marked.

Adduct	ZPE_μ (eV)	ε_μ (a.u.)	$E_T^{(\mu)}$ (eV)	$E_T^{(c)}$ (eV)
1-Mu-adenine	0.529	-1.01792	1.351	1.340
2-Mu-adenine	0.535	-1.01236	0.675	0.666
3-Mu-adenine	0.529	-1.03796	1.147	1.127
4-Mu-adenine	0.518	-1.03649	0.388	0.388
5-Mu-adenine	0.516	-1.01960	0.000	0.000
6-Mu-adenine	0.564	-0.94966	1.108	0.988
7-Mu-adenine	0.559	-0.93551	0.769	0.657
8-Mu-adenine	0.555	-0.93872	1.952	1.843

Adduct	ZPE_p (eV)	ε_p (a.u.)	$E_T^{(p)}$ (eV)	$E_T^{(c)}$ (eV)
1-H-adenine	0.205	-1.05596	1.345	1.340
2-H-adenine	0.214	-1.05219	0.671	0.666
3-H-adenine	0.203	-1.07630	1.134	1.127
4-H-adenine	0.193	-1.07424	0.388	0.388
5-H-adenine	0.187	-1.05737	0.000	0.000
6-H-adenine	0.224	-0.99064	1.017	0.988
7-H-adenine	0.214	-0.97630	0.681	0.657
8-H-adenine	0.211	-0.97839	1.868	1.843

Table 5.4: Energies of the eight adducts formed by addition to adenine. In order, these are the HLN zero-point energy, the total HLN energy, and the total energy of the system relative to the most stable adduct. Energies are given for a quantum muon, quantum proton, and classical particle

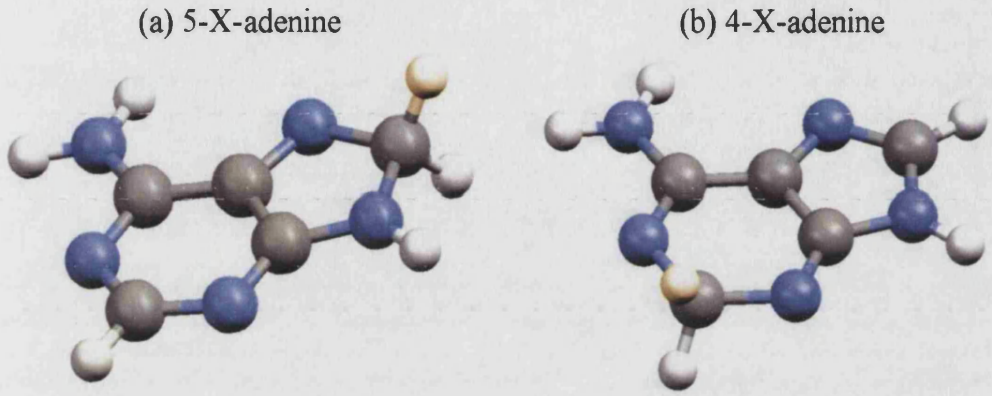

Figure 5.9: The two lowest energy adducts in order of increasing energy, formed by the addition of hydrogen/muonium to the adenine molecule.

Figure 5.9 shows the two most stable adducts of adenine, but as can be seen, there is very little deformation of molecular structure upon formation of the adduct.

5.2 Hyperfine Couplings

The hyperfine interaction is a manifestation of spin-spin coupling between the hydrogen-like nucleus and the electron density. Of most interest here is the isotropic or Fermi contact interaction, A. If the hydrogen-like nucleus is assumed to be point-like, the contact term can be calculated using the spin Hamiltonian

$$A = -\frac{2}{3}\mu_0 g_e \gamma_e \gamma_N \left|\varphi_e(0)\right|^2 \mathbf{s} \cdot \mathbf{I}, \tag{5.1}$$

where $|\varphi_e(0)|^2$ is the electron spin density at the nucleus. This term is calculated in Gaussian 98. However, the value of A can be affected when the vibrational properties of the hydrogen-like nucleus are included if the electron spin density at the nucleus varies significantly over its vibrational motion [21, 135]. The

System	A_p (MHz)	$\langle A_p \rangle$ (MHz)	A_μ (MHz)	$\langle A_\mu \rangle$ (MHz)
5-X-cytosine	-14.6225	-17.95251	-46.54584	-14.45560*
2-X-cytosine	128.66901	149.43461	409.59848	620.79356
1-X-cytosine	104.01066	108.06812	331.10234	422.16991
2-X-thymine	129.90701	144.30129	405.78954	585.59735
1-X-thymine	102.01008	105.29796	325.73536	423.84734
5-X-guanine	118.14318	124.23390	376.09109	507.97618
6-X-guanine	-21.67185	-20.46879	-68.98908	-31.83676*
5-X-adenine	111.24166	116.52294	354.12114	465.78288
4-X-adenine	150.39983	156.95422	478.77530	617.28966

Table 5.5: classical and vibrationally averaged hyperfine coupling constants for the low energy DNA base molecule adducts

hyperfine contact term is then given by

$$\langle A \rangle = \int A(\mathbf{r}) \left|\varphi_\mu(\mathbf{r})\right|^2 d\mathbf{r}, \tag{5.2}$$

where $A(\mathbf{r})$ is the 'static' value of A when the point charge is located at $\mathbf{r}$, and $\left|\varphi_\mu(\mathbf{r})\right|^2$ is the nuclear density at $\mathbf{r}$. As will be seen, this vibrational averaging can lead to a large deviation of the contact term from the static value, especially for a particle as light as the muon.

Vibrationally averaged hyperfine coupling constants were calculated for both the muon and proton in the adducts discussed in Section 5.1. These calculations were carried out in a similar manner to those used in the parametrisation of the correlation model discussed in Chapter 4. In this case the electron spin density was sampled at approximately fifty points around the equilibrium position of the hydrogen-like nucleus. These samples were then used to construct a spin density surface, and the averaging given by Equation 5.2 was evaluated numerically. Table 5.5 summarises the results. Here the hyperfine coupling constant A is expressed as a frequency, not an energy, and so a more accurate description

System	$\langle A_p \rangle / A_p$ (MHz)	$\langle A_\mu \rangle / A_\mu$ (MHz)	$\langle A'_\mu \rangle / \langle A_p \rangle$ (MHz)
5-X-cytosine	1.22773	0.31055*	0.25295*
2-X-cytosine	1.16139	1.51561	1.30500
1-X-cytosine	1.03901	1.27504	1.22717
2-X-thymine	1.11080	1.44279	1.29887
1-X-thymine	1.03223	1.30120	1.26057
5-X-guanine	1.05155	1.35067	1.28446
6-X-guanine	0.94449	0.46148*	0.48860*
5-X-adenine	1.04748	1.31532	1.25570
4-X-adenine	1.04358	1.28931	1.23547

Table 5.6: ratios of vibrationally averaged to classical hyperfine coupling constants, and a measure of the residual isotope effect in the low energy DNA base molecule adducts

would be A/h. However, in line with the literature, A will be used, but values will be quoted in MHz.

Of interest are two ratios of these hyperfine coupling constants. The first, $\langle A \rangle / A$, gives a measure of the inaccuracy of calculated hyperfine coupling constants if vibrational effects are neglected, whilst the second, $\langle A'_\mu \rangle / \langle A_p \rangle$, where A'_μ is the reduced muon hyperfine coupling constant, given by

$$A'_\mu = \frac{\gamma_p}{\gamma_\mu} A_\mu, \tag{5.3}$$

gives a direct theoretical estimate of the residual isotope effect experimentally observed in many systems, e.g. [110]. Table 5.6 gives these ratios for the various low energy adducts. As can be seen the isotope effects can be very large, even for the relatively localised proton, and so the theoretical hyperfine coupling constant at the equilibrium geometry can only be used as an approximate value with which to interpret experimental data. Since experimental measurement of the hyperfine coupling constant is one of the key tools for site identification [24], it is very important that a theoretical treatment takes account of vibrational averag-

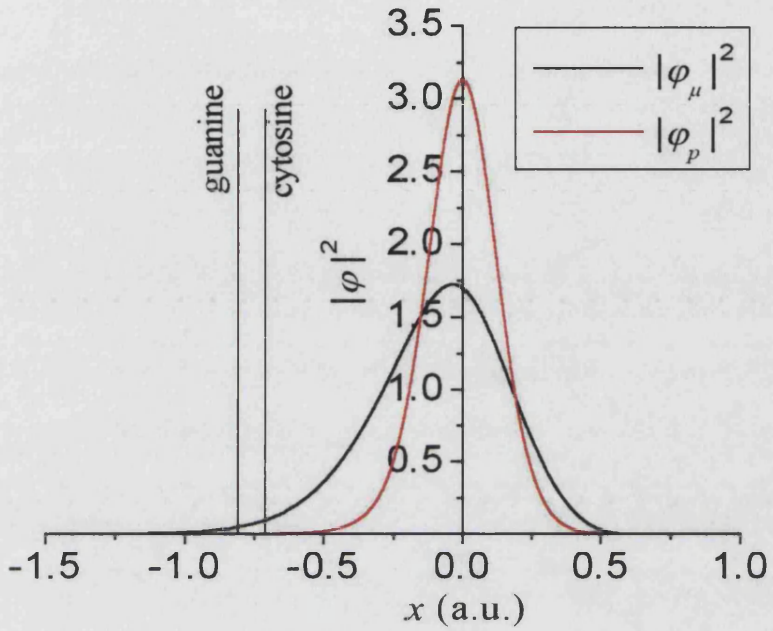

Figure 5.10: Probability densities for the muon and proton in 5-X-cytosine and 6-X-guanine. Vertical lines mark the point at which the non-adiabatic change in electron density occurs

ing when predictions of binding sites are attempted. This is highlighted by two of the systems studied here, namely 5-X-cytosine and 6-X-guanine (marked by asterisks in Tables 5.5 and 5.6). Both of these adducts are formed by addition of hydrogen/muonium at an unsaturated nitrogen, and 5-X-cytosine is predicted to be energetically the most stable cytosine adduct. In contrast to the typical residual isotope effects of approximately 25% predicted here, these two systems show the reverse effect. A more detailed study reveals that a non-adiabatic change in the electron density occurs during the vibrational motion of the muon. At this point the highest occupied molecular orbital (HOMO) changes from a somewhat delocalised state, with the majority of the spin density being associated with the next nearest carbon neighbour, to a state resembling that of atomic hydrogen.

This results in a large and instantaneous change in the spin density at the muon to a level close to that of atomic hydrogen. After this non-adiabatic change occurs, the lowest energy configuration for the system is that of the original base molecule and free muonium. Figure 5.10 shows the probability densities for the muon and the proton, along with the points at which this non-adiabatic change in the electron density occurs for the two systems. As can be seen, the probability of finding the proton at this distance is negligible (and indeed, most of the change in the hyperfine coupling constants in these systems comes from vibrational averaging *normal* to the bond), whilst for the muon, it is significant. This implies that whilst this system may be stable if the adduct is formed by hydrogen addition, it's analogous system formed by muonium addition will not be. This is particularly interesting since this difference is not due to the energetics of the system, but due to the *amplitude* of the HLN zero-point motion.

5.3 Comparisons to Other Work

Barnabas *et al.* [4] have carried out muon level-crossing resonance experiments on thymine, where they assumed that adducts were formed by addition to carbons 1 and 2 of Figure 5.4, in agreement with the calculations presented here. The observed hyperfine coupling constants were 323 MHz (compared to 585.59735 MHz here), and 371 MHz (compared to 423.84734 MHz here) respectively. There are several possible reasons for this discrepancy in the observed and calculated hyperfine coupling constants. Firstly, the experimental results were obtained in solution and so the effects of the solution on both the electron density and the muon itself cannot be ignored. Secondly, the relaxation of the adduct, performed using Gaussian 98, assumed it to be a free molecule, and so distortions to the molecular structure could have been overemphasised.

Adduct	A_μ (MHz) [95]	$\langle A_\mu \rangle$ (A_μ) (MHz) (this work)
5-Mu-cytosine	-27.3	-14.45560 (-46.54584)
2-Mu-cytosine	392.4	620.79356 (409.59848)
1-Mu-cytosine	534.0	422.16991 (331.10234)
2-Mu-thymine	459.2	585.59735 (405.78954)
1-Mu-thymine	374.0	423.84734 (325.73536)
5-Mu-guanine	391.7	507.97618 (376.09109)
6-Mu-guanine	-52.4	-31.83676 (-68.98908)
5-Mu-adenine	82.3	465.78288 (354.12114)
4-Mu-adenine	514.4	617.28966 (478.77530)

Table 5.7: Comparison of hyperfine coupling constants calculated by Oganesyan *et al.* and those calculated in this work.

Finally, the calculations presented here were performed using the MP4/6-31G model chemistry, and so, although electron-electron correlation was included in the total energy calculations, it was included using a post-SCF method, and so has no effect on the electron density distribution itself. This allows for the possibility that the spin density distribution could be significantly different if electron-electron correlation effects are included in the SCF cycle. It would be useful for experimental data on crystallised DNA samples to be obtained, so that the reasons for the discrepancies between the experimental and theoretical data postulated above could be considered more quantitatively.

Calculations presented here predicted 2-X-thymine to be more stable than 1-X-thymine by approximately 0.1 eV. Barnabas *et al.* predict a radical yield ratio of 2-Mu-thymine/1-Mu-thymine of 1 ± 0.3, while von Sonntag [131] quotes a ratio of 2.2 for the protonated case, and so both of these experimental results are in broad agreement with calculation. It is worth noting here that 1,2-dihydrothymine, formed by hydrogen addition at both of the predicted lowest energy binding sites, is observed experimentally [56].

Radical	Bond	A'_μ/A_p (Reference)
Hydroxyl	O-X	1.24 ([21]T); 1.27 ([130]T)
Isopropyl		1.38 ([110]E)
tert-Butyl		1.44 ([110]E)
cyclohexadienyl	C-X	1.21 ([43]E, [109]E)
C_{60} exo-adduct	C-X	1.07 ([9]T); 1.09 ([3]E, [90]E)
Methyl	C-X	1.02 ([2]T)
Ethyl	C-X	1.15 ([15]T); 1.16 ([21]T); 1.38 ([110]E)
Formyl		1.18 ([135]T)

Table 5.8: Residual isotope effects in various radical systems. In the third column, T=theoretical and E=experimental result.

Oganesyan *et al.* [95] have a completed a theoretical investigation of the hyperfine coupling constants for all of the adducts discussed in this chapter. Their results are compared to those of this work in Table 5.7. There is general agreement with the static values (A_μ) calculated here across the systems, with some notable exceptions, 1-Mu-cytosine and 5-Mu-adenine. Again discrepancies are probably due to a more sophisticated model chemistry with a higher quality basis set being used in [95]. Of greater importance however is the difference between $\langle A_\mu \rangle$ and A_μ presented here. This vibrational averaging appears to have been ignored in [95], and so any attempts at site identification using these values should be treated with caution.

A much larger body of work exists on the subject of the residual isotope effect. Table 5.8 summarises these results. As can be seen, the residual isotope effect can vary a great deal between systems, accounting for over 30% of the hyperfine coupling constant of the muon. Of course, a detailed analysis of the behaviour of the electron spin density distribution as a function of geometry would be required to fully understand the differences between these systems, in addition to a more sophisticated vibrational averaging method than that applied here.

The method used here should be reliable for the muon, since its lighter mass leads to high vibrational frequencies and a decoupling from the other normal modes of a given system, but its validity for the proton is questionable, since the vibrational motion of the heavier particle will be coupled to other vibrational modes of the system. This could account for the theoretical underestimation of the residual isotope effect observed in the ethyl radical.

The experimental residual isotope effect observed for the cyclohexadienyl radical is in reasonable agreement with the values calculated in this work. This is encouraging since in five of the seven systems shown in Table 5.6, wherein the adduct is formed by addition to an unsaturated carbon, the adduct structure resembles that of the cyclohexadienyl radical, and so bond properties would be expected to be similar. The average value of the residual isotope effect in these five systems is 1.262, compared to the experimental value for the cyclohexadienyl radical of 1.21.

Summary

All potential binding sites of the HLN to the four DNA base molecules have been studied. As can be seen, the inclusion of a quantum mechanical description of the HLN resulted in very little change with respect to the relative energies of the adducts, particularly for the most stable adducts. This suggests that the classical model is very succesful in calculating these relative energies, and this is due to the fact that the effects of the HLN-electron correlation appear to be similar for each of the adducts. This similarity means that total energy differences of an order of magnitude smaller than correlation energies are preserved when the PCM is applied. The quantum motion of the HLN cannot however be ignored when hyperfine coupling constants are being evaluated, since this motion can

lead to deviations of up to 50% from the values calculated using a classical model.

Chapter 6

Interaction of H and Mu with Diamond Dopants

It has long been realised that hydrogen is a ubiquitous impurity in diamond, where concentrations of up to 1 at.% have been reported [30, 120]. Many theoretical calculations have been performed in order to better understand the structural and electronic environments of hydrogen and muonium in diamond, with μSR data, revealing two distinct muonium states, proving extremely useful in these attempts. Reviews are available, e.g. [51], and an overview can be found in Section 1.3.

More recently, interest has grown in diamond as a useful semiconductor, where its high carrier mobility and thermal conductivity, along with its low dielectric constant and wide band gap [67] make it a promising candidate for a high frequency, high power, high temperature, and high irradiation-tolerant semiconducting device [93]. For this to be realised, however, low-resistivity n-type and p-type diamond must be fabricated. Attempts to create p-type diamond using boron as an acceptor have met with some success, although there is no clear experimental evidence supporting a given structure for the B-H complex, but the fabrication of n-type diamond is much more challenging. Dopant candidates are

nitrogen, phosphorus, and sulphur. Nitrogen has a high solubility in diamond due to its low defect formation energy of -3.4 eV [71], but acts as a deep donor, with an activation energy of 1.7 eV [41], making N-doped diamond insulating at room temperature. High doping with P is difficult since the defect formation energy is very high at +10.4 eV [71], partly due to the significant lattice distortion associated with the large substitutional atom. When incorporated, phosphorus gives a deep donor level lying around 0.6 eV below the conduction band [123]. Sulphur acts as a double donor in diamond, and S-doped n-type diamond has been obtained [59]. However, location of the donor level has proved difficult, with reports of levels being very close to the conduction band [115], or being rather deep [133].

The inclusion of hydrogen further complicates the situations discussed above. Hydrogen passivates both donors and acceptors in diamond [51], removing the electronically active levels from the band gap, and so more research is required in order to understand how this occurs, and what, if anything, can be done in order to produce high quality material containing hydrogen. In this chapter the interaction of H and Mu with substitutional P and S is considered, in addition to the interaction of H and Mu with various impurity-vacancy complexes.

6.1 Parametrisation of the P-X and S-X bonds

Before the present calculations on the P-X and S-X complexes in diamond were performed, it was important to attempt to model the P-X and S-X bonds in some small analogous molecules, as was carried out in the parametrisation of the C-X, N-X, and O-X bonds in Chapter 4. The reasons for this are two-fold. Firstly, the information gained about the nature of these bonds can be used to understand the observed differences in the solid state, and secondly, the

parametrisation calculated for these small molecules can be used in the solid-state calculation in order to ascertain whether the same parametrisation is valid, or if reparametrisation must be performed.

6.1.1 Reference Systems

The reference systems used for the parametrisation of the P-X bond were isotopomers of phenylphosphine (C_6H_6PX), the phosphino radical (HPX), phosphethene (CH_2PX), and hypophosphorus acid (H_2O_2PX). Hypophosphorus acid was chosen as a reference system so as to investigate whether the parametrisation is dependent on the P-X bond alone, or if longer range effects are important, i.e. would parametrisation based on the fact that H (or Mu) was a component of a functional group be more appropriate?

The reference systems for parametrisation of the S-X bond were all open shell systems. They were adducts of thioacetone (C_3H_6SX), thioformamide (CH_3NSX), thioacetamide (C_2H_5NSX), and thiobenzamide (C_7H_7NSX). Figures 6.1 and 6.2 show the optimised structures for these reference systems. The potential energy surface on which the HLN moves was again obtained for each system. It was assumed that the PES was separable into a contribution along the bond, and contributions from each of two directions normal to this and each other. When these surfaces were obtained, the Schrödinger equation was solved numerically for the muon, proton and deuteron mass. The results of these calculations can be seen in Tables 6.1 and 6.2.

When compared to the zero-point energies and bond length increases calculated for the C-X, N-X, and O-X, and presented in tables 4.4, 4.7, and 4.10, it can be seen that the zero-point energies are on average 25-30% lower for the P-X and S-X bonds. The bond length increases are only slightly larger for the muon,

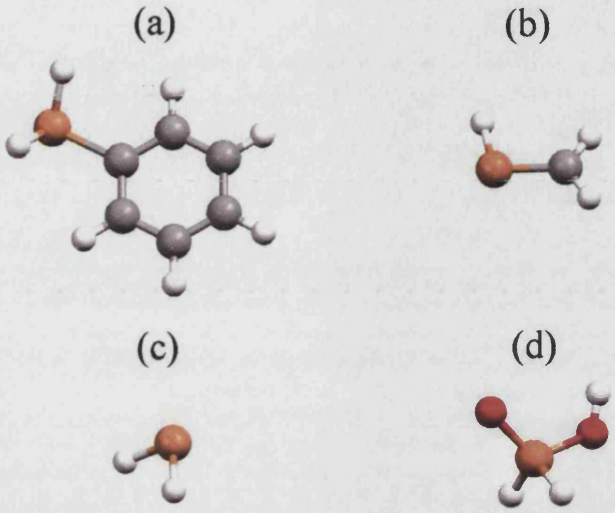

Figure 6.1: P-X bond reference systems showing the isotopomers of a) phenylphosphine, b) phosphethene, c) the phosphino radical, and d) hypophosphorous acid.

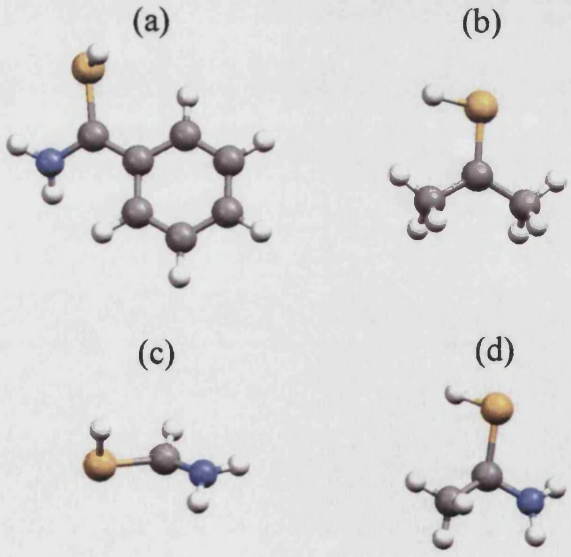

Figure 6.2: S-X bond reference systems showing the isotopomers of a) thiobenzamide, b) thioacetone, c) thioformamide, and d) thioacetamide.

System	ZPE_x	ZPE_y	ZPE_z	$ZPE_{Tot.}$	Δx (Å)
C_6H_6PMu	0.212	0.088	0.078	0.378	0.054
C_6H_6PH	0.072	0.029	0.025	0.126	0.024
C_6H_6PD	0.050	0.020	0.018	0.088	0.021
HPMu	0.216	0.081	0.051	0.348	0.055
HPH	0.071	0.027	0.013	0.111	0.019
HPD	0.051	0.019	0.008	0.078	0.014
CH_2PMu	0.207	0.091	0.067	0.365	0.055
CH_2PH	0.071	0.030	0.021	0.122	0.019
CH_2PD	0.051	0.021	0.014	0.086	0.014
H_2O_2PMu	0.225	0.095	0.092	0.412	0.051
H_2O_2PH	0.077	0.031	0.030	0.138	0.018
H_2O_2PD	0.055	0.022	0.021	0.098	0.013

Table 6.1: Results of numerical reference calculations performed on systems containing a P-X bond. Quoted energies are in eV

System	ZPE_x	ZPE_y	ZPE_z	$ZPE_{Tot.}$	Δx (Å)
C_3H_6SMu	0.238	0.093	0.051	0.382	0.049
C_3H_6SH	0.081	0.030	0.013	0.124	0.016
C_3H_6SD	0.058	0.021	0.008	0.087	0.012
CH_3NSMu	0.212	0.071	0.071	0.354	0.064
CH_3NSH	0.078	0.022	0.022	0.122	0.020
CH_3NSD	0.055	0.015	0.015	0.085	0.015
C_2H_5NSMu	0.234	0.071	0.074	0.379	0.052
C_2H_5NSH	0.080	0.022	0.023	0.125	0.018
C_2H_5NSD	0.057	0.015	0.016	0.088	0.013
C_7H_7NSMu	0.226	0.086	0.059	0.371	0.056
C_7H_7NSH	0.080	0.028	0.016	0.124	0.019
C_7H_7NSD	0.057	0.020	0.011	0.088	0.014

Table 6.2: Results of numerical reference calculations performed on systems containing an S-X bond. Quoted energies are in eV

but this increase is more pronounced for both the proton and the deuteron. This suggests that the PES is more anharmonic for these systems than for those considered previously, since both the proton and deuteron explore less of the PES than the muon. It should also be noted that for the isotopomers of hypophosphorous acid, H_2O_2PX, HLN zero-point energies are approximately 10% larger than in the other reference systems containing a P-X bond.

The parametrised correlation model described in Chapter 4 was used in an attempt to define the mass-dependent parameters for the P-X and S-X bonds. In contrast to the calculations of Chapter 4, wherein the separation between the two centres on which HLN basis functions were placed was found to be relatively insensitive to both classical bond length and HLN mass, it was found to be necessary here to increase the separation to $\sim$0.4 Å for calculation involving the muon, and to reduce this to $\sim$0.36 Å for the proton and deuteron. Again, results were reasonably insensitive to further variation about these values. Tables 6.3 and 6.4 show the correlation factors which best replicate the references calculations, along with the calculated zero-point energies and bond length increases. It can be seen that the correlation factors associated with the HLN in the isotopomers of hypophosphorous acid are significantly lower than those for the other systems containing a P-X bond. This supports the proposal at the beginning of this section that the atomic species to which the HLN is bonded may not in itself be enough to define the correlation factor. In this case, the fact that the phosphorus to which the HLN is bonded is itself bonded to an oxygen, in contrast to the other reference systems, in which P is bonded to C or H.

System	f_c	ZPE_C (eV)	$\frac{ZPE_C}{ZPE_N}$	Δx_C (Å)	$\frac{\Delta x_C}{\Delta x_N}$
C_6H_6PMu	0.638	0.372	0.98	0.051	0.94
C_6H_6PH	0.706	0.116	0.92	0.016	0.67
C_6H_6PD	0.715	0.091	1.03	0.008	0.38
HPMu	0.638	0.347	1.00	0.057	1.04
HPH	0.705	0.115	1.04	0.017	0.89
HPD	0.717	0.072	0.92	0.012	0.86
CH_2PMu	0.638	0.367	1.01	0.052	0.95
CH_2PH	0.704	0.126	1.03	0.014	0.74
CH_2PD	0.715	0.076	0.88	0.011	0.79
H_2O_2PMu	0.614	0.415	1.01	0.042	0.82
H_2O_2PH	0.691	0.133	0.96	0.013	0.72
H_2O_2PD	0.703	0.100	1.02	0.009	0.69

Table 6.3: Zero-point energies and increases in bond lengths as calculated using the parametrised correlation model for the P-X bond

6.2 HLN-Impurity Complexes in Diamond

6.2.1 The PX complex

In keeping with previous calculations, equilibrium structures were obtained using a point defect to represent the HLN, and PCM calculations were subsequently performed using these structures. To study the PX complex, a $C_{35}H_{40}PH$ diamond cluster, centred on an anti-bonding site, was used, with the unrelaxed C-C bond length set to 1.545 Å, and the bond length between the carbons and the saturating hydrogens being set to 1.09 Å. Geometry optimisation was performed at the UHF/6-31G level, and relaxation of the PH complex itself, along with the nearest and next nearest neighbour carbons was allowed, although it should be noted that the only symmetric distortions were considered. With this relaxation the minimum energy of the system was found when the interstitial hydrogen was at the anti-bonding site, in agreement with [93]. The relaxed structure can be

System	f_c	ZPE_P (eV)	$\frac{ZPE_P}{ZPE_N}$	Δx_P (Å)	$\frac{\Delta x_P}{\Delta x_N}$
C_3H_6SMu	0.606	0.384	1.01	0.047	0.96
C_3H_6SH	0.685	0.129	1.04	0.014	0.92
C_3H_6SD	0.695	0.080	0.92	0.009	0.75
CH_3NSMu	0.610	0.369	1.04	0.050	0.78
CH_3NSH	0.685	0.134	1.10	0.013	0.65
CH_3NSD	0.696	0.088	1.04	0.008	0.53
C_2H_5NSMu	0.606	0.382	1.01	0.048	0.92
C_2H_5NSH	0.685	0.125	1.00	0.015	0.83
C_2H_5NSD	0.695	0.080	0.91	0.10	0.77
C_7H_7NSMu	0.607	0.376	1.01	0.049	0.88
C_7H_7NSH	0.685	0.125	1.01	0.015	0.79
C_7H_7NSD	0.695	0.081	0.92	0.010	0.71

Table 6.4: Zero-point energies and increases in bond lengths and as calculated using the parametrised correlation model for the S-X bond

seen in Figure 6.3. The carbons nearest to the substitutional phosphorus can be seen to be noticeably displaced from the perfect crystal structure, and this can be seen more clearly when the local structure of the complex is studied more closely. The P-C_1 bond length is equal to 1.711 Å, an increase of 0.166 Å (10.7%). The P-C_2 bond length is equal to 1.784 Å, an increase of 0.239 Å (15.5%). The angle C_1PC_2 is equal to 105.32°, a decrease of 4.14° (3.8%). The angle PC_2C_3 is equal to 104.17°, a decrease of 5.19° (4.8%). Finally, the P-H bond length is equal to 1.326 Å, a decrease of approximately 10% from the standard value of around 1.43 Å calculated for the reference systems. This means that the effect of the PH complex is to displace the nearest neighbour carbons outwards from their equilibrium position by a significant amount, whilst as can be seen from the values of the two angles considered, the phosphorus itself is also displaced backwards from the prefect crystal substitutional site. Using the PCM, with the parameters $f_{c\mu}^P = 0.638$ and $f_{cp}^P = 0.704$ obtained from Section 6.1, the total

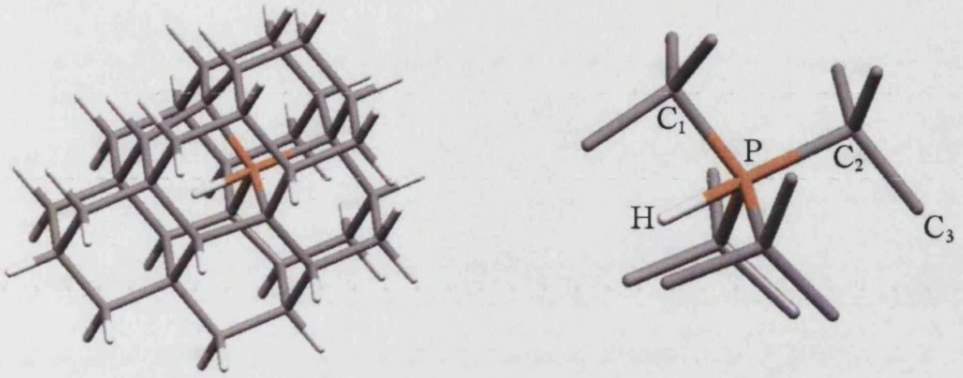

Figure 6.3: The UHF/6-31G relaxed structure of the $C_{35}H_{40}PH$ cluster

Particle	f_c	ZPE (eV)	E_T (a.u.)	E_D (eV)	Δx (Å)
μ^+	0.638	0.728	-1688.46063	2.127	0.015
p	0.704	0.339	-1688.51145	0.744	0.004
classical	n/a	n/a	-1688.53879	0.000	n/a

Table 6.5: ZPE, total energy, defect formation energy, and bond length increase for the P-X defect complexes

energy and the relative defect formation energy E_D can be found by comparing this system to one containing a point charge in place of the HLN (note: to obtain *absolute* defect formation energies, a more sophisticated calculation must be made. See [52] for details). In addition, the HLN zero-point energy can be calculated. Table 6.5 shows these different energies, and also includes the PCM calculated bond length increases. As can be seen, the zero-point energies of the HLN are predicted to be much larger than those encountered in the molecular systems, around 100% larger for the muon, and 200% larger for the proton, and the bond length increases are correspondingly reduced. Interestingly, the dependence of the defect formation energy on the HLN-electron correlation is large, and illustrates the fact that *post-hoc* methods, which only inlude the HLN

Particle	ZPE_x	ZPE_y	ZPE_z	ZPE_{Tot}	Δx (Å)
μ^+	0.288	0.201	0.199	0.688	0.029
p	0.099	0.068	0.067	0.234	0.009

Table 6.6: Numerically calculated ZPE, defect formation energy, total energy, and bond length increase for the P-X defect complexes. Quoted energies are in eV

zero-point energy, are insufficient when properties dependent on the total energy are of interest. It should be noted, however, that the formation of the P-H bond in this complex serves to reduce the defect formation energy when compared to that of a lone phosphorus.

It is important to consider whether the parameters obtained for the P-X bond in molecular systems, and used in the calculations of the P-X defect complex, are valid, since the defect complex has a radically different local structure to that of the molecular bond. In order to evaluate the suitability of the parameters used in the calculations presented in Table 6.5, the PES on which the HLN moves was again sampled, both along and normal to the P-X bond, and the Schrödinger equation for this PES was solved numerically. The results of these calculations can be seen in Table 6.6. There is a remarkable increase in the zero-point energy over that found in the reference calculations, with the ZPE along the bond increasing by ~25%, and the ZPE's normal to the bond increasing by over 100%, illustrating the effect of the surrounding atoms on the motion of the HLN, an effect predicted using the PCM. The bond length increase is also reduced by approximately 40% for the muon, and approximately 50% for the proton. This is due to the fact that there is a pronounced maximum between the anti-bonding site and the tetrahedral site, both of which lie along the $[\overline{1}11]$ axis. This can be seen in the potential surface shown in Figure 6.4, which illustrates the fact

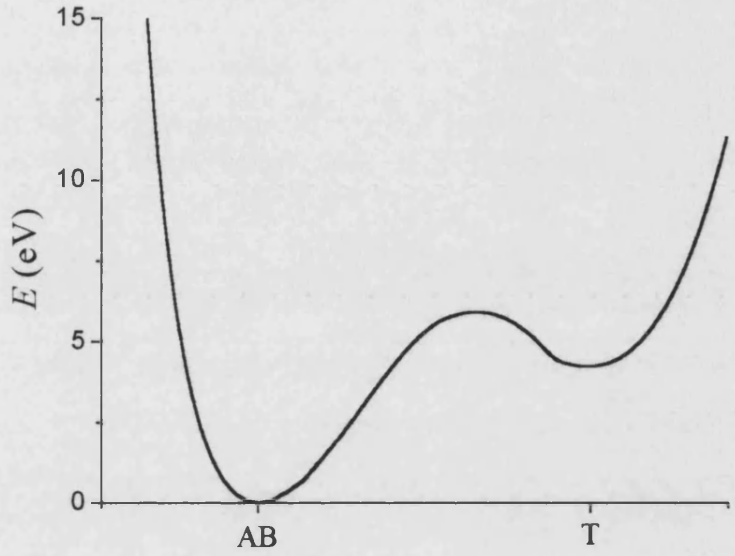

Figure 6.4: The [111] adiabatic potential energy surface upon which the HLN moves

that the antibonding site is indeed more stable than the tetrahedral site, with a barrier of 5.915 eV between the antibonding and cage centres. The barrier is some 1.686 eV above the local minimum found at the cage centre, and so it would be expected that both the muon and proton would also be trapped at the cage centre since the zero-point energies of the proton and muon would be expected to be significantly lower than this. It should be noted that the cage centre referred to in Figure 6.4, is the centre in the cage adjacent to that for the antibonding site is found, i.e. an HLN at the cage centre would have four carbons as nearest neighbours, rather than three carbons and an impurity.

Comparison of Tables 6.5 and 6.6 show that the PCM has reproduced the general features of the HLN component of the defect-complex. In particular, the muon zero-point energy is accurate to 0.04 eV (5.8%), an encouraging sign which suggests the PCM is accurately modelling the HLN-electron correlation across

Particle	f_c	ZPE (eV)	E_T (a.u.)	E_D (eV)	Δx (Å)
μ^+	0.645	0.653	-1688.46415	2.031	0.023
p	0.740	0.232	-1688.51454	0.666	0.005

Table 6.7: ZPE, defect formation energy, total energy, and bond length increase for the P-X defect complexes, parametrised for this system

considerably different systems. The proton zero-point energy is less accurate, however, being overestimated by some 0.105 eV (44.8%). In both cases, Δx is underestimated by around 50%.

Although the features of the HLN component of the defect complex have been reasonably well modelled using the parameters obtained from the reference calculations, it is worth considering how large the alteration to these parameters must be to model the HLN more accurately. Table 6.7 gives the parameters which best model the PX complex. As can be seen, the zero-point energies are much better modelled, the realtive defect formation energies remain largely unaffected, and Δx is improved to 79% of the numerical value for the muon. The bond length increase is still considerably underestimated for the proton. An explanation for this may be found if Figure 4.6 is considered again. A ridge can be seen in the effective potential. If a similar effective potential is being experienced here, and is located low enough in the potential well, the effect would be to significantly reduce the 'tail' of the proton wavefunction, whilst leaving the muon wavefunction relatively unaffected.

The defect formation energies are relatively insensitive to the reparametrisation of the P-X bond in the defect complex. This is to be expected, since the zero-point energies, and hence the HLN-electron correlation energies, are well modelled using the original parameters, and it these components of the total energy that give the defect formation energy the calculated mass dependence.

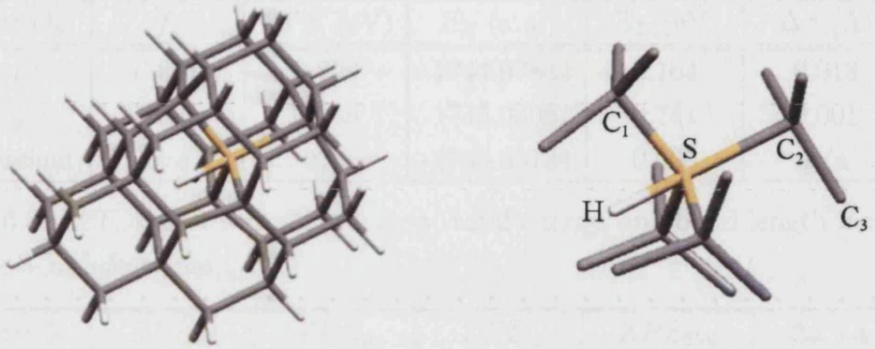

Figure 6.5: The UHF/6-31G relaxed structure of the $C_{35}H_{40}SH$ cluster

6.2.2 The SX Complex

Calculations were carried out on the SX complex in diamond in an analogous way to those of Section 6.2.1, with a sulphur atom replacing the phosphorus in the diamond cluster. The relaxed features of this cluster are again worth considering. The carbons nearest to the substitutional sulphur can be seen to be displaced from the perfect crystal structure. The S-C_1 bond length is equal to 1.767 Å, an increase of 0.222 Å (14.4%). The S-C_2 bond length is equal to 2.010 Å, an increase of 0.465 Å (30.1%). The angle C_1SC_2 is equal to 104.62°, a decrease of 4.84° (4.4%). The angle PSC_2C_3 is equal to 97.18°, a decrease of 12.28° (11.2%). Finally, the S-H bond length is equal to 1.312 Å, a decrease of approximately 3% from the standard value of around 1.35 Å calculated for the reference systems. The distortion to the crystal can be seen to be far more pronounced here than in the P-X complex. The S-C bond length along the [111] direction is severely dilated, with the majority of this dilation due to the carbon being forced away from its perfect lattice location. The carbon lies close to the plane of its nearest neighbours.

The parameters $f_{c\mu}^S = 0.607$ and $f_{cp}^S = 0.685$ obtained from the S-X bond

Particle	f_c	ZPE (eV)	E_T (a.u.)	E_D (eV)	Δx (Å)
μ^+	0.607	0.769	-1744.97832	2.164	0.013
p	0.685	0.338	-1745.03061	0.741	0.001
classical	n/a	n/a	-1745.05784	0.000	n/a

Table 6.8: ZPE, defect formation energy, total energy, and bond length increase for the S-X defect complex

Particle	ZPE_x	ZPE_y	ZPE_z	ZPE_{Tot}	Δx (Å)
μ^+	0.265	0.192	0.194	0.651	0.047
p	0.089	0.065	0.067	0.221	0.011

Table 6.9: ZPE, defect formation energy, total energy, and bond length increase for the S-X defect complex. Quoted energies are in eV

reference calculation where used in the PCM to investigate the quantum nature of the HLN in the SX complex, and the results of these calculations can be seen in Table 6.8. The large zero-point energy increases are again predicted using the PCM, and these values are quite similar to those predicted for the PX complex using the parameters obtained from the reference calculations. It may be expected therefore, that whilst the muon zero-point energy may be quite accurate, that of the proton is probably significantly over-estimated. The bond length increase for each of the cases would also be expected to be too small. The PCM calculations were therefore checked numerically and the results of these numerical calculations can be seen in Table 6.9. Again, the qualitative features of the complex have been obtained from the PCM using the S-X bond parameters, i.e. the significant increase in zero-point energy, and the corresponding decrease in Δx. The muon zero-point energy is predicted less well than in the PMu complex, with the PCM overestimating this by 0.118eV (18.1%). The proton zero-point energy is again significantly too large, being overestimated by 0.117eV (52.9%). The bond length increases are underestimated in both cases, with

Particle	f_c	ZPE (eV)	E_T (a.u.)	E_D (eV)	Δx (Å)
μ^+	0.633	0.652	-1744.98405	2.008	0.019
p	0.725	0.230	-1745.03425	0.642	0.006

Table 6.10: ZPE, defect formation energy, total energy, and bond length increase for the S-X defect complex, parametrised for this system

the proton value being the most severely inaccurate. The general features of this calculation bear a striking resemblance to those of the P-X bond however, implying that systematic corrections could be made to account for these failings in the model.

The [111] potential energy surface upon which the HLN moves in the SX complex is broadly similar to that shown in Figure 6.4. In this case the barrier between the antibonding and cage centres was found to be 4.017 eV, with a local minimum at the cage centre being 1.613 eV below this barrier, again suggesting that both the muon and proton would also be stable at the cage centre.

The correlation factor f_c was again varied to obtain better agreement with the numerical calculations of Table 6.9. These values, along with the predicted energies and bond length increases, can be seen in Table 6.10. Again, using different parameters allows the zero-point energies to be accurately predicted, although the bond length increases remain underestimated. This could be due to the reason given in Section 6.2.1 to account for the same feature of the PCM calculations on the PX complex. As seen for the PX complexes the mass dependent defect formation energies are relatively insensitive to the reparametrisation of the S-X bond.

6.3 HLN-Impurity-Vacancy Complexes in Diamond

In Section 6.2, The PX and SX defect complexes in diamond were studied, and it was found that the defect formation energies were high, and indeed positive for the SH, SMu, and PMu complexes. This was mainly due to the large lattice deformation associated with the interstitial impurity, which is large in comparison with the neighbouring carbons. In reality, the host crystal is not perfect, but will contain various other defects, of which we will consider here the vacancy. A vacancy creates a site in which an impurity replacing a nearest neighbour carbon will not induce such a large lattice distortion, leading to a lower defect formation energy. There has recently been interest in such defects, and in particular the nitrogen-hydrogen-vacancy (NHV) defect, for which the negatively charged complex is experimentally observed to have [111] symmetry [49]. Theoretical calculations [52] find the hydrogen localised via the saturation of one of the carbon dangling bonds present due to the vacancy. These calculations do not account for the experimentally observed symmetry. Rapid diffusion of the hydrogen between the *three* nearest neighbour carbons, however, would account for this, and this is in fact suggested as a possible explanation in [52]. In this section, various *neutral* HLN-impurity-vacancy complexes are studied, and the three-dimensional version of Herring's formula, derived in Section 2.4, is employed to estimate the tunnel splitting energy, and hence the tunnelling rate, of hydrogen and muonium in these complexes. It is particularly important to study the isotope effects here, since the tunnelling rate is highly sensitive to the mass of the tunnelling particle and so the [111] defect symmetry may be conceivable for the muon, but not the proton, if only quantum diffusion is considered.

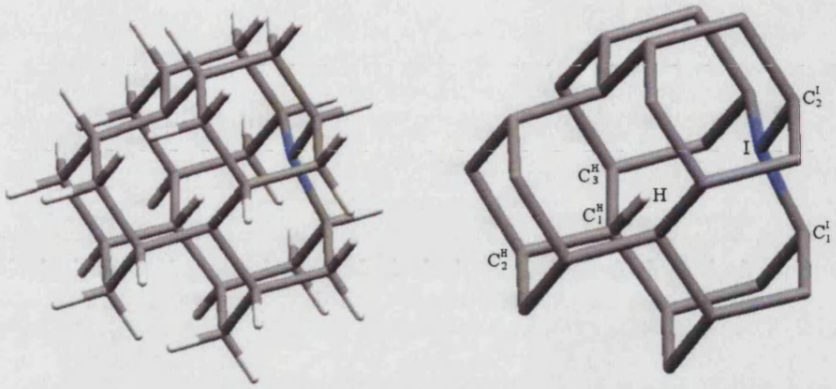

Figure 6.6: UHF/6-31G relaxed structure of the $C_{27}H_{36}NX$ cluster used for calculations upon the NXV defect complex

The impurities considered in this section are nitrogen, phosphorus, and sulphur, each of which adopt an interstitial position in the complexes discussed here. As a reference, the hydrogen-vacancy complex was also studied. The cluster used in the calculations presented here was $C_{27}H_{36}IX$, where I={C, N, P, S}, X={Mu, H}. This cluster was centred on the vacancy. The nearest and second nearest neighbours to the HLN, along with the nearest neighbours to the vacancy, were relaxed using Gaussian 98 at the UHF/6-31G level, and for each of the complexes, the lowest energy site was obtained when the HLN saturated one of the carbon dangling bonds. The relaxed structure of the $C_{27}H_{36}NH$ complex is shown in Figure 6.6, both with and without saturating hydrogens.Various structural properties of the cluster where taken in order to study the dependence of the crystal structure on the impurity species. These properties are summarised in Table 6.11. As can be seen, the local structure around the HLN remains largely unaffected by the presence of the impurity. However, the local structure of the impurity itself is altered to a more noticeable extent, with the presence of

Complex	C-H (Å)	C_1^H-C_2^H (Å)	$\angle C_2^H C_1^H C_3^H$(°)	I-C_1^I(Å)	$\angle C_1^I IC_2^I$(°)
CXV	1.053	1.519	112.7	1.497	115.6
NXV	1.040	1.511	113.0	1.480	114.2
PXV	1.031	1.517	114.9	1.718	106.5
SXV	1.051	1.516	114.1	1.725	105.9

Table 6.11: Various properties of impurity-HLN-vacancy defects in diamond

the large phosphorus or sulphur atoms inducing a dilation in the bond length, and a corresponding reduction in the angle $C_1^I IC_2^I$. For the smaller carbon and nitrogen, the opposite is observed. The PCM was used to evaluate the HLN wavefunction in these complexes, with the parameters obtained in Section 4.4.2 for the C-X bond being used. The results of Section 6.2 suggest that these parameters should be sufficient to model well the C-Mu bond in each of these complexes, although the same cannot be said for the C-H bond. Tables 6.12 and 6.13 summarise the HLN properties in these complexes. Numerical calculations

complex	f_c	ZPE_μ (eV)	Δx_μ (Å)
CMuV	0.663	0.574	0.046
NMuV	0.663	0.607	0.042
PMuV	0.663	0.625	0.040
SMuV	0.663	0.615	0.041

Table 6.12: Zero-point energies and increases in bond length for the muon in the CMuV, NMuV, PMuV, and SMuV complexes, calculated using the PCM with parameters obtained from the reference calculations

were also performed by obtaining the PES on which the HLN moves, and solving the Schrödinger equation numerically for this PES. The results of these calculation are presented in Table 6.14. The PCM succeeds in predicting an increase in the zero-point energy of the muon in all of the complexes when compared to those of the C-Mu bond in the reference systems. It also succeeds in predicting

complex	f_c	ZPE_p (eV)	Δx_p (Å)
CHV	0.758	0.239	0.004
NHV	0.758	0.261	0.003
PHV	0.758	0.260	0.003
SHV	0.758	0.261	0.003

Table 6.13: Zero-point energies and increases in bond length for the proton in the CHV, NHV, PHV, and SHV complexes, calculated using the PCM with parameters obtained from the reference calculations

complex	ZPE_x (eV)	ZPE_y (eV)	ZPE_z (eV)	$ZPE_{Tot.}$ (eV)	Δx (Å)
CMuV	0.293	0.139	0.139	0.571	0.048
NMuV	0.308	0.150	0.145	0.603	0.044
PMuV	0.315	0.138	0.138	0.591	0.043
SMuV	0.308	0.165	0.155	0.628	0.051
CHV	0.103	0.045	0.045	0.193	0.016
NHV	0.107	0.049	0.047	0.203	0.014
PHV	0.111	0.045	0.045	0.201	0.011
SHV	0.104	0.055	0.060	0.219	0.011

Table 6.14: Numerically calculated zero-point energies and increases in bond length for the CXV, NXV, PXV, and SXV complexes

an increase in the zero-point energy when a carbon is replaced by an impurity, and models the corresponding decrease of Δx well in all cases except sulphur. In particular, the results for the CMuV and NMuV are in excellent agreement with the numerical calculations Again, the PCM performs less well for the proton when the parameter obtained from the C-H bond reference systems is used. Although it again correctly predicts the increase in zero-point when a carbon is replaced by an impurity, the increase in bond length is severely underestimated. The ratios of the zero-point energies and bond length increases, as obtained from the PCM and the numerical calculations, is shown in Table 6.15. Since the intention here was to use the HLN wavefunctions obtained from the PCM to

complex	ZPE_P/ZPE_N	$\Delta x_P/\Delta x_N$
CMuV	1.01	0.96
NMuV	1.01	0.95
PMuV	1.06	0.93
SMuV	0.98	0.80
CHV	1.24	0.25
NHV	1.29	0.21
PHV	1.28	0.27
SHV	1.19	0.27

Table 6.15: Comparison of zero-point energies and bond length increases, calculated numerically and using the parametrised correlation model with parameters obtained from the reference calculations, for the CXV, NXV, PXV, and SXV complexes

calculate tunnel splitting energies, the optimal values for the correlation factor f_c were found, so that the wavefunctions obtained could be used to evaluate these energies. The optimal values for f_c, along with the associated zero-point energies and bond length increases, are presented in Table 6.16.

In the systems being considered here there are three possible positions that the HLN can adopt, due to the three dangling bonds created by the vacancy. For three identical potential wells, located at the vertices of a triangle, the tunnel-splitting energy can be approximated using the appropriate three-dimensional version of Herring's formula which, in atomic units, is given by

$$\Delta E = \frac{3}{m} \int_{-\infty}^{\infty} \int_{-\infty}^{\infty} \varphi(0,y,z) \frac{\partial \varphi(0,y,z)}{\partial x} \, dy \, dz. \tag{6.1}$$

This represents the difference in energy between the symmetric ground state and doubly degenerate first excited states of a particle in the aforementioned triple potential well when the wells are separated by a *finite* barrier. Here $\varphi(x,y,z)$ is the wavefunction of the particle in one of the wells when there are no other

potential minima, and this function, along with its first derivative, must be evaluated at $x = 0$, where this represents the top of a barrier, and hence defines a plane of symmetry for the ground state. In the PCM calculations presented in this section, $\varphi(x, y, z)$ is the calculated HLN wavefunction and, assuming the geometry used to calculate this localised state is a good approximation to the geometry of a system containing a rapidly tunnelling particle, Herring's formula can be directly applied. It should be noted here that no other atomic motion is considered in these calculations, and so the 'undressed' tunnel-splitting energies are calculated. Inclusion of the atomic motion would in this case reduce this energy. Table 6.17 gives the tunnel splitting energies, calculated using Herring's formula, for the muon and proton in each of the defect complexes considered in this section.

The tunnel splitting energy of the muon in these defect complexes varies between 3-7% of the corresponding zero-point energy, and so the tunnelling could only be considered weak. For the proton, the tunnel splitting energy is even smaller, varying between 0.3-0.7% of the zero-point energy. It should be noted, however, that Goss *et al.* [52] predict a barrier between equivalent minima of no greater than 0.4 eV, and so the zero-point energies calculated here are small enough to support the suggestion that quantum diffusion is the mechanism responsible for the observed defect symmetry. Table 6.18 gives the time taken for a proton or muon initially localised in any given well to return to this well, obtained using Equation 2.96. The results of [49] were obtained using an ESR technique which would be expected to give a time resolution of $\tilde{}10^{-10}$ s. The results presented here suggest that, for the neutral charge state at least, quantum diffusion of the proton is sufficient to give an apparent experimental [111] defect symmetry, a conclusion supported when extra consideration is given to

complex	f_c	ZPE (eV)	ZPE_P/ZPE_N	Δx (Å)	$\Delta x_P/\Delta x_N$
CMuV	0.663	0.574	1.01	0.046	0.96
NMuV	0.663	0.607	1.01	0.042	0.95
PMuV	0.675	0.595	1.01	0.043	1.00
SMuV	0.660	0.622	0.99	0.040	0.78
CHV	0.775	0.195	1.01	0.007	0.44
NHV	0.790	0.199	0.98	0.007	0.50
PHV	0.790	0.204	1.01	0.006	0.55
SHV	0.785	0.218	1.00	0.005	0.45

Table 6.16: Zero-point energies and increases in bond length for the HLN in the CXV, NXV, PXV, and SXV complexes, calculated using the PCM with parameters optimised for these systems

complex	f_c	ΔE (eV)	complex	f_c	ΔE (eV)
CMuV	0.663	0.0393	CHV	0.775	1.467×10^{-3}
NMuV	0.663	0.0188	NHV	0.790	6.776×10^{-4}
PMuV	0.675	0.0201	PHV	0.790	5.253×10^{-4}
SMuV	0.660	0.0359	SHV	0.785	7.883×10^{-4}

Table 6.17: Tunnel-splitting energies of the HLN in the CXV, NXV, PXV, and SXV complexes, calculated using the PCM with parameters obtained from the reference systems

complex	f_c	$\tau_{\Delta E}$ ($\times10^{-12}$s)	complex	f_c	$\tau_{\Delta E}$ ($\times10^{-12}$s)
CMuV	0.663	0.1052	CHV	0.775	2.8194
NMuV	0.663	0.2201	NHV	0.790	6.1009
PMuV	0.675	0.2058	PHV	0.790	7.8736
SMuV	0.660	0.1152	SHV	0.785	5.2459

Table 6.18: Tunnelling period of the HLN in the CXV, NXV, PXV, and SXV complexes, calculated using the PCM with parameters obtained from the reference systems

complex	f_c	ΔE (eV)	complex	f_c	ΔE (eV)
CMuV	0.663	0.0393	CHV	0.758	4.091×10^{-4}
NMuV	0.663	0.0188	NHV	0.758	9.311×10^{-5}
PMuV	0.663	0.0183	PHV	0.758	8.094×10^{-5}
SMuV	0.663	0.0371	SHV	0.758	2.021×10^{-4}

Table 6.19: Tunnel splitting energies of the HLN in the CXV, NXV, PXV, and SXV complexes, calculated using the PCM with parameters optimised for these systems

complex	f_c	$\tau_{\Delta E}$ ($\times10^{-12}$s)	complex	f_c	$\tau_{\Delta E}$ ($\times10^{-12}$s)
CMuV	0.663	0.1052	CHV	0.758	10.1091
NMuV	0.663	0.2201	NHV	0.758	44.4075
PMuV	0.663	0.2260	PHV	0.758	46.4628
SMuV	0.663	0.1115	SHV	0.758	20.4620

Table 6.20: Tunnelling period of the HLN in the CXV, NXV, PXV, and SXV complexes, calculated using the PCM with parameters optimised for these systems

the validity of these results.

It has been assumed that the HLN wavefunctions are accurate, and although this is true in the context of accurate reproduction of zero-point energies and bond length increases, Figures 4.9, 4.12, and 4.13 show considerable overlocalisation across the bond. The calculations of Section 3.3 reveal that the tunnel splitting energy is dependent on the overlap of the single well wavefunctions, and so it is conceivable that the overlocalisation across the bond could lead to an underestimation of the tunnel splitting energy by an order of magnitude. As an illustration of the sensitivity of these tunnel splitting energies to the HLN wavefunction, Tables 6.19 and 6.20 show the tunnel-splitting energy and tunnelling time for the muon and proton obtained using the parameters obtained from the C-X reference systems. Although the tunnel-splitting energy of the muon re-

complex	E_D^c (eV)	E_D^p (eV)	E_D^μ (eV)
CXV	0.000	0.587	1.710
NXV	0.000	0.583	1.757
PXV	0.000	0.586	1.746
SXV	0.000	0.599	1.783

Table 6.21: Defect formation energies of the CXV, NXV, PXV, and SXV complexes, where X represents the muon, proton, or a point charge

mains essentially unaffected when the sub-optimal wavefunctions are used, the tunnel-splitting energy of the proton is reduced by up to an order of magnitude, due to the overlocalisation of the wavefunction. For these reasons, the tunnel-splitting energies calculated here should be considered lower estimates of the true tunnel splitting energy, although those calculated for the muon would be expected to be good approximations to the true values.

Finally, the dependence of the relative defect formation energies of the each of the complexes on the mass of the HLN can be considered. These energies, presented in Table 6.21, were calculated in the same manner as those associated with the PX and SX defects, and for systems containg a quantum HLN the optimal correlation factors presented in Table 6.16 were used. The raising of these energies when the quantum nature of the HLN is included is smaller for these complexes, but remains significantly larger than the zero-point energy. Since the zero-point energies of the HLN in all of the complexes considered in this chapter are comparable, it can be deduced that the HLN-electron correlation is not as significant in the vacancy containing complexes as in those with no vacancy. This would be expected since, as was shown in Section 4.3, the HLN-electron correlation energy rapidly approaches zero as the separation between the two increases. In the case of the PX and SX complexes, there is a greater electron density in close proximity to the HLN than in the vacancy containing

defects, and so the corresponding HLN-correlation energy is greater. This leads to a raising of the relative defect formation energy.

Chapter 7

Conclusions and Further Work

7.1 Conclusions

General Conclusions

I have found that in all cases considered here the HLN-electron correlation had to be modelled accurately in order to obtain realistic HLN wavefunctions. For the first time, I have shown that this correlation could be accounted for by using a parametrised model potential, and this model potential gave accurate results in molecular systems if the parametrisation was assumed to be dependent only on the atomic species to which the HLN was bonded. I have applied this parametrised model in order to study features of various systems, which are only accessible via quantum mechanical methods. This was achieved at a fraction of the computational cost of path-integral Monte-Carlo (PIMC) methods. I have shown that using this parametrisation, there was a significant dependence of the total system energies on the mass of the HLN. When I applied the PCM to systems which were significantly different to those used to parametrise the model, the results were still reasonably accurate, suggesting the model potential was able to well approximate the HLN-electron correlation across different systems, although small changes to the parametrisation resulted in significantly improved

wavefunctions. This lends weight to the argument that a consideration of next nearest neighbours of the HLN (and possibly more remote components of a system) may lead to better parametrisation.

Chapter 2

For the first time I extended Herring's Formula [61] so that the tunnel splitting energy of a particle confined to a symmetric double potential well in a three-dimensional space could be considered. I then further extended this work to allow the evaluation of the tunnel splitting energy of a particle confined to a potential energy surface composed of three identical potential wells located at the vertices of an equilateral triangle, a geometry found in certain hydrogen-impurity-vacancy complexes in diamond, such as that considered in Chapter 6. In this case, I found that the splitting was not symmetric around the ground state energy of the particle localised in a single well, and so predicted an amplification of the tunnelling rate when compared to that of the two-well system.

Chapter 3

I studied some general problems concerning the evaluation of the hydrogen-like nuclear (HLN) wavefunction in the context of interacting harmonic oscillators. Firstly, I considered the nature of the variationally optimal isotropic HLN ground state wavefunction for a particle moving in an anisotropic potential, and I found that the more energetic components of the wavefunction were best approximated when using a basis which sufficiently spanned the entire configuration space.

Secondly, I confirmed the validity of Herring's formula in the evaluation of tunnel-splitting energies. I achieved this by considering a particle of muon mass tunnelling through a finite barrier, and evaluating the tunnel-splitting energy using Herring's formula, in addition to both analytical and numerical evalu-

ation. I found that for physically realistic barrier height and potential well separation, Herring's formula was a very good approximation to the numerical tunnel-splitting energy.

Finally, I considered the effects of HLN-electron correlation on the HLN wavefunction by studying a system in which two particles of differing mass interact with each other, and the external environment, harmonically. This system can be considered to be a crude approximation to a trapped hydrogen atom. For the first time, I solved the Schrödinger equation of the system exactly and within the framework of the Hartree-Fock (HF) approximation. I found that the HF approximation led to the HLN component of the wavefunction becoming highly overlocalised, with a zero-point energy some three times larger than that obtained using the exact wavefunction. I found the electron component of the wavefunction to be almost completely insensitive to this approximation. I obtained an analytical form for the HLN-electron correlation energy and, for physically realistic HLN-electron mass ratios, found this correlation energy to be proportional to $m^{-1/2}$, where m is the HLN mass.

Chapter 4

I studied small molecular systems containing a single hydrogen-like nucleus using Gaussian 98, with the HLN-electron interaction modelled within the HF approximation. I compared the HF-HLN wavefunctions to those obtained by finding the adiabatic potential energy surface upon which the HLN moves, and numerically solving the Schrödinger equation for this PES. As observed in Chapter 3, The wavefunctions obtained within the HF approximation were highly overlocalised, showing that HLN-electron correlation effects are also extremely important when the HLN is coupled to a system through the Coulomb interaction.

I developed a parametrised correlation model (PCM) which allowed the accurate evaluation of the mass-dependent HLN wavefunction in all of the systems considered in this chapter through the variation of a single parameter. I achieved this by assuming that the correlated potential experienced by the HLN could be well modelled by a linear combination of Hartree-Fock and 'Born-Oppenheimer' potentials. In this way, I parametrised the C-X, N-X, and O-X bonds, where X represents H, Mu, or D. I again found the HLN-electron correlation energy to have an $m^{-1/2}$ dependence, where m is the HLN mass.

Chapter 5

I applied the parametrised correlation model of Chapter 5 in order to study the adducts of the four DNA base molecules formed by addition of hydrogen or muonium to an unsaturated bond. I found that when the finite mass of the HLN was included (i.e. when the HLN was modelled quantum mechanically as opposed to classically) the relative stability of adducts formed by addition at a carbon site increased when compared to the stability of adducts formed by addition at nitrogen and oxygen sites respectively. I also calculated that adducts formed by addition at a nitrogen site became more stable than those formed by addition at an oxygen site. Furthermore, I found that these effects were more pronounced for an HLN of muon mass than for one of proton mass.

I found that the inclusion of effects due to the finite mass of the HLN did not result in a reordering of the most stable adducts, i.e. the most stable adducts found using a classical HLN remained the most stable adducts. For some of the higher energy adducts, however, the inclusion of these effects led to some adducts becoming more stable than those predicted to be more stable using a classical description of the HLN. In particular high energy adducts formed by addition

to carbon became more stable than adducts formed by addition to nitrogen and oxygen.

I found that the most stable adduct of cytosine, 5–X-cytosine, and the second most stable adduct of guanine, 6-X-guanine, were formed by addition at a nitrogen site, irrespective of effects due to the finite mass of the HLN. When the variation of the hyperfine coupling constant (HFCC) at the HLN as a function of bond length was considered, I discovered that there was a crossing of electronic energy levels, with the highest occupied molecular orbital (HOMO) changing from a delocalised bonding orbital to a localised, 1*s*-like, non-bonding orbital. When I considered the PCM calculated HLN wavefunctions, I found that there was a non-zero probability that the HLN would be found at a distance sufficiently far from the remainder of the system for the HOMO to be described by this non-bonding orbital, suggesting that although these adducts are energetically stable, the amplitude of the zero-point energy is large enough for these adducts to be *unstable*. The experimentally observed adduct 1,2-dihydrocytidine is formed by addition to sites the sites labelled 1 and 2 in Figure 5.2. The adduct 5-X-cytosine (shown in Figure 5.3) has, to my knowledge, not been reported..

Finally, I found that the vibrationally averaged HFCC's were significantly larger than the 'static' values (obtained by finding the HFCC at the equilibrium geometry). This fact leads to the experimentally observable residual isotope effects. For adducts formed by addition to a ring carbon, the residual isotope effect was calculated here to be $\sim$1.26, comparable to the experimental value, obtained from the isotopomers of the cyclohexadienyl radical, of 1.21.

The results of Chapter 6 show a marked change in the quantum motion of the HLN when it's local environment is altered from a molecular to a crystalline one. Similar effects might be expected for the results presented in Chapter 5 if

the DNA base molecules were surrounded by water. This would give insight into the change in behaviour of single strand DNA, currently being used in various applications (see Chapter 5), and that of DNA in the more widely considered double helix form, where the paired bases linking the helices would be essentially 'dry'.

Chapter 6

I used the PCM to study the phosphorus-hydrogen (PH), sulphur-hydrogen (SH), hydrogen vacancy (CHV), nitrogen-hydrogen-vacancy (NHV), phosphorus-hydrogen-vacancy (PHV), and sulphur-hydrogen-vacancy (SHV) complexes, along with their muonated analogues. I Parametrised the P-X and S-X bonds, and used these parameters in order the study the PX and SX complexes. The PCM predicted a large increase in the zero-point energies of both the proton and muon in these systems compared to the molecular ones, a feature verified by numerical calculations. I found, however, that the zero-point energies of the proton were overestimated using the PCM.

I used the parameters obtained in Chapter 4 for the C-X bond in order study the CXV, NXV, PXV, and SXV complexes, since in each of these the total energy of the system was minimised by the HLN saturating a carbon dangling bond. The PCM again correctly predicted an increase of the HLN zero-point energies over those found for the HLN in C-X bonds, although numerical calculations again revealed the proton zero-point energy to be overestimated.

I reconsidered the defect complexes discussed here using parameters optimised for the complexes themselves. I used results of these calculations to study the mass dependence of the defect formation and tunnel-splitting energies. In all complexes, I found that the effect of including the finite mass of the HLN

raised the defect formation energy.

I obtained the tunnel-splitting energies for both the muon and proton in the impurity-HLN-vacancy complexes. Experimentally, the negatively charged NHV defect complex is found to have a [111] symmetry. The results of the calculations presented here suggest that for the neutral NHV complex, quantum diffusion may be adequate to account for the experimentally observed symmetry. Further calculations would be required in order to determine if this is the case for the negative charge state.

7.2 Further Work

There are various approaches that could be taken to extend this work. One would be to systematically parametrise a larger group of HLN-containing bonds, in order to determine if a relationship between the parametrisation and atomic species could be identified. In this way, the parametrisation could be to some extent automated. Previously mentioned extensions of this would be to recognise HLN-next nearest neighbour interactions as significantly contributing to the parametrisation, potentially leading to a parametrisation of the HLN- containing bond in terms of a functional group. It would also be of use to study how the parametrisation is affected when different charge states of the HLN are considered. In this way consideration could be given to the effects of HLN-electron correlation when charge transfer processes occur.

It would be useful to perform some higher level calculations, using a method such as PIMC, in order to determine if the mass dependence of properties considered in this thesis can be reproduced at this higher level. This method could also be used in an attempt to develop an HLN-electron correlation functional in terms of the HLN and electron densities. A similar approach has allowed for

a positron-electron correlation functional to be constructed [106]. This would have the added advantage that the electron density could be calculated in a manner which would include the HLN-electron correlation. Recent PIMC calculations [108] suggest that the inclusion of such effects leads to a strengthening of hydrogen bonds in liquid hydrogen fluoride.

It may be possible to relax some of the restrictions placed on the PCM in Section 4.3 by considering a multipole expansion of the potential energy since this would, in principle, allow for basis functions without a well-defined maxima at their centre to be used, and hence give a much greater degree of flexibility to the basis set. Improved flexibility could also be achieved by using a contracted basis set, where the contraction scheme allowed for Gaussians functions on more than one centre to be included in the same basis function. In this way, instabilities in the overlap matrix which proved a problem during the course of this work could be reduced.

Another approach would be to consider in more detail how accurately the quantum diffusion of the HLN could be modelled within the frameworks discussed in this thesis. Attempts were made during the course of this thesis to evaluate the tunnel splitting energy explicitly, i.e. by placing HLN centres at more than one potential energy minimum, and attempting to evaluate the tunnel-splitting energy by calculating the HLN eigenvalues of the ground and first excited states. It appears that neither the HF-approximation, nor the PCM model, were sufficiently accurate to obtain tunnel-splitting energies this way, even for very simple systems, making it more important to have a more general description of the HLN-electron correlation.

The results of Chapter 5 seem to be the first to explicitly consider the relative energies of all possible DNA base molecule adducts that can be formed

by addition of hydrogen. It would therefore be useful to study these systems using a higher level of theory, in order to gain a more accurate description of the hyperfine interaction. This would emphasize the importance of including the zero-point vibrational motion when using theoretical results to interpret experimental data.

The results of Chapter 6 suggest that the PCM can still be reasonably accurate even when applied to systems considerably different to those for which it was parametrised. This makes the study of dynamical processes a possibility, for example, the muon could be used to probe the change in electronic structure, and hence the hyperfine interaction, as DNA strands are stretched. Another possibility would be to use the muon to study soliton motion, which has been considered as a mechanism for chemical energy transport in proteins [29].

The model presented in this thesis has succeeded in adequately describing many features of HLN-containing systems, but no-one - even those using computationally expensive methods - has succeeded in simulating some of the most important outstanding problems, such as the hydrogen tunnelling believed to be responsible for catalysis in some enzymes [5, 57, 124].

Bibliography

[1] Adleman, L. M. (1994) *Science* **266** 1021

[2] Addison-Jones, B. *et al.* (1997) *Hyp. Int.* **106** 143

[3] Ansaldo, E. J., Niedermayer, C., and Stronach, C. E. (1991) *Nature* **353** 121

[4] Barnabas, M. V. *et al.* (1991) *J. Phys. Chem.* **95** 10204

[5] Basran, J., Sutcliffe, M. J., and Scrutton, N. S. (1999) *Biochemistry* **38** 3218

[6] Becke, A. D. (1988) *Phys. Rev* **A38** 3098

[7] Born, M. and Oppenheimer, R. (1927) *Ann. Phys.* **84** 457

[8] Boucher, D. E. and DeLeo, G. G. (1994) *Phys. Rev. B* **50** 5247

[9] Boxwell, M. A., Claxton, T. A., and Cox, S. F. J. (1993) *J. Chem. Soc., Far. Trans.* **89** 2957

[10] Boys, S. F. (1950) *Proc. Roy. Soc. (london)* **A200** 542

[11] Briere, T. M. *et al.* (2000) *Physica B* **289-290** 128

[12] Breuer, S. J. and Briddon, P.R. (1994) *Phys. Rev. B* **49** 103326

[13] Brewer, J. H. *et al.* (1973) *Phys. Rev. Lett.* **31** 143

[14] Brown R. D. *et al.* (1970) *Theo. Chim. Acta* **21** 205

[15] Buttar, D. and Webster, B. C. (1991) *J. Chem. Soc., Far. Trans.* **87** 2901

[16] Cammarere, D. *et al.* (2001) *Hyp. Int.* **136** 759

[17] Ceperly, D. M. and Alder, B. J. (1980) *Phys. Rev. Lett.* **45** 566

[18] Chang, K. J. and Chadi, D. J. (1989) *Phys. Rev. B* **40** 11644

[19] Chow K. H. *et al.* (1991) *Phys. Rev. B* **51** 14762

[20] Chow, K. H. *et al.* (1995) *Phys. Rev. B* **52** 16939

[21] Claxton, T. A. *et al.* (1990) *Hyp. Int.* **65** 913

[22] Claxton, T. A. and Cox, S. F. J. (1993) **207** 31

[23] Cox, S. F. J. and Symons, M. C. R. (1986) *Chem. Phys. Lett.* **126** 516

[24] Cox, S. F. J. (1987) *J. Phys.C: Solid Sate Phys.* **20** 3187

[25] Cox, S. F. J. *(2003) to be published*

[26] Daudel, R *et al.* (1983) *Quantum Chemistry* (Chichester: John Wiley & Sons)

[27] Davis, E. A. and Cox, S. F. J. (1996) *Protons and Muons in Materials Science* (London: Taylor & Francis)

[28] Davis, P. J. and Rabinowitz P. (1984) *Methods of Numerical Integration* (Orlando, FL: Academic Press)

[29] Davydov, A. S. (1973) *J. Theo. Bio.* **38** 559

[30] Dischler, B. *et al.* (1993) *Physica B* **185** 217

[31] Dizdaroglu, M. (1993) in *DNA and Free Radicals*, Eds. Halliwell, B. and Auroma, O. I. (Chichester: Ellis Horwood)

[32] Donzelli, O. *et al.* (1994) *Solid Sate Comm.* **90** 663

[33] Donzelli, O. *et al.* (1996) *Hyp. Int.* **97** 19

[34] Estle, T. L. *et al.* (1997) *Phys. Rev. Lett.* **58** 1547

[35] Estreicher, S. K. *et al.* (1985) *Phys. Rev. Lett.* **55** 1976

[36] Estreicher S. K. *et al.* (1986) *Phys. Rev. B* **34** 6071

[37] Estreicher, S. K. (1987) *Phys. Rev. B* **36** 9122

[38] Estreicher, S. K. *et al.* (1992) *Chem. Phys. Lett.* **196** 311

[39] Estreicher, S. K. *et al.* (1995) *Mat. Sci. Eng.* **R14** 319

[40] Estreicher, S. K (2000) *Phys. Stat. Sol.* **B217** 513

[41] Farrer, R. G. (1969) *Solid State Comm.* **7** 685

[42] Feynman, R. P. and Hibbs, A. R. (1965) *Quantum Mechanics and Path Integrals* (New York: McGraw Hill)

[43] Fischer, H. (1962) *Kolloid-Z* **180** 64

[44] Friedman, J. I. and Telegdi, V. L. (1957) *Phys. Rev.* **105** 1681

[45] Frisch, M. J., Trucks, G. W., Schlegel, H. B., Scuseria, G. E., Robb, M. A., Cheeseman, J. R., Zakrzewski, V. G., Montgomery Jr., J. A., Stratmann, R. E., Burant, J. C., Dapprich, S., Millam, J. M., Daniels, A. D.,

Kudin, K. N., Strain, M. C., Farkas, O., Tomasi, J., Barone, V., Cossi, M., Cammi, R., Mennucci, B., Pomelli, C., Adamo, C., Clifford, S., Ochterski, J., Petersson, G. A., Ayala, P. Y., Cui, Q., Morokuma, K., Malick, D. K., Rabuck, A. D., Raghavachari, K., Foresman, J. B., Cioslowski, J., Ortiz, J. V., Baboul, A. G., Stefanov, B. B., Liu, G., Liashenko, A., Piskorz, P., Komaromi, I., Gomperts, R., Martin, R. L., Fox, D. J., Keith, T., Al-Laham, M. A., Peng, C. Y., Nanayakkara, A., Gonzalez C., Challacombe, M., Gill, P. M. W., Johnson, B., Chen, W., Wong, M.W., Andres, J. L., Gonzalez, C., Head-Gordon, M., Replogle, E. S., and Pople, J. A. *Gaussian 98, Revision A.7* Gaussian, Inc., Pittsburgh PA, 1998

[46] Garwin, R.L *et al.* (1957) *Phys. Rev.* **105** 1415

[47] Gautschi, W. (1968) *Math. Comput.* **22** 251

[48] Gillan, M. (1988) *Philos. Mag. A* **58** 257

[49] Glover, C. *et al.* (2003) *Phys. Rev. Lett.* **90** 185507

[50] Goss, J. P. *et al.* (2002) *Phys. Rev. B* **65** 115207

[51] Goss, J. P. (2003) *J. Phys.: Cond. Matt.* **15** R551

[52] Goss, J. P. *et al.* (2003) *J. Phys.: Cond Matt.* **15** S2903

[53] Halgren, T. A. and Lipscomb, W. N. (1973) *J. Chem. Phys.* **58** 1569

[54] Halgren *et al.* (1978) *J. Am. Chem. Soc.* **100** 6595

[55] Hall, G. G. (1951) *Proc. Roy. Soc. (London) A* **205** 541

[56] Halliwell, B. and Gutteridge, J. M. C. (1999) *Free Radicals in Biology and Medicine* (Oxford: OUP)

[57] Harris, R. J. *et al.* (2000) *Biochemistry* **39** 1189

[58] Hartree, D. R. (1928) *Proc. Cambridge Phil. Soc.* **24** 89, 111, 426

[59] Hasegawa, M. et al. (1999) *Jpn. J. Appl. Phys.* **38** L1519

[60] Herrero, C. P. (1996) *Phys. Rev. B* **55** 9235

[61] Herring, C. and Flicker, M. (1964) *Phys. Rev. A* **134** 362

[62] Herring, C. *et al.* (2001) *Phys. Rev. B* **64** 125209

[63] Hoffman, L. *et al.* (2000) *Phys. Rev. B* **61** 16659

[64] Hohenberg, P. and Kohn, W. (1964) *Phys. Rev. B* **136** 864

[65] Hückel, E. (1931) *Z. Phys.* **70** 204

[66] Ienaga, N. and Tsuneyuki, S. (1997) *Hyp. Int.* **105** 297

[67] Inuzuka, T. (1990) *Diamond Hakumaku (Diamond Thin Films)* (Tokyo: Kyouritsu Shuppan)

[68] Jeong, J. *et al.* (2000) *Physica B* **289** 132

[69] Jeong, J. *et al.* (2001) *Hyp. Int.* **136** 763

[70] Johnson, N. M. *et al.* (1986) *Phys. Rev. Lett.* **56** 769

[71] Kajihara, S. A. *et al.* (1991) *Phys. Rev. Lett.* **66** 2010

[72] Kanai, C. *et al.* (2002) *Phys. Rev. B* **65** 153312

[73] Kaxiras, E. and Joannopoulos, J. D. (1988) *Phys. Rev. B* **37** 8842

[74] Kohn, W. and Sham, L. J. (1965) *Phys. Rev. A* **140** 1133

[75] Korpás, L. *et al.* (1992) *Phys. Rev. B* **46** 19

[76] Landau, L. D. and Lifshitz, E. M. (1977) Quantum Mechanics (Non-Relativistic Theory), 3rd Ed. (Oxford: Pergamon Press)

[77] Lee, T. D. and Yang, C. N. (1956) *Phys. Rev.* **104** 254

[78] Lee, C., Yang, W., and Parr, R. G. (1988) *Phys. Rev.* **B37** 785

[79] Lindholm, E. and Lundqvist, S. (1985) *Physica Scripta* **32** 220

[80] Luchsinger, R. H. *et al.* (1998) *Phys. Rev. B* **57** 4413

[81] Mainwood, A. and Stoneham, A. M. (1983) *J. Phys. C: Solid State Phys.* **17** 2513

[82] Macrae, R. M. (2000) *Mag. Res. Chem.* **38** S33

[83] Macrae, R. M. and Carmichael, I. (2003) *Physica B* **326** 81

[84] Marynick, D. S. and Lipscomb, W. N. (1982) *Proc. Nat. Acad. Sci.* (USA) **79** 1341

[85] Mehandru, S. P. *et al.* (1992) *J. Mat. Res.* **7** 689

[86] Mehandru, S. P. and Anderson, A. B. (1994) *J. Mat. Res.* **9** 383

[87] Merzbacher, E. (1998) *Quantum Mechanics, 3rd Ed.* (Chichester: John Wiley & Sons)

[88] Miyake, T. *et al.* (1998) *Phys. Rev. Lett.* **81** 1873

[89] Møller, Chr. and Plesset, M. S. (1934) *Phys. Rev.* **46** 618

[90] Morton, J. R., Negri, F., and Preston, K. F. (1994) *Phys. Rev. B* **49** 12446

[91] Moshinsky, M. (1968) *Am. J. Phys.* **36** 52

[92] Moshinsky, M. and Kittel, C. (1968) *Proc. N. A. S.* **60** 110

[93] Nishimatsu, T. *et al.* (2001) *Jpn. J. Appl. Phys.* **41** 1952

[94] Noya, J. C., Herrero, C.P., and Ramírez, R. (1997) *Phys. Rev. Lett.* **79** 111

[95] Oganesyan, V. S. *et al.* (2003) *Physica B* **326** 25

[96] Parr, R. G. amd Yang W. (1989) *Density-Functional Theory of Atoms and Molecules* (New York: Oxford University Press)

[97] Percival, P. W. and Wlodek S. (1992) *Chem. Phys. Lett.* **196** 317

[98] Percival, P. W. *et al.* (1999) *Can J. Chem.* **77** 326

[99] Perdew, J. P. (1986) *Phys. Rev. B* **33** 8822

[100] Perdew, J. P. and Wang, Y. (1992) *Phys. Rev. B* **45** 13244

[101] Pople, J. A.., Santry, D. P., and Segal G. A. (1965) *J. Chem. Phys.* **43** S129

[102] Pople, J. A., Beveridge D. L., and Dobosh, P. A. (1967) *J. Chem. Phys.* **47** 2026

[103] Pople, J. A. and Beveridge, D. L. (1970) *Approximate Molecular Orbital Theory* (New York: McGraw-Hill)

[104] Porter, A. R. *et al.* (1999) *Phys. Rev. B* **60** 13534

[105] Press, W. H. *et al.* (2002) *Numerical Recipes in Fortran 90* (Cambridge: Cambridge University Press)

[106] Puska, M. J., Seitsonen, A. P., and Nieminen, R. M. (1995) *Phys. Rev. B* **52** 10947

[107] Ramírez, R. and Hererro, C. P. (1994) *Phys. Rev. Lett.* **73** 126

[108] Raugei, S. and Klein, M. L. (2003) *J. Am. Chem. Soc.* **125** 8992

[109] Roduner, E. *et al.* (1978) *Chem. Phys. Lett.* **57** 37

[110] Roduner, E. *et al.* (1982) *Chem. Phys.* **67** 275

[111] Roduner, E. and Reid, I. D. (1989) *Israel J. Chem.* **29** 3

[112] Roduner E. (1993) *Chem. Soc. Rev.* 337

[113] Roothaan, C. C. J. (1951) *Rev. Mod. Phys.* **23** 69

[114] Saada, D., Adler, J., and Kalish R. (2000) *Phys. Rev. B* **61** 10712

[115] Saada, D. *et al.* (1999) *Appl. Phys. Lett.* **77** 878

[116] Saebø, S. Radom, L, and Schaefer, H. F. (1983) *J. Chem. Phys.* **78** 845

[117] Sagar, S. P. and Smith, V. H. (1992) *Int. J. Quantum Chem.* **42** 827

[118] Sahoo N. *et al.* (1983) *Phys. Rev. Lett.* **50** 913

[119] Schenk, A. (1985) *Muon Spin Rotation Spectroscopy* (Bristol: Adam Hilger)

[120] Sellschop, J. P. F. *et al.* (1977) *Ind. Diamond Rev. Sup.* 2-4

[121] Slater, J. C. (1930) *Phys. Rev.* **35** 509

[122] Springborg, M. (2000) *Methods of Electronic-Structure Calculation* (Chichester: John Wiley & Sons)

[123] Sternschulte, H. *et al.* (1999) *Phys. Rev. B* **59** 12924

[124] Sutcliffe, M. J., and Sutton, N. S. (2000) *Phil. Trans. R. Soc. Lond. A* **358** 367

[125] Sžego, G. (1975) *Orthogonal Polynomials* (American Mathematical Society Colloquium Publication 23)

[126] Tuttle, B. and Van de Valle, C. G. (1999) *Phys. Rev. B* **59** 12884

[127] Van de Valle, C. G. et al. (1989) *Phys. Rev. B* **39** 10791

[128] Valladares, R. M. *et al.* (1995) *Chem. Phys. Lett.* **242** 1

[129] Valladares, R. M. *et al.* (1998) *J Phys: Cond. Matt.* **10** 10701

[130] Varshni, Y. P. (1957) *Rev. Mod. Phys.* **29** 664

[131] von Sonntag, C. (1987) *The Chemical Basis of Radiation Biology* (London: Taylor & Francis)

[132] Vosko, S. J., Wilk, L., and Nusair, M. (1980) *Can. J. Phys.* **58** 1200

[133] Wang, L. G. and Zunger, A. (2002) *Phys. Rev. B* **66** 161202

[134] Watson, J. and Crick, F. (1953) *Nature* **171** 153

[135] Webster, B. (1997) *J. Chem. Soc., Far. Trans.* **93** 205

[136] Xu, H. (1992) *J Phys.: Cond. Matt.* **4** 795

[137] Young, D. C. (2001) *Computational Chemistry* (Chichester: John Wiley & Sons)

[138] Yu, D. et al (1990) *Chem. Phys.* **142** 229

[139] Yurke, B. *et al.* (2000) *Nature* **406** 605